GRANT
IN-26-CR
185212
P-169

A Progress Report
June 1, 1988 - December 31, 1988
Grant No. NAG-1-745-2

ENVIRONMENT ASSISTED DEGRADATION MECHANISMS IN ADVANCED LIGHT METALS

Submitted to:

National Aeronautics and Space Administration
Langley Research Center
Hampton, Virginia 23665

Attention: Mr. J. F. Royall, Jr.
Grants Officer, MS 126

For Review by: Mr. D. L. Dicus
Contract Monitor
Metallic Materials Branch, MS 188A

Submitted by:

R. P. Gangloff
Associate Professor

G. E. Stoner
Professor

R. E. Swanson
Assistant Professor, Department of Materials Engineering
Virginia Polytechnic Institute and State University
Blacksburg, VA 24061

Report No. UVA/528266/MS89/103
January 1989

SCHOOL OF ENGINEERING AND APPLIED SCIENCE

DEPARTMENT OF MATERIALS SCIENCE
UNIVERSITY OF VIRGINIA
CHARLOTTESVILLE, VIRGINIA 22901

UNIVERSITY OF VIRGINIA
School of Engineering and Applied Science

The University of Virginia's School of Engineering and Applied Science has an undergraduate enrollment of approximately 1,500 students with a graduate enrollment of approximately 600. There are 160 faculty members, a majority of whom conduct research in addition to teaching.

Research is a vital part of the educational program and interests parallel academic specialties. These range from the classical engineering disciplines of Chemical, Civil, Electrical, and Mechanical and Aerospace to newer, more specialized fields of Applied Mechanics, Biomedical Engineering, Systems Engineering, Materials Science, Nuclear Engineering and Engineering Physics, Applied Mathematics and Computer Science. Within these disciplines there are well equipped laboratories for conducting highly specialized research. All departments offer the doctorate; Biomedical and Materials Science grant only graduate degrees. In addition, courses in the humanities are offered within the School.

The University of Virginia (which includes approximately 2,000 faculty and a total of full-time student enrollment of about 17,000), also offers professional degrees under the schools of Architecture, Law, Medicine, Nursing, Commerce, Business Administration, and Education. In addition, the College of Arts and Sciences houses departments of Mathematics, Physics, Chemistry and others relevant to the engineering research program. The School of Engineering and Applied Science is an integral part of this University community which provides opportunities for interdisciplinary work in pursuit of the basic goals of education, research, and public service.

A Progress Report
June 1, 1988 - December 31, 1988
Grant No. NAG-1-745-2

Submitted to:

National Aeronautics and Space Administration
Langley Research Center
Hampton, Virginia 23665

Attention: Mr. J. F. Royall, Jr.
Grants Officer, MS 126

For Review by: Mr. D. L. Dicus
Contract Monitor
Metallic Materials Branch, MS 188A

Submitted by:

R. P. Gangloff
Associate Professor

G. E. Stoner
Professor

R. E. Swanson
Assistant Professor
Department of Materials Engineering
Virginia Polytechnic and State University
Blacksburg, VA 24061

Department of Materials Science
SCHOOL OF ENGINEERING AND APPLIED SCIENCE
UNIVERSITY OF VIRGINIA
CHARLOTTESVILLE, VIRGINIA

Report No. UVA/528266/MS89/103
January 1989

Copy No.___

ENVIRONMENT ASSISTED DEGRADATION MECHANISMS IN ADVANCED LIGHT METALS

INTRODUCTION

A multifaceted research program on the performance of advanced light metallic alloys in aggressive aerospace environments, and associated environmental failure mechanisms, was initiated in April of 1987 under NASA-LaRC Grant NAG-1-745 [1]. Progress for the periods April 1987 to December, 1987; and January, 1988 to May, 1988 was previously reported [2,3]. A grant review meeting was held at the NASA Langley Research Center on July 15, 1988; results are collated elsewhere [4]. This report summarizes the research which has been conducted from June 1, 1988 to December 31, 1988.

The current participants in this NASA-LaRC sponsored work include two faculty and four PhD level graduate students in the Department of Materials Science at the University of Virginia, a NASA/LaRC based employee enrolled in the PhD program at UVa, and one faculty and an MS graduate student in the Department of Materials Engineering at the Virginia Polytechnic Institute and State University. The NASA grant monitor for this program is D.L. Dicus of the Metallic Materials Branch at the Langley Research Center.

This program has recently been expanded to include two additional faculty and two graduate students in Materials Science at UVa [5,6]. This new work on the NASA-UVa Light Aerospace Alloy and Structures Technology Program will be reported in June of 1989. Research on stress corrosion cracking of Al-Li alloys by Professor Stoner and Mr. James P. Moran will be added to the expanded Technology Program; results are reported here.

Problem

Problems of long-term environmental degradation and failure could impede reliable applications of advanced light metallic alloys and composites in aerospace structures. Materials of particular interest include wrought Al-Li-X alloys, powder metallurgy Al-Fe ternary and quaternary alloys, and titanium aluminides. Environments include aqueous electrolytes, cryogenic and elevated temperatures, and gaseous hydrogen. The challenge at hand is to examine alloys; which have been developed based on short term, benign environment strength and ductility; in terms of resistance to brittle fracture, localized corrosion, hydrogen embrittlement, elevated

temperature cracking, stress corrosion cracking and corrosion fatigue during prolonged environmental exposures.

Several deficiencies are generically relevant to the performance of advanced light metallics.

+ Predictions of long term durability and reliability, based on short term laboratory data, are hindered by a lack of experimental observations, fundamental understanding, and predictive models of time dependencies.

+ Laboratory measurements have not separated and characterized the localized processes which are relevant to complex failure modes. Data are not scalable to predict performance.

+ Hydrogen contributions to localized corrosion, deformation and brittle fracture have not been studied systematically.

+ Fatigue-environment interactions have not been studied, particularly with regard to transgranular crack propagation relevant to thin sheet.

+ The effects of defects common to advanced PM alloys and service have not been characterized.

+ State of the art fracture mechanics methods have not been applied to the fatigue and fracture modes which are relevant to many of the thin sheet, joint and anisotropic material applications relevant to space components.

Program Objectives

The general goal of each element of the research program is to characterize alloy behavior quantitatively and to develop predictive mechanisms for environmental failure modes. Successes in this regard will provide the basis for metallurgical optimization of alloy performance, for chemical control of aggressive environments and for engineering life prediction with damage tolerance and long term reliability.

Current Projects and Personnel

1. DAMAGE LOCALIZATION MECHANISMS IN AQUEOUS CHLORIDE CORROSION FATIGUE OF ALUMINUM-LITHIUM ALLOYS
   R.P. Gangloff and Robert S. Piascik, PhD candidate

2. MEASUREMENTS AND MECHANISMS OF LOCALIZED AQUEOUS CORROSION IN ALUMINUM-LITHIUM ALLOYS
   G.E. Stoner and Rudolph G. Buchheit, Jr., PhD candidate

3. AN INVESTIGATION OF THE LOCALIZED CORROSION AND STRESS CORROSION CRACKING BEHAVIOR OF ALLOY 2090
   G.E. Stoner and James P. Moran, PhD candidate

4. DEFORMATION AND FRACTURE OF ALUMINUM-LITHIUM ALLOYS: THE EFFECT OF DISSOLVED HYDROGEN
   R.E. Swanson and F. Rivet, MS candidate

5. DEFORMATION AND FRACTURE OF ALUMINUM LITHIUM ALLOYS: THE EFFECT OF CRYOGENIC TEMPERATURES
   Richard P. Gangloff and John A. Wagner, PhD candidate

6. ELEVATED TEMPERATURE CRACK GROWTH IN ADVANCED POWDER METALLURGY ALUMINUM ALLOYS
   Richard P. Gangloff and William C. Porr, Jr., PhD candidate

Research Status

Research progress for the period from April 1, 1987 to May 31, 1987 was reported previously [2-4]. Work conducted during the past six months is summarized below.

Appendix I contains publications which were issued under grant sponsorship. Appendix II summarizes grant travel and conference participation. Appendix III summarizes scheduled presentations with abstracts.

References

1. R.P. Gangloff, G.E. Stoner and M.R. Louthan, Jr., "Environment Assisted Degradation Mechanisms in Al-Li Alloys", University of Virginia, Proposal No. MS-NASA/LaRC-3545-87, October, 1986.

2. R.P. Gangloff, G.E. Stoner and R.E. Swanson, "Environment Assisted Degradation Mechanisms in Al-Li Alloys", University of Virginia, Report No. UVA/528266/MS88/101, January, 1988.

3. R.P. Gangloff, G.E. Stoner and R.E. Swanson, "Environment Assisted Degradation Mechanisms in Advanced Light Metals", University of Virginia, Report No. UVA/528266/MS88/102, June, 1988.

4. R.P. Gangloff, G.E. Stoner and R.E. Swanson, "Environment Assisted Degradation Mechanisms in Advanced Light Metals", University of Virginia, July, 1988.

5. T.H. Courtney, R.P. Gangloff, G.E. Stoner and H.G.F. Wilsdorf, "The NASA-UVA Light Alloy Technology Program", University of Virginia, Proposal No. MS NASA/LaRC-3937-88, March, 1988.

6. R.P. Gangloff, "NASA-UVa Light Aerospace Alloys and Structures Technology Program", University of Virginia, Proposal No. MS NASA/LaRC, December, 1988.

SUMMARY OF RESEARCH (June 1, 1988 to December 31, 1988) AND PLANS

Program 1 DAMAGE LOCALIZATION MECHANISMS IN AQUEOUS CHLORIDE CORROSION FATIGUE OF ALUMINUM-LITHIUM ALLOYS

Robert S. Piascik and R.P. Gangloff

Objective.

The objective of this PhD study is to characterize and understand intrinsic fatigue crack propagation in the class of new Al-Li-X alloys, with emphasis on the damage mechanisms for transgranular environmentally assisted cracking.

Approach.

Experimental design and analysis were presented in a previous progress report [1]. Work on corrosion fatigue in aluminum-lithium-copper alloy 2090 is divided into five areas; specifically: 1) intrinsic fatigue crack propagation kinetics, 2) gaseous environmental effects, 3) aqueous electrolyte environmental effects, 4) fractographic analysis and 5) mechanistic interpretation.

Results.

Fatigue crack growth experiments and fractographic analysis performed during the reporting period have revealed; 1) the damaging effects of very low levels of water vapor, 2) that oxide surface films do not influence mechanical crack tip damage, 3) that alloy 2090 fatigue crack growth proceeds by slip band cracking, subboundary cracking and cleavage, with the proportions depending on environment, and 4) that Mode I loading does not obviously enhance near threshold fatigue crack rates.

Detailed analyses of gaseous and aqueous environmental effects are separately presented in two appendixed papers [2,3].

Intrinsic Fatigue Crack Propagation Kinetics. The results of experiments performed to determine the importance of increased da/dN and decreased threshold stress intensity range (ΔK_{th}) for Mode I loading are inconclusive [4]. Mode I loading, "fixed grip", single edge notched (SEN) and center crack panel (CCP) experiments were performed for alloy 7075

during the reporting period. A comparison of results, shown in Fig. 1, reveals a significant difference between the fixed grip SEN and CCP results.

Similar to alloy 2090, alloy 7075 fixed grip experimental results (Fig. 1) exhibit increased da/dN and decreased ΔK_{th} compared to compact tension (CT) specimen data [4]. Significantly, the CCP specimen results shown in Fig. 1 exhibit a higher ΔK_{th} and lower da/dN compared to the fixed grip results; CCP data compare closely to the CT specimen results. These results suggest that increased da/dN and reduced ΔK_{th} observed under fixed grip Mode I loading with the SEN geometry are not real.

The anomalous fixed grip results may be due to slight displacements in the actuator load train which enable a bending component and elevated stress intensity. The fixed grip K solution assumes that the SEN specimen does not rotate; the stress intensity at constant applied load is accordingly reduced compared to a bend dominated geometry.

While not a high priority aspect of our environmental fracture work, we will attempt to gain additional insight on the issue of specimen geometry effects during the next year.

Aqueous Electrolyte Environmental Effects. No aqueous environment experiments have been conducted during the reporting period. Fractographic analyses are currently being performed on aqueous environment specimens.

Gaseous Environmental Effects. Critical experiments were performed to further investigate the environmental effects of helium, oxygen and water vapor described in the previous progress report [4]. Of particular interest is the effect of trace impurities, water vapor and hydrocarbons, during fatigue experimentation in the presumably inert helium environment and verification of the crack growth rates observed in oxygen.

Experimental results show that trace amounts (ppm levels) of water vapor exacerbate environmental cracking, resulting in the unexpectedly high crack growth rates previously reported for liquid nitrogen cold trapped (Method A) helium [4]. An improved helium purification procedure (Method B) was developed during this reporting period, and employed for the additional experiments. Specifically, helium was purified by passage through molecular sieve at 23°C to remove H_2O, followed by a reactive, hot titanium alloy chip getter to further reduce O_2 and H_2 contaminants. Shown in Fig. 2 is a comparison of the fatigue crack growth characteristics of Alloy 2090 in helium (Method B) and 2 kPa water vapor. At high ΔK, similar fatigue crack growth rates are observed in 2 kPa water vapor and high purity helium. For near threshold, Alloy 2090

exhibits a factor of ten increase in da/dN for 2 kPa H_2O compared to pure helium.

A series of near threshold constant ΔK (2.2 MPa$\cdot m^{1/2}$, R=0.88) experiments confirm that small (ppm) levels of H_2O in otherwise pure helium accelerate fatigue crack growth in alloy 2090. Data points 1 through 5, in Fig. 2, represent the sequential measurement of fatigue crack growth rate for decreased purity levels of helium. Point 1 was obtained immediately after backfilling with helium (Method B), followed by measurements 2 through 5. The crack growth rate obtained for a 7 mPa H_2O/helium environment (data point 5) increased approximately 10-fold compared to dry helium, point 1 in Fig. 2, and is similar to the value obtained for the 2 kPa water vapor experiment.

Additional experiments performed at low ΔK (2.4 MPa$\cdot m^{1/2}$), establish the damaging effect of water vapor at very low pressures. Fig. 3 reveals that at very low water vapor pressure, below 0.2 Pa at 5 Hz, fatigue crack growth is strongly dependent on H_2O pressure. A factor of ten reduction in da/dN is observed for water vapor pressures lower than 0.2 Pa, the saturation pressure. Molecular transport to the crack tip is reduced with decreasing pressure or increasing frequency below the saturation level, resulting in reduced hydrogen production at the crack tip and lower crack growth rates. These results are consistent with the transport controlled fatigue crack growth model derived for 2000 and 7000 series aluminum alloys [5]. We do, however, plan to examine the possible contribution of crack tip deformation and production of localized active surface area; unique to near threshold corrosion fatigue.

A comparison of da/dN in oxygen and purified helium (Method B) shown in Fig. 4 reveals that oxygen has little effect on the intrinsic fatigue crack growth rate in alloy 2090. At moderate ΔK and low R, a factor of three decrease in da/dN is observed in alloy 2090 for oxygen compared to helium. These data can be interpreted based on oxide induced closure during low R testing. At low ΔK and high R, little difference is observed between oxygen, helium and vacuum suggesting that oxide surface films do not alter crack tip damage by postulated slip irreversibility or homogenizing crack tip deformation mechanisms. This observation provides important input to our analysis of crack tip damage mechanisms. Auger spectroscopy experiments are planned to confirm that corrosion fatigue, in oxygen at high mean stress, produced a substantial surface oxide film.

Fractographic Analysis. Fractographic analysis has revealed three modes of fatigue cracking in peak aged alloy 2090:

1. slip band cracking,
2. subboundary cracking,
3. cleavage cracking.

The three regimes of cracking are described in Fig. 5.

Slip band cracking (SBC) is the predominant fatigue mode for non-hydrogen producing environments (oxygen, helium and vacuum) over a broad range of stress intensities. For hydrogenous environments (water vapor, moist air and aqueous NaCl), SBC is observed only for moderate to high cyclic stress intensity levels, where mechanical effects are dominant. The SBC morphology exhibits severe crack deflections parallel to the direction of growth, Fig. 5. The planar facets extend through a number of large unrecrystallized grains along (111) planes. An etched pit technique is used to confirm the fracture surface crystallographic plane. For the fcc lattice, triangularly shaped pits identify (111) planes, while square and rectangular pits identify (100) and (110) planes, respectively.

Subboundary cracking is observed for hydrogenous environments at moderate to high ΔK. Components of subboundary and slip band cracking are observed for moist air, aqueous NaCl and water vapor. Preliminary results suggest that the proportion of subboundary cracking varies with environment. The fracture surface exposed to water vapor exhibited the greatest proportion of subboundary cracking, approximately 80%. In aqueous NaCl (anodic), 50% to 75% subboundary cracking is observed and for moist air the fracture surface contains equal proportions of subboundary and slip band cracking.

The third fracture mode, cleavage, is observed within the environmentally sensitive low ΔK regime identified in Fig. 5. Fractographic analysis of moist air, water vapor, aqueous NaCl specimens revealed a transition from subboundary cracking to a flat crystallographic fracture at moderate ΔK. The regions of crystallographic fracture have been identified as (100) or (110) cleavage planes by the etch pit technique. At the time of reporting, the SEM analysis of etch pits has not been able to resolve the specific cleavage plane.

The constant K_{max} FCG results shown in Fig. 5 suggest that the subboundary/cleavage transition is ΔK dependent; occurring at a cyclic stress intensity range corresponding to a cyclically reversed plastic zone size of 5 to 10 um. This transitional plastic zone size is the approximate size of subgrains. When the reversed plastic zone is smaller than sub-grains (low ΔK), environmentally induced cleavage is preferred. As the cyclic stress intensity is increased to moderate levels, the reversed plastic zone approaches the size

of sub-grains and subboundary cracking is preferred.

Conclusions.

1. Near threshold, intrinsic fatigue crack growth rates are not clearly enhanced by Mode I loading.

2. Accelerated fatigue crack growth rates are produced by very low water vapor pressures (approximately 0.2 Pa H_2O at 5 Hz). Alloys 2090 and 7075 in water vapor exhibit crack growth kinetics which are consistent with mass transport control by impeded Knudsen flow along the crack.

3. No difference in the intrinsic fatigue crack growth rates for oxygen compared to purified helium and vacuum indicates that surface films do not influence mechanical crack tip damage.

4. Fatigue crack growth in alloy 2090 proceeds by a slip band cracking mechanism in inert environments. Slip band cracking is also observed in aggressive environments, at high K, when mechanical crack tip damage effects are dominant. In the presences of hydrogen, cracking proceeds by subboundary cracking at moderate to high ΔK and by cleavage at low levels of ΔK.

Future Work.

Research during the next reporting period will:

1. Further develop correlations between environmental crack growth rates and high resolution fractographic observations.

2. Characterize the surface film formed during fatigue crack growth in oxygen.

3. Repeat near threshold fatigue crack growth experiments for alloy 7075 in helium (Method B) and oxygen.

4. Finalize corrosion fatigue crack growth experiments in aqueous chloride electrolyte.

5. Write and defend the PhD dissertation.

It is anticipated that Mr. Piascik will achieve the PhD degree by May of 1989. A proposal has been written to extend research on corrosion fatigue to include the following [6]:

- oo quantitatively model mechanisms of mechanical-chemical damage, with emphasis on hydrogen and surface film effects on crack propagation.

- oo examine crack closure-corrosion fatigue interactions.

- oo characterize corrosion fatigue in additional microstructures, particularly to determine the effects of recrystallization and precipitation.

- oo examine new materials; including metal matrix composites, corresponding monolithic matrices, and new Al-Li alloys developed for NASA missions.

- oo examine additional environmental conditions, including varying hydrogen activity and temperature relevant to cryogenic and hydrogen storage applications.

A new PhD candidate is being recruited and a Research Associate has been hired to conduct this work.

References.

1. R.P. Gangloff, G.E. Stoner and R.E. Swanson, "Environment Assisted Degradation Mechanisms in Al-Li Alloys", University of Virginia, Report No. UVA/526266/MS88/101, January (1988).

2. R.S. Piascik and R.P. Gangloff, "Intrinsic Fatigue Crack Propagation in Aluminum-Lithium Alloys: The Effect Of Gaseous Environments", Proceedings of ICF-7, K. Salema, ed., Pergammon Press, London, in press (1989).

3. R.S. Piascik and R.P. Gangloff, "Aqueous Environment Effects on Intrinsic Corrosion Fatigue Crack Propagation in an Al-Li-Cu Alloy", Environmental Cracking of Metals, R.P. Gangloff and M.B. Ives, eds., NACE, Houston, TX, in press (1989).

4. R.P. Gangloff, G.E. Stoner and R.E. Swanson, "Environment Assisted Degradation Mechanisms in Al-Li Alloys", University of Virginia, Report No. UVA/526266/MS88/102, June (1988).

5. M. Gao, P.S. Pao and R.P. Wei, Metall. Trans., 19A, 1739-1750 (1988).

6. R.P. Gangloff, "NASA-UVa Light Aerospace Alloys and Structures Technology Program", University of Virginia, Proposal No. MS NASA/LaRC-xxx-88, December, 1988.

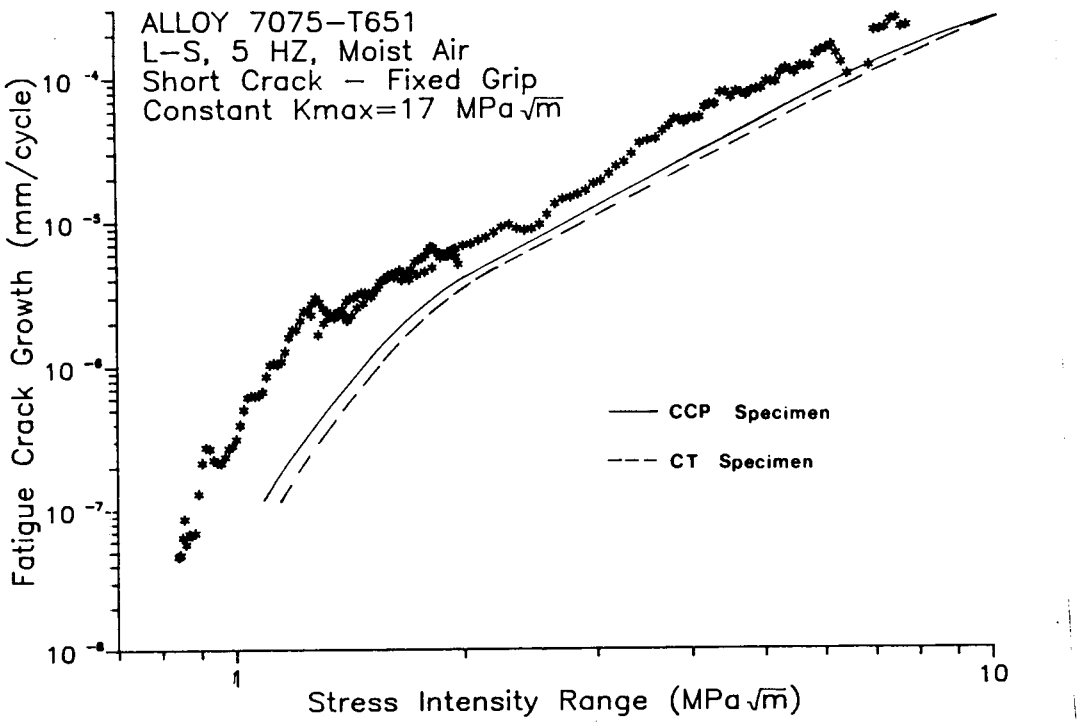

Figure 1. Near threshold intrinsic fatigue crack growth rates in alloy 7075 for; (1) Mode I loading fixed grip single edge notch (SEN) and center crack panel (CCP) specimens and (2) freely rotating compact tension (CT) specimen.

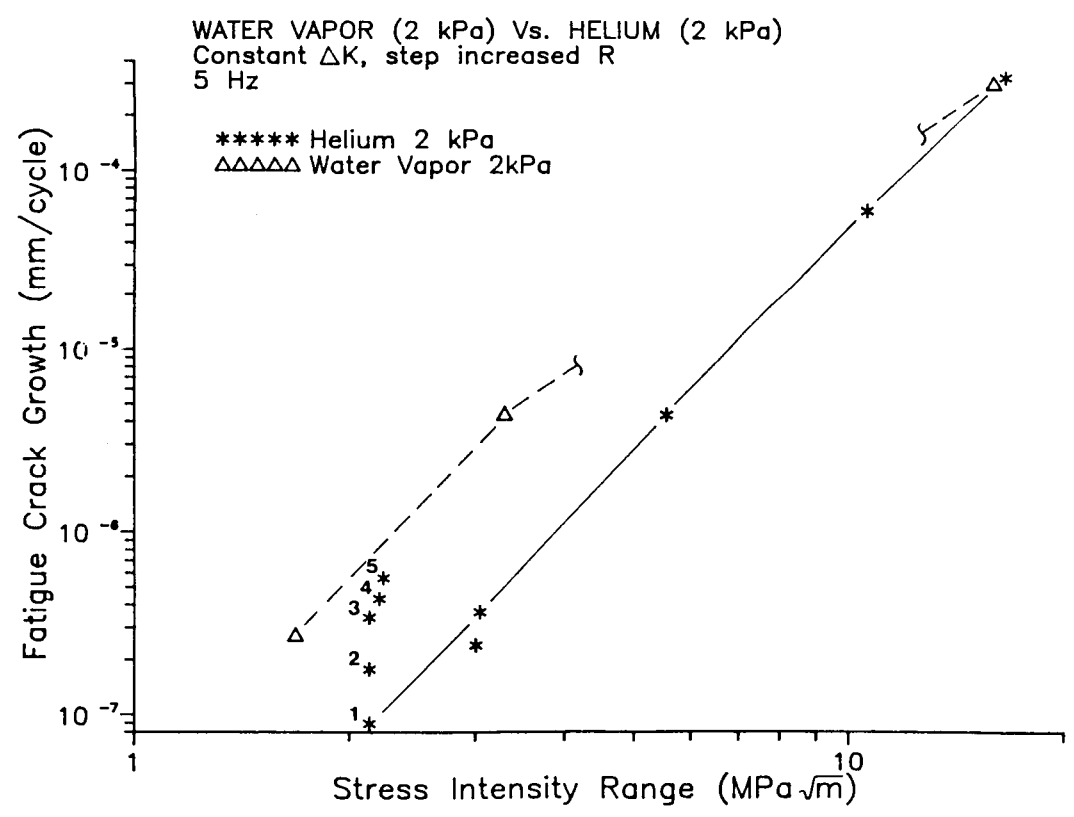

Figure 2. The fatigue crack growth behavior of alloy 2090 for water vapor and helium.

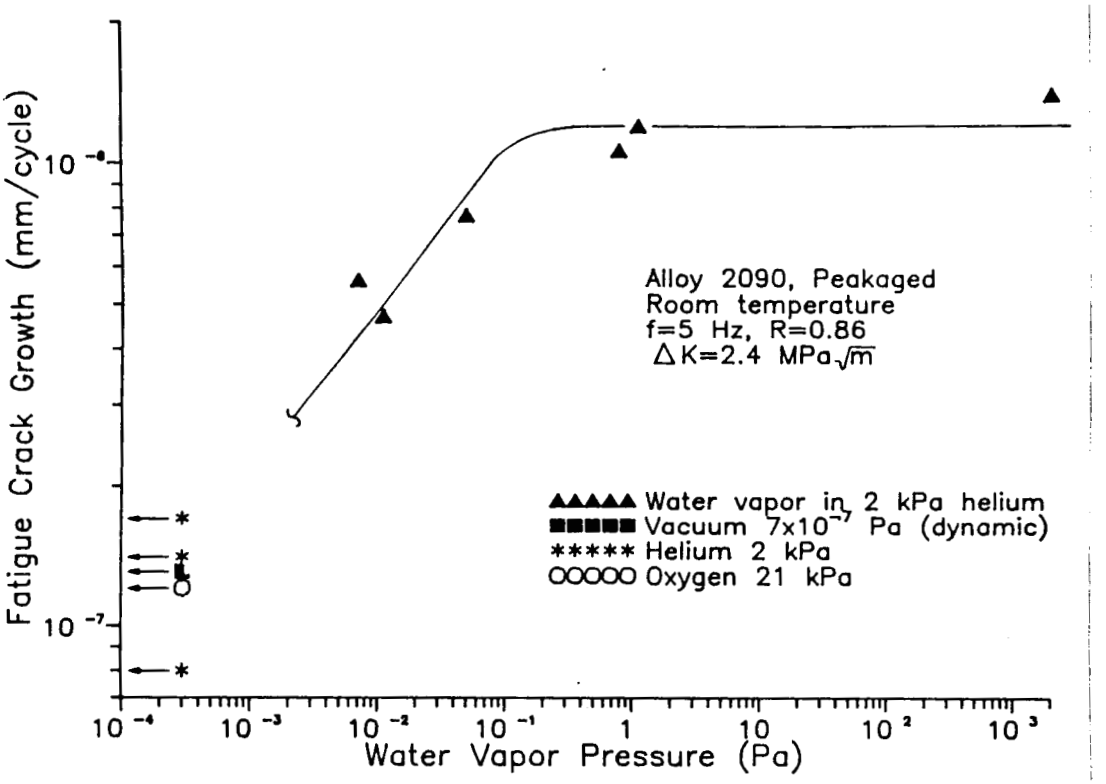

Figure 3. The effect of water vapor pressure on the intrinsic fatigue crack growth rate of alloy 2090.

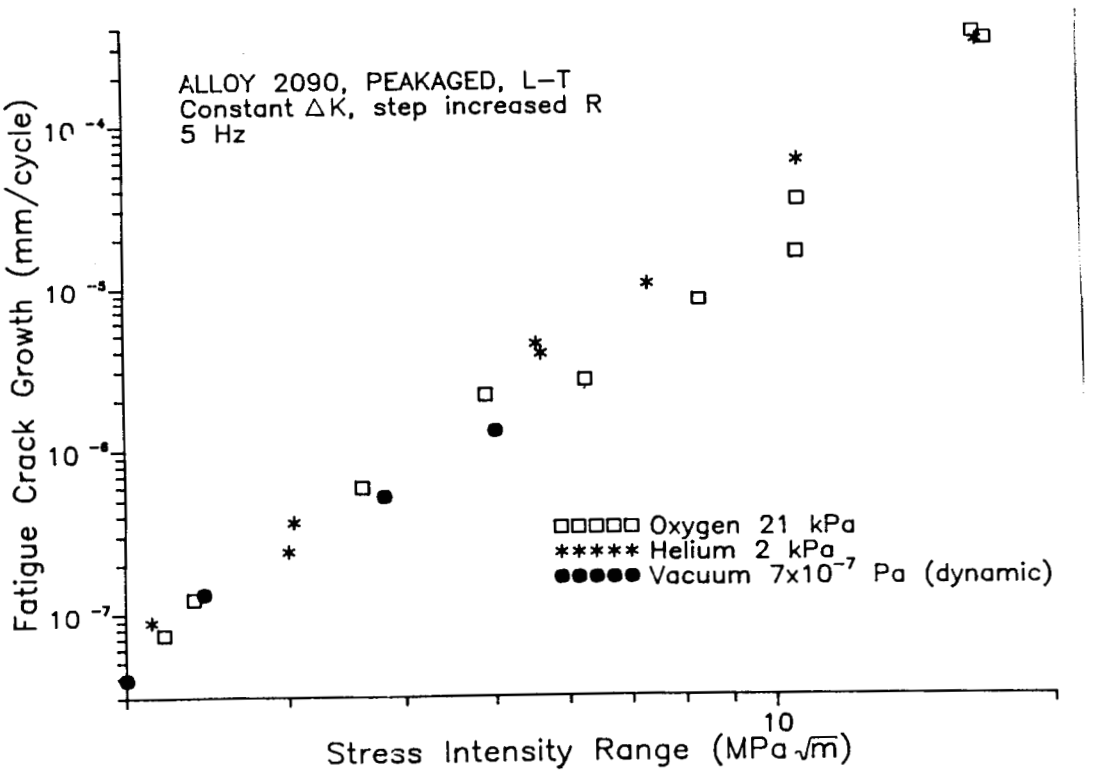

Figure 4. Intrinsic corrosion fatigue crack growth in alloy 2090 in highly purified oxygen, helium and vacuum.

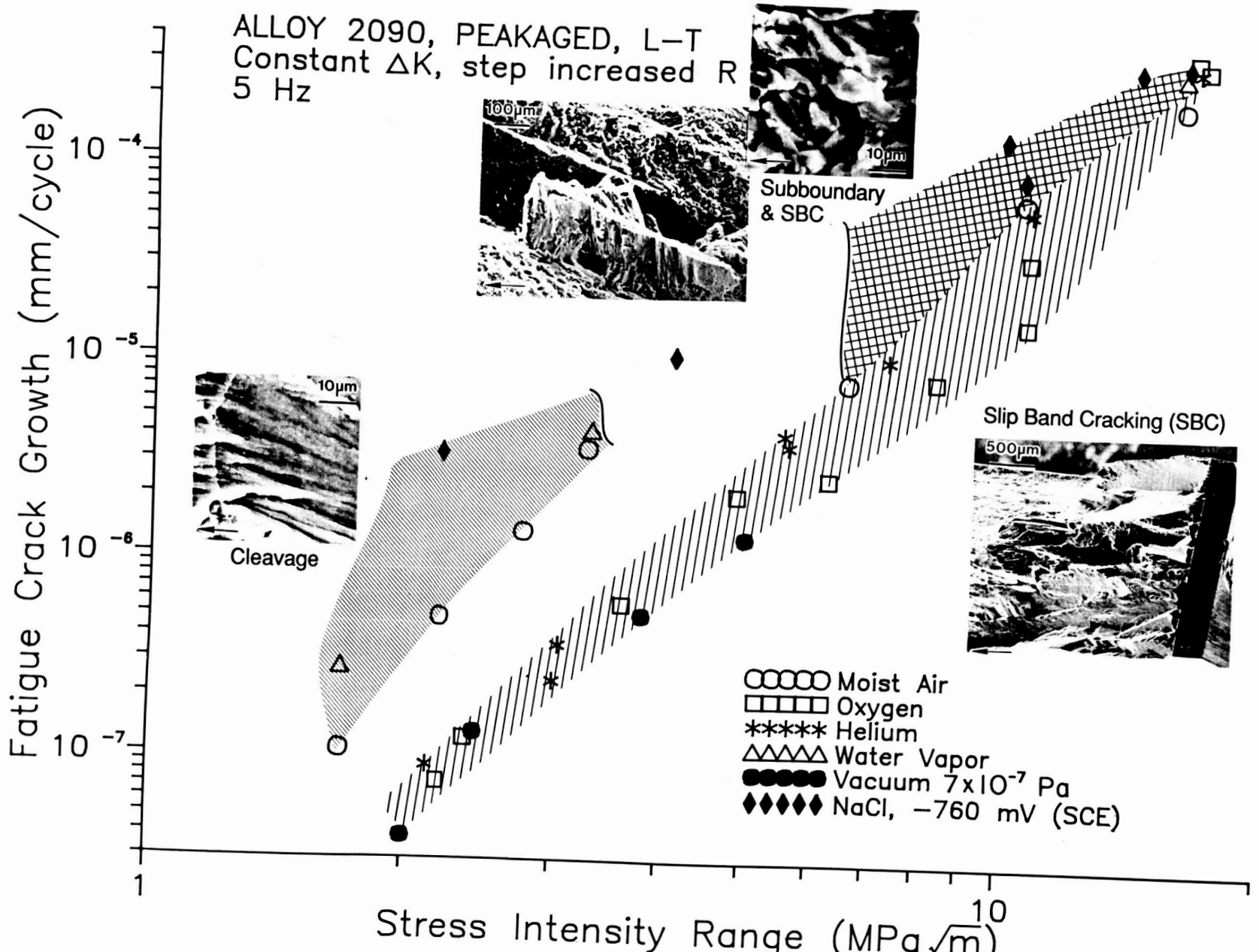

Figure 5. The three regimes of corrosion fatigue crack growth in alloy 2090; (1) inert environment slip band cracking (SBC), (2) moderate ΔK subboundary and SBC, (3) near threshold cleavage.

Program 2. MEASUREMENTS AND MECHANISMS OF LOCALIZED AQUEOUS CORROSION IN ALUMINUM-LITHIUM ALLOYS

Rudolph G. Buchheit, Jr. and Glenn E. Stoner

Objectives.

As cited in the previous report [1], the objectives of this study are:

1) to develop new or adapt existing techniques to surmount the difficulties associated with measuring and monitoring localized corrosion processes;

2) to utilize these techniques to understand the processes and mechanisms of localized corrosion and embrittlement of aluminum-lithium alloys.

Approach.

As outlined in the previous report [1], research efforts have been focused in the following areas:

1) Identification of the effect of copper dissolution and reduction in localized corrosion phenomenon;

2) Isolation of the factors which control the evolution of occluded environment chemistry in aluminum-lithium alloys;

3) Identification of the mechanisms causing localized corrosion.

Results.

Corrosion Behavior of Alloyed Copper. In a study of the corrosion behavior of the Al_2Cu intermetallic compound using a rotating disc electrode technique, Mazurkiewicz and Piotrowski noted that copper deposits formed on the counter electrode after some time [2]. Similarly, artificial crevice experiments performed with alloy 8090 (Al-Li-Cu-Mg) showed evidence that copper was physically transported through solution and deposited at some preferred site [3]. Deposition of metallic copper is commonly observed during artificial crevice experiments performed on peak aged 2090 and 2024-T6 in this study.

From these observations it is clear that copper ions are transported from one location to another during the corrosion

process. This process occurs despite the fact that the thermodynamic state of the system is not favorable for the existence of copper in its ionized state [4].

A copper ion selective electrode was used to detect the Cu^{2+} concentration; if measurable. Shavings of 2024-T6 were immersed in acidified 3.5 w/o NaCl solution. The solution was decanted periodically and a measurement was made. The Cu^{2+} concentration was never measured to be greater than 1.5×10^{-7} moles/liter. This value was on the lower end of the linear response range of the electrode. It is believed that little or no Cu^{2+} was present in solution.

Interrupted crevice experiments were performed to monitor the development of copper deposits forming at the mouths of artificial crevices. Copper deposits were first identified after 150 minutes of immersion.

Mazurkiewicz and Piotrowski concluded that since the copper content in solution was measured to be less than 10^{-8} moles/liter at any time, the copper did not participate in the corrosion process. The results obtained in our artificial crevice experiments are in general agreement with those presented by Mazurkiewicz and Piotrowski. However, conclusions regarding the role of copper or copper deposition near a crevice are premature.

During the crevice activation process, it is likely that crevice corrosion is occurring under cathodic control. There is evidence to suggest that deposits of copper form before or during this activation process. Copper can contribute to the total cathodic current in two ways. The reduction of copper by:

$$Cu^{2+} + 2e^- == Cu(s) \qquad \text{(eq. 1)}$$

occurs as copper deposits. Copper can also contribute to cathodic current by facilitating hydrogen reduction as illustrated in the table below.

TABLE 1. Exchange Current Densities and Hydrogen Overpotentials for Aluminum and Copper*

	i_o --A/cm^2	η --V
Aluminum	3.16×10^{-10} [4]	very large [4]
Copper	3.16×10^{-7} [4]	0.19 [5]

* In the presence of 1 M H_2SO_4

Though copper effects may contribute, consumption of dissolved oxygen by reduction and metal cation hydrolysis appear to be the primary cause of both the potential and pH transients observed in artificial crevice experiments [6].

Depletion of the dissolved oxygen supply occurs when the rate of oxygen diffusion into the crevice occurs more slowly than the rate of the reduction reaction. Depletion reduces the amount of cathodic activity occurring in the crevice making the crevice a net anode. This process is termed 'activation' and is marked by the sudden drop in crevice potential relative to the measured bulk potential.

The pH transient appears to be the result of competing reactions occurring in the crevice. Oxygen reduction occurs until depletion according to:

$$O_2 + 2H_2O + 4e^- == 4OH^- \qquad \text{(eq. 2)}.$$

The dominant aluminum hydrolysis reaction reported to occur is:

$$Al^{3+} + H_2O == AlOH^{2+} + H^+ \quad K_{form} = 1.07 \times 10^{-5} \qquad \text{(eq. 3)}.$$

These reactions compete in the sense that the oxygen reduction tends to make the crevice solution alkaline while the hydrolysis reaction drives the solution in the acidic direction.

Figure 1 shows a plot of pH versus time for a crevice in 2090 which is coupled to aerated bulk 3.5 w/o NaCl solution and a calculated pH versus time curve based on the above reactions. This simple calculation which neglects diffusion between the crevice and bulk solutions reasonably approximates the experimental data. Appendix 1 details the method used to generate the calculated response.

Evolution of Crevice Chemistry. As illustrated above, acid-base reactions and oxidation-reduction reactions are known to contribute to the development of crevice chemistry [7]. Acid-base reactions like the monomeric hydrolysis of Al^{3+} and Mg^{2+} occurs with the production of protons hence the generation of an acidic solution [8]:

$$Al^{3+} + nH_2O == Al(OH)^{(3-n)} + nH^+ \qquad n = (1,2,3,4) \qquad \text{(eq. 4)}$$

$$Mg^{2+} + nH_2O == Mg(OH)^{(2-n)} + nH^+ \qquad n = (1,2) \qquad \text{(eq. 5)}$$

The hydrolysis of Li^+ is different from that of Al^{3+} and Mg^{2+}. Because of its high space charge density, Li^+ is only slightly hydrolyzed and the hydrolysis product LiOH is almost completely dissociated in all but the most concentrated of aqueous solutions:

$$Li^+ + H_2O == LiOH(aq) + H^+ \qquad \text{(eq. 6)}.$$

As a result, an alkaline crevice can develop in aluminum-lithium alloys under certain conditions [9].

In crevice corrosion situations oxidation and reduction reactions are isolated from one another due to the development of corrosion macrocouples. In real crevice corrosion situations, the dominant cathodic reaction is oxygen reduction (eq. 2). Corrosion macrocouples arise due to the restricted diffusion of oxygen into a crevice. The limited availability of oxygen inhibits the cathodic activity within the crevice causing the crevice to become a net anode. Metal oxidation then becomes the dominant electrochemical reaction. Surfaces near the crevice which are freely exposed to oxygen act as the net cathode for the crevice and a corrosion macrocouple is established.

Shavings experiments were performed for 1100 aluminum, peak aged 2090 and 2024-T6 to measure the effect of hydrolysis on crevice solution pH. Artificial crevice experiments were performed to assess the effect of corrosion macrocouples on crevice pH. The experimental procedures used and the results obtained are detailed in the papers appended to this report.

Mechanisms of Local Surface Attack. Optical and scanning electron microscopy of corroded peak, aged 2090 surfaces revealed two distinctive types of localized attack (Figs. 2,3). The first type was pitting along subgrain boundaries. This type of attack increased in severity with increased aging time. This type of attack has been attributed to the T_1 phase (Al_2CuLi) which is known to precipitate on subgrain boundaries [10].

The second type of attack is a form of gross pitting associated with Al-Cu-Fe constituents found in 2090 plate. This type of attack is temper independent. In this case, a galvanic effect between the constituents and matrix is believed to operate. The constituents, being more noble than the surrounding matrix, act as local cathodes causing aggressive local corrosion at their periphery. An occluded environment develops which facilitates localized, crevice-type corrosion resulting in gross pitting.

The experimental techniques used to investigate these mechanisms and the results of those experiments are detailed in the paper contained in Appendix 1.

Electrochemical Characterization of T_1. Presently there is some controversy regarding the effect of T_1 on the localized corrosion of Al-Li-Cu alloys. One argument for preferential subgrain boundary dissolution is based on the selective dissolution of T_1 precipitates at the boundary [11]. A second argument states that the precipitates free zone along the boundary is preferentially attacked and the T_1 precipitates remain intact [12]. Currently, little quantitative ancillary data on the corrosion behavior of T_1 has appeared in the literature.

A T_1 ingot was cast and prepared for electrochemical measurements which included open circuit potential determination, potentiodynamic polarization and galvanic coupling to solution heat treated 2090. Results showed that in deaerated 3.5 w/o NaCl the corrosion potential was about -1100 mV SCE. A potential independent current regime is exhibited by T_1 during anodic potentiodynamic polarization. However, the measured current density of 5×10^{-4} A/cm^2 is not typical of corrosion through a passive film. When galvanically, coupled to solution heat treated 2090, T_1 behaves as the couple anode. Measured currents were between 5 and 15 uA. These results suggest that T_1 is indeed more active than 2090.

Summary

1) Experiments performed to date do not conclusively identify the role of Cu or Cu^{2+} in potential and pH transients in artificial crevice experiments. However, competing oxygen reduction and acid hydrolysis can be used to model the pH transient in artificial crevice experiments.

2) Consequently, corrosion macrocouples and hydrolysis of metal cations can be used to explain the pH versus time response in shavings and artificial crevice experiments.

3) Two different types of surface attack have been identified:

a) sub-boundary pitting attributed to the selective dissolution of T_1.

b) constituent particle pitting attributed to galvanic attack and crevice-type corrosion.

4) Some elementary electrochemical experiments have been performed to characterize the behavior of Tl in aqueous chloride environments.

Future Work

1) Determination of Corrosion Currents in Solutions of Various pH. Currently, pH versus time response is being modeled for shavings experiments based on:

a) corrosion rate

b) hydrolysis equilibria

c) alloy composition and temper

d) solution pH

Presently, the corrosion rate input is an estimate because corrosion current densities for 2090 in solutions of various pH are not known. Cyclic polarization is being performed for solution heat treated in 3.5 w/o NaCl solutions of whose pH ranges from 0 to 12 to obtain the necessary corrosion rate data. Cyclic polarization gives:

a) a passive current density which can be used when crevice corrosion occurs under anodic control

b) the Tafel slope for the hydrogen reduction reaction (assumed to be the dominant cathodic reaction in the deaerated shavings experiments) which can be used to calculate the corrosion rate when crevice corrosion is occurring under cathodic control.

2) Electrochemical Characterization of Tl. The experiments described above are still in progress. Experiments will be repeated in aerated 3.5 w/o NaCl solution. These experiments will be performed in acidic and basic solutions as well.

3) Corrosion Through Lithiated Films. These experiments will be performed to determine if a film on pure aluminum containing Li^+ ions is more resistive to the passage of cations from metal to solution than a Li^+ free film. If lithium ions were incorporated into the film as defects, would their high positive charge density present a barrier to the passage of other cations through the film?

To answer this question, 1100 aluminum will be subjected to anodic potentiostatic polarization in solutions of LiCl, NaCl and KCl. After forming films in the presence of all three cations, specimens would be subjected to one of two tests.

Anodic potentiodynamic polarization could be used to measure and compare passive current densities. An alternate technique would utilize electrochemical impedance spectroscopy to measure and compare the resistances of the different films.

References

1. R.P. Gangloff, G.E. Stoner and R.E. Swanson, "Environment Assisted Degradation Mechanisms in Al-Li Alloys", University of Virginia, Report No. UVA/528266/MS88/102, June, 1988.

2. B. Mazurkiewicz and A. Piotrowski, "The Electrochemical Behavior of the Al_2Cu Intermetallic Compound", Corrosion Sci., 23, 7, pp. 697-707, 1983.

3. J.C. Craig and R.C. Newman, "Local Chemistry of Stress-Corrosion Cracking in Al-Li-Cu Alloys", 4th International Conference on Aluminum-Lithium Alloys, Paris, 1987.

4. G. Kortum and J.O'M. Bockris, Textbook of Electrochemistry, Vol. II, Elsevier, Amsterdam, 1951.

5. A. Theil and W. Hammerschmidt, Beitrage zur Kenntis der Ueberspannungserscheinungen. II. Ueber Zusammenhang zwischen der Ueberspannung des Wasserstoffs an reinen Metallen und gewissen Eigenschaften der Metalle, Z. Anorg. allgem. Chem., 132, pp. 15-35, 1923.

6. D.W. Siitari and R.C. Alkire, "Initiation of Crevice Corrosion, I. Experimental Investigations on Aluminum and Iron", J. Electrochem. Soc., 129, pp. 481-487, 1982.

7. N. Sato, "Some Concepts of Corrosion Fundamentals", Corrosion Sci., 27, 5, pp. 421-433, 1987.

8. C.F. Baes and R.E. Mesmer, Hydrolysis of Cations, John Wiley and Sons, New York, 1976.

9. N.J.H. Holroyd, A. Gray, G.M. Scamans and R. Hermann, "Environment Sensitive Fracture of Al-Li-Cu-Mg Alloys", 3rd International Conference on Aluminum-Lithium Alloys, C. Baker, P.J. Gregson, S.J. Harris, eds., Institute of Metals, London, 1986, pp. 310-320.

10. M.H. Tosten, A.K. Vasudevan and P.R. Howell, "Grain Boundary Precipitation in Al-Li-Cu Alloys", pp. 490-495, in reference 8.

11. J.G. Rinker, M. Marek and T.H. Sanders, Jr. "Microstructure, Toughness and SCC Behavior of 2020", 2nd International Conference on Aluminum-Lithium Alloys, T.H. Sanders, Jr. and E.A. Starke, Jr., eds., TMS-AIME, Warrendale, PA, 1984, pp. 597-626.

12. C. Kumai, J. Kusinski, G. Thomas and T.M. Devine, "Influence of Aging at 200°C on the Corrosion Resistance of Aluminum- Lithium and Aluminum-Lithium-Copper Alloys", March, 1987.

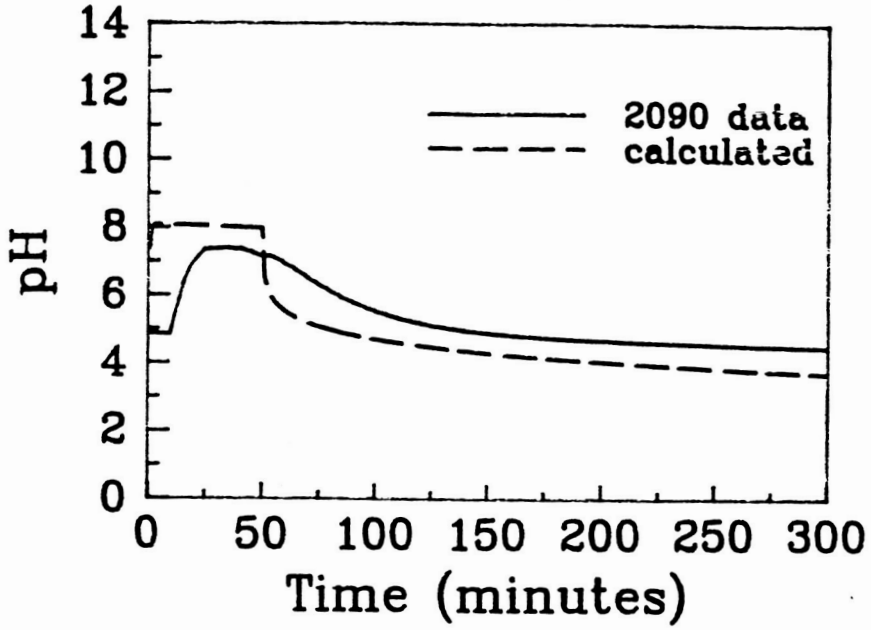

Figure 1. A plot of pH versus time for 2090 and the calculated response based on O_2 reduction and Al^{3+} hydrolysis.

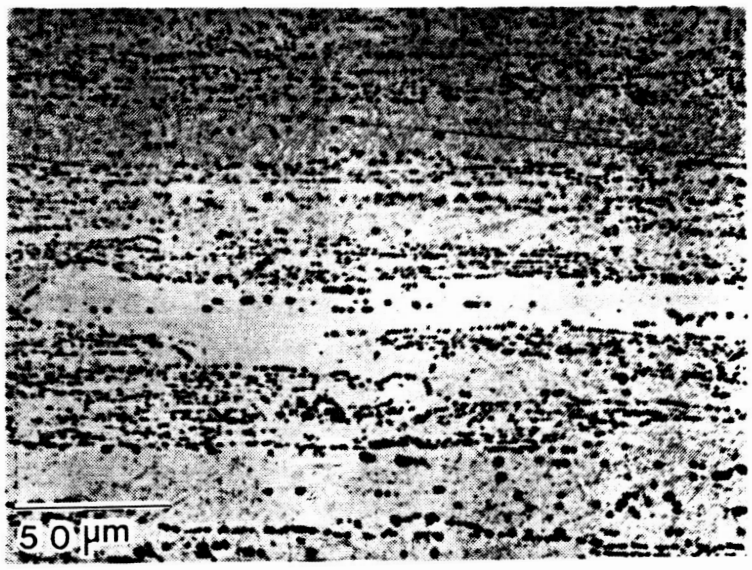

Figure 2. Optical micrograph of subgrain boundary pitting on peak aged 2090.

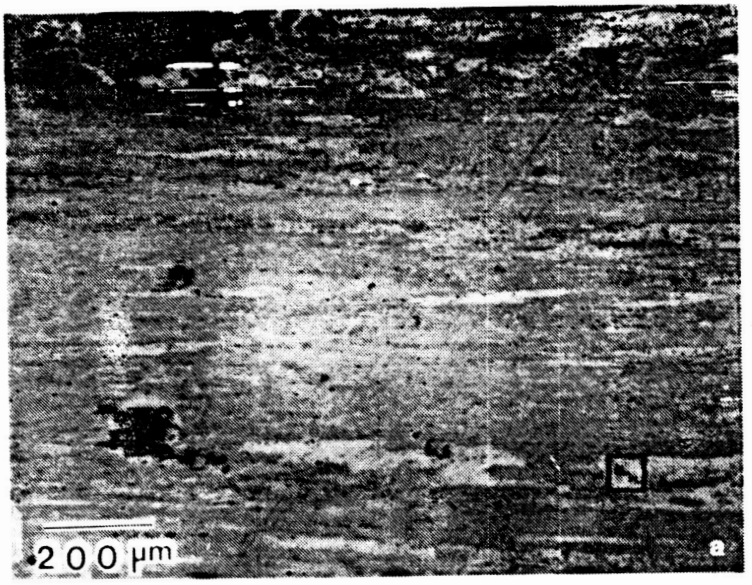

Figure 3. Optical micrograph of constituent particle pitting on peak aged 2090.

Appendix I.

The fundamental assumptions are:

1.) Crevice pH is determined by the starting pH, oxygen reduction and $Al^{3+}/AlOH^{2+}$ acid hydrolysis.

2.) Crevice corrosion is occurring under anodic control at all times.

3.) No diffusion between the crevice and bulk solution occurs.

Time Required to Deplete a Crevice of Dissolved Oxygen

Based on analysis by Oldfield and Sutton (1), the time required to consume the oxygen in a crevice of width x is given by:

$$t_d = \frac{n\ F\ C_O}{I_p}\ x \qquad \text{(eq. 1)}$$

where,

variable	value
t_d = time to depletion	(sec)
n = equivalents/mole	4 eq/mol
F = Faraday's constant	96500 C/eq
C_O = dissolved O_2 concentration	14×10^{-6} mol/cm^3
I_p = passive current density	2×10^{-6} A/cm^2
x = crevice gap	10×10^{-4} cm

Using the stated values t_d = 45 minutes.

Change in pH Due to Oxygen Reduction

Assume the reaction occurs according to:

$$O_2 + 2H_2O + 4e^- = 4OH^-$$

and operates for 45 minutes. Use,

$$n = \frac{it}{nF}$$

variable	value
m = moles O_2 consumed	(moles)
i = passive current	3.1×10^{-7} A

n = equivalents/mole	4 eq/mol
F = Faraday's constant	96500 C/eq
t = time	(sec)

to determine the number of moles of oxygen consumed at the specified corrosion rate.

Change in pH Due to Al^{3+} Hydrolysis

Assume the reaction occurs according to :

$$Al^{3+} + H_2O \rightleftharpoons AlOH^{2+} + H^+ \quad K_{form} = 1.07 \times 10^{-5}$$

The equilibrium expression is:

$$K_{form} = \frac{[AlOH^{2+}][H^+]}{[Al^{3+}]}$$

This expression is solved every 60 seconds during the simulated experiment by applying Le Chatelier's principle to the hydrolysis equilibrium. Aluminum ion concentration increases by the quantity given by corrosion rate multiplied by 60 seconds shifting the equilibrium to the right.

	time	$[Al^{3+}]$	$[AlOH^{2+}]$	$[H^+]$
equilibrium	t_o	C_1	C_2	C_3
disturbed	t_o + 60 s	$C_1 + \Delta C_1$	C_2	C_3
equilibrium	t_o + 60 s	$C_1 + \Delta C_1 - x$	$C_2 - x$	$C_3 - x$

$$C_1 = [Al^{3+}]$$
$$C_2 = [AlOH^{2+}]$$
$$C_3 = [H^+]$$

Solve

$$K_{form} = \frac{(C_2 + x)(C_3 + x)}{(C_1 + \Delta C_1 - x)}$$

for the real roots and the change in pH for that 60 second interval.

Listed below is the routine used to generate the 'calculated' pH versus time response.

```
'this pro-gram calculates a pH versus time curve in an artificial crevice
'experiment based on oxygen reduction and Al hydrolysis
OPEN "o", #1, "dat.dat"
INPUT "initial pH"; iph
hconc = EXP(-2.303 * iph)
aloh2 = 0
FOR i = 1 TO 300

        'the change in Al ion concentration in 60 sec is calculated
        almoles = almoles + 5.85E-09
        alconc = alconc + almoles

        'quadratic formula is used to solve for the real root of
        'the new hydrolysis equlibrium expression
        part1 = ((aloh2 + hconc + .0000107) ^ 2 + 4 * (.0000107 * alconc)) ^ .5
        root1 = .5 * (-(aloh2 + hconc + .0000107) + part1)

        'the new concentrations are calculated
        aloh2 = aloh2 + root1
        hconc = hconc + root1
        alconc = alconc - root1

        IF i > 50 GOTO 20      'stops oxygen reduction after 50 min

        deloh = 1.24E-06       'change in OH concentration due to reduction
        GOTO 30

20 :
        deloh = 0

30 :
        newh = hconc - deloh  'calculates the new hydrogen ion concentration

        'prevents us from taking the log of a negative number
        IF newh < 0 GOTO 40
        ph = -LOG(newh) / 2.303
        GOTO 50

40 :    'if a negative value is identified the pOH is calculated instead
        dum1 = ABS(newh)
        poh = -LOG(dum1) / 2.303
        ph = 14 - poh


50 :
        PRINT #1, i; ph
        hconc = EXP(-2.303 * ph)
NEXT i
CLOSE #1
PRINT "done"


'this pro-gram calculates a pH versus time curve in an artificial crevice
'experiment based on oxygen reduction and Al hydrolysis
OPEN "o", #1, "dat.dat"
INPUT "initial pH"; iph
hconc = EXP(-2.303 * iph)
aloh2 = 0
FOR i = 1 TO 300
```

Program 3. AN INVESTIGATION OF THE LOCALIZED CORROSION AND STRESS CORROSION CRACKING BEHAVIOR OF ALLOY 2090

James P. Moran and Glenn E. Stoner

BACKGROUND

This report represents the initial contribution from this project to NASA Grant NAG-1-745. The project is an ongoing dissertation research effort, with an expected completion date of early to mid-summer, 1989. A detailed, 100 page research summary was compiled for this project in September, 1988 [1]. Two copies were sent to Dr. W. Barry Lisagor at that time, since he is a member of the student's dissertation committee. Further copies can be made available upon request. The following is a brief review of the highlights of that summary, along with the expected goals for the next reporting period. In addition, since this is the initial contribution from this project, a brief chronological history of the project is included.

OBJECTIVES

The objectives of this project are as follows:

1) To characterize the localized corrosion and SCC initiation behavior of alloy 2090.

2) To gain an understanding of the role of localized corrosion phenomena and associated occluded cell environments in the mechanisms of initiation and early-stage propagation of stress corrosion cracks in 2090.

EXPERIMENTAL PROCEDURES

MATERIALS PREPARATION

Two 2090-type alloys were supplied by ALCOA for this study. Both were commercially prepared 38 mm ingot-cast plates that were solution heat treated and subjected to 6% deformation prior to shipping. Both plates were aged at 160°C and studied in under-aged (UA) and peak-aged (PA) tempers. Standard optical microscopy and aging data are included in the Fall 1988 report (sec. 3.1) [1]. All mechanical testing to date (both inert and corrosive environments) has been performed in the short- transverse direction. Round tensile bars, with a 3.12 mm diameter and 20 mm gage length, were utilized.

LOCALIZED CORROSION TESTING

Potentiodynamic and potentiostatic anodic polarizations were performed at both aging conditions, in 3.5 w/o NaCl solution (aerated and deaerated). The polarizations were performed in a plexiglass cell, using a Pt counter electrode and a saturated calomel (SCE) reference. An automated PAR corrosion measurement system was utilized. The specimens were finely polished, allowing microscopic examination of the corroded surfaces after polarizing.

STRESS CORROSION CRACKING EXPERIMENTAL TECHNIQUES

Alternate Immersion Time to Failure. This technique closely followed ASTM Standard G-44, for alternate immersion time to failure (TTF) SCC testing in NaCl, and ASTM G-49, for constant extension SCC testing of smooth tensile bars. ASTM G-44 requires that the tests be performed in a consistent temperature (27°C) and humidity (45%). In addition to this standard technique, TTF experiments were conducted under ambient conditions of near 100% relative humidity. Times to failure for 2090-UA were compared for these two methods at identical stress levels.

Slow Strain Rate (SSRT) SCC Experiments. The SSRT experiments were performed on a CORTEST 6 Kip slow extension rate load frame interfaced to a personal computer for data acquisition. A more detailed description of the apparatus and developed software is included in the Fall 1988 report (sec. 2.3.2) [1]. The SSRT tensile specimens were exposed to deaerated NaCl solution, at various strain rates and electrochemical conditions (both free corrosion and applied potential). The data are presented in the relatively standard format of ductility as a function of strain rate or applied potential. In addition, composite plots of corrosion current and applied load as a function of time (or strain) are presented to illustrate electrochemical current-strain-load interactions.

Constant Immersion TTF Experiments in Selected Environments. For these experiments, ASTM G-49 stressing frames were used to load tensile bars to 35 ksi (roughly 55 to 65% of yield). The specimens were then immersed in selected 3.5w/o NaCl-based environments. Additions to the solution included, LiCl, Na_2CO_3 and Li_2CO_3. These experiments were performed based on the findings reported by Newman et al. regarding the effects of carbonate additions to NaCl on the SCC behavior of alloy 8090 (this work is reviewed in the Fall 1988 report; pg. 25) [2,3]. Several of the environments chosen here were similar to those used by Newman, along with several new environments chosen to clarify the roles played by the various species added.

In addition to the SCC tests, polarization experiments were performed in many of the same environments. A summary of all test environments is presented elsewhere [1].

RESULTS AND DISCUSSION

LOCALIZED CORROSION

The potentiodynamic polarization behavior of alloy 2090C is summarized in Table 1. Concentrating on the deaerated data, a comparison of the two tempers reveals that a slightly more active breakaway potential is exhibited by the peak-aged specimen. A similar trend is present in the repassivation data. This suggests that increased aging, and therefore increased grain/subgrain boundary precipitation, renders alloy 2090 slightly more susceptible to pitting corrosion. As further evidence, an increased concentration of grain/subgrain boundary pitting was observed for the peak-aged temper.

A second type of pitting was attributed to the Al-Fe-Cu constituent particles inherent in this alloy. Although these pits were much less frequently observed relative to boundary pits, the were typically quite large (on order of a few hundred microns). Continuous subgrain boundary attack was observed in the regions surrounding these large pits. This attack was attributed to the development of a low pH (pH=4) occluded environment within these large pits.

A thorough account of the localized corrosion behavior of alloy 2090 is presently being compiled for publication, and is included in Appendix 1 of this progress report [4].

ALTERNATE IMMERSION RESULTS

Time to failure (TTF) data for alloy 2090B (UA) is illustrated in Figure 1 for both normal ambient lab conditions and controlled 100% humidity. The TTF's under normal lab conditions are similar to those determined at ALCOA [5]. A significant increase in TTF is observed, however, under 100% humidity.

The 100% humidity experiment was performed because there was no means of actively controlling the ambient conditions surrounding the alternate immersion tank, as prescribed by the ASTM standard. Clearly, the two-part "bulk-environment/ local-environment" cycle, which is obtained under 100% humidity, is not representative of the three-part "bulk-environment/local-environment/drying" cycle employed in the standard test. Therefore, any future TTF experiments will be performed under normal ambient conditions, with any

atmospheric fluctuations being carefully monitored and reported with the test results.

SLOW STRAIN RATE RESULTS

Figure 2 illustrates one primary method of displaying data from a SSRT experiment. The exposed specimen area (for current density calculation) is continuously recalculated, based on the elastic and plastic strain at each data point. Note that the corrosion current shows a marked increase near the vicinity of the onset of plastic deformation, followed by a steady state current again being obtained once the loading rate is reduced to practically zero. Typically, there is some time lag between the onset of plastic deformation and the observance of increasing current. A similar time lag occurs between the end of increasing load and steady state current again being attained. This current increase is not uniquely dependent on plastic strain. It is also not solely dependent on load.

Scatter in the yield strength data has aided in the determination of current evolution during loading. For two given specimens at a specific load, one can be below its yield strength, while the other is above its yield strength. Only the specimen above its yield strength will exhibit a current increase. Figure 3 supplies more evidence. In this experiment, the applied extension was stopped intermittently, and the corrosion current was monitored. A corrosion current time lag similar to that described above is seen, in particular at the start of the final (and largest) load plateau. Eventually, the current levels off and remains at a relatively high value, even without continued straining. Apparently, the only necessary condition for producing this increased corrosion current is an applied load above the yield strength.

The effects of strain rate on ductility are illustrated in Figures 4 and 5 for UA and PA tempers (no detectable trends were evident in the yield strength or ultimate tensile strength data). Each plot includes the ductility data gathered in dry argon, at a strain rate of 5.4E-7 /sec. The first and most obvious observation is that there is considerable scatter in the data. This should not seem surprising when one examines the data gathered in an argon environment, where considerable scatter is observed for both tempers. This is an intrinsic problem with this alloy, particularly when tested in the ST direction (in the Fall 1988 report [1], an attempt is made to explain some of the anomalous data points in Figures 4 and 5).

Even given the scatter, however, a trend in the data can be seen (particularly for the under-aged temper). For both tempers, ductility decreases with increasing strain rate over 1.5 decades. This trend is consistent with the film rupture/ dissolution theory of environmental fracture. In particular,

this would be consistent with a material governed by the dissolution model with a relatively high localized corrosion rate. Increasing the strain rate increases the frequency of film rupture at the crack tip, thereby keeping the dissolution reaction concentrated at the tip, relative to the crack walls. This will yield a sharp crack of high stress intensity, which should continue propagating. As the strain rate is lowered (along with an associated decrease in the frequency of bare metal exposure), the corrosion becomes less concentrated at the crack tip, and blunting can occur. This lowers the stress intensity and reduces the crack growth rate.

CONSTANT IMMERSION TTF EXPERIMENTS IN SELECTED ENVIRONMENTS

This investigation was initiated based on a study performed by Craig, Newman et al. [2,3]. The pertinent aspects of the work performed by Craig, et al. [2,3] are reviewed in the Fall 1988 report (pg. 25) [1]. In summary, they found that 8090, constantly immersed in NaCl solution, would not stress corrosion crack. Removal from solution after several days and placement in lab air resulted in very quick fracture, while removal and placement in a CO_2-free environment did not produce fracture. They proposed that the role of CO_2 was to provide a $Cl^-/CO_3^=$ environment of the proper pH for passivation by $LiAlO_2$. Additions of Li_2CO_3 to the NaCl solution produced rapid failure under constant immersion conditions.

The experiments discussed above were repeated on 2090 by this author, and the results were perfectly duplicated. They are summarized in Table 2. Constant immersion in NaCl containing 0.1M Li_2CO_3 yielded greatly accelerated TTF's, relative to straight NaCl, as seen in Table 3. Those immersed in straight NaCl suffered from severe pitting and surface discoloration, while those in Li_2CO_3 exhibited no evidence of macroscopic localized corrosion. This is consistent with Craig's argument of improved passivity in the presence of $CO_3^=$.

Several other environments were also investigated, in an effort to isolate the relative roles of Li^+ and $CO_3^=$. The results are presented in Table 3, and the key points will be summarized in the following paragraphs (see the Fall 1988 report [1] for a thorough review). Occluded cell pH vs. time measurements were also performed. The steady state pH values are summarized in Table 4.

To isolate the role of $CO_3^=$, 0.1M Na_2CO_3 was substituted for Li_2CO_3. The results were dramatically different. Severe surface attack and discoloration occurred almost immediately, and fracture times were significantly increased. Many samples did not fracture after 30 days (similar to straight NaCl). Clearly, there is a major difference between these two cations.

To isolate the role of Li^-, LiCl was added to NaCl solution (pH=10). The NaCl concentration was altered to keep a consistent Cl^- concentration. SCC times to failure for this environment slightly increased, relative to NaCl, but were still far greater than Li_2CO_3. As seen in Table 4, however, the pH did not remain at 10 within the crevice. Therefore, one can only speculate as to whether the change in SCC performance is due to the lack of $CO_3^=$ or the pH change. Similarly, an attempt to isolate the role of pH (pure NaCl; pH 10) also proved inconclusive, since the local pH rapidly decreased.

Compositional effects were also investigated. To investigate the role of the lithium in the alloy, an Al-Cu-Mg alloy 2024 was subjected to all of the above test environments. As is seen in the tables, its performance was similar to that of 2090. The one anomaly between 2024 and 2090 was in the "constant immersion/removal to lab air" experiment. Upon removal from the NaCl, 2024 did not fracture after 60 days.

Table 6 summarizes the polarization behavior of alloy 2090C in the above environments. Consistent with the observed surface corrosion, Na_2CO_3 exhibits a "passive" current density almost 2 orders of magnitude higher than Li_2CO_3. Note in Table 5 that K_2CO_3 behaved similar to Na_2CO_3. It is clear that Li_2CO_3 has unique characteristics, relative to other alkali metal carbonates. Although addition of Li_2CO_3 to NaCl does not change the passive current density, the corrosion potential is lowered slightly and the breakaway potential is increased by about 100 mV. The polarization behavior of LiCl/NaCl was basically identical to that of pure NaCl.

The mechanism by which Li_2CO_3 dramatically and uniquely affects the corrosion behavior is still unclear. In addition to the mechanism proposed by Craig (precipitation of $LiAlO_2$), we are presently considering the possibility of passivation by precipitation of Li_2CO_3. The low solubility of Li_2CO_3 (see Table 5) could result in precipitation within occluded cells, where the Li^+ concentration will tend to increase. The obvious next step for this part of the project is to gain a better understanding of the different characteristics of the alkali metals, paying particular attention to the unique qualities of Li_2CO_3.

FUTURE WORK

The addition of selected cation/anion combinations and their effects on occluded environments and SCC behavior are clearly the most dramatic findings to date. The primary focus of the remaining work will be toward a better understanding of these effects. In addition, SSRT experiments will be continued

to examine further the role of plastic deformation and increasing corrosion current in the SC initiation process. The following is a list of proposed activities for the next reporting period :

* Finish paper on localized corrosion of 2090 (ref. 4) and submit it to a refereed journal. Prepare manuscript on $CO_3^=$ effects for Al-Li V Proceedings.

* Defend dissertation outline in late January, 1989.

* Continue SSRT experiments, concentrating on the under-aged temper (less inherent scatter).

  - Develop ductility vs. strain rate data for selected applied potentials

  - Perform non-standard loading ramps in an effort to determine the origin of increasing corrosion current.

* Continue constant immersion TTF experiments in selected bulk environments. This is aimed at determining the mechanism by which Li_2CO_3, (or simply the presence of CO_2) enhances stress corrosion crack initiation.

CHRONOLOGICAL HISTORY OF PROJECT

I. Year 0 to Year 2

A. Literature review of SCC mechanisms in Al alloys.

B. Laboratory set-up.

1. Construction and standardization of an alternate immersion SCC facility.

2. Construction of a slow strain rate (SSRT) SCC facility.

a. Integration of mechanical and electrochemical equipment.

b. Development of extensive data acquisition and analysis software.

c. Calibration and standardization.

3. Microstructural and mechanical characterization of several candidate Al-Li-Cu alloys.

II. Year 1.5 to Year 2.5

A. Alternate Immersion time to failure experiments on 2090 and 2024 in various ambient environments.

B. SSRT experiments on 2090 and 2024, using various strain rates, electrochemical conditions.

III. Year 2 to Year 3

A. Localized corrosion studies of 2090, using polarization techniques.

B. Further SSRT experiments.

C. SCC initiation experiments in various NaCl-based solution chemistries.

IV. Year 3 to Year 3.5 (present)

A. Compilation of Research Summary Report.

B. Occluded cell pH experiments in NaCl-based environments.

REFERENCES

1. J.P. Moran; "An Investigation of the Mechanisms of Localized Corrosion and Stress Corrosion Cracking of Alloy 2090 - A Literature Review and Research Summary"; A progress report submitted to the dissertation committee. The University of Virginia. September, 1988.

2. J.G. Craig, R.C. Newman, M.R. Jarret and N.J.H Holroyd; Conference Proceedings of the International Conference of Environmental Degradation of Engineering Materials, Pennsylvania State University, 1987.

3. J.G. Craig, R.C. Newman, M.R. Jarret and N.J.H. Holroyd; Proceedings of the Fourth International Al-Li Conference, Paris, June, 1987.

4. R.G. Buchheit, Jr., J.P. Moran, G.E. Stoner and K.A. Coyne; "An Investigation of the Localized Corrosion Behavior of Alloy 2090", to be submitted to Corrosion, Jan, 1989.

5. Steve Byrne and Ed Colvin, ALCOA Technical Center; Personal Communication, Fall, 1987.

TEMPER	A/D*	E_{corr}	i_{pass}	E_{br}	E_{rp}	E_{corr}'
UNDER-Aged	A	-725±10	---	-710±8	-740±12	-905±22
PEAK-AGED	A	-735±13	---	-720±7	-754±14	-920±16
UNDER-Aged	D	-916±23	1.0	-690±1	-720±8	-908±12
PEAK-Aged	D	-892±35	0.5	-725±10	-739±6	-920±25

* A=Aerated; D=Deaerated.

TABLE 1 : Anodic polarizarion data for Alloy 2090C.
Potential values include standard deviation (n-1).
(Units: Potential = mV vs SCE ; Current Dens. = $\mu A/cm^2$)

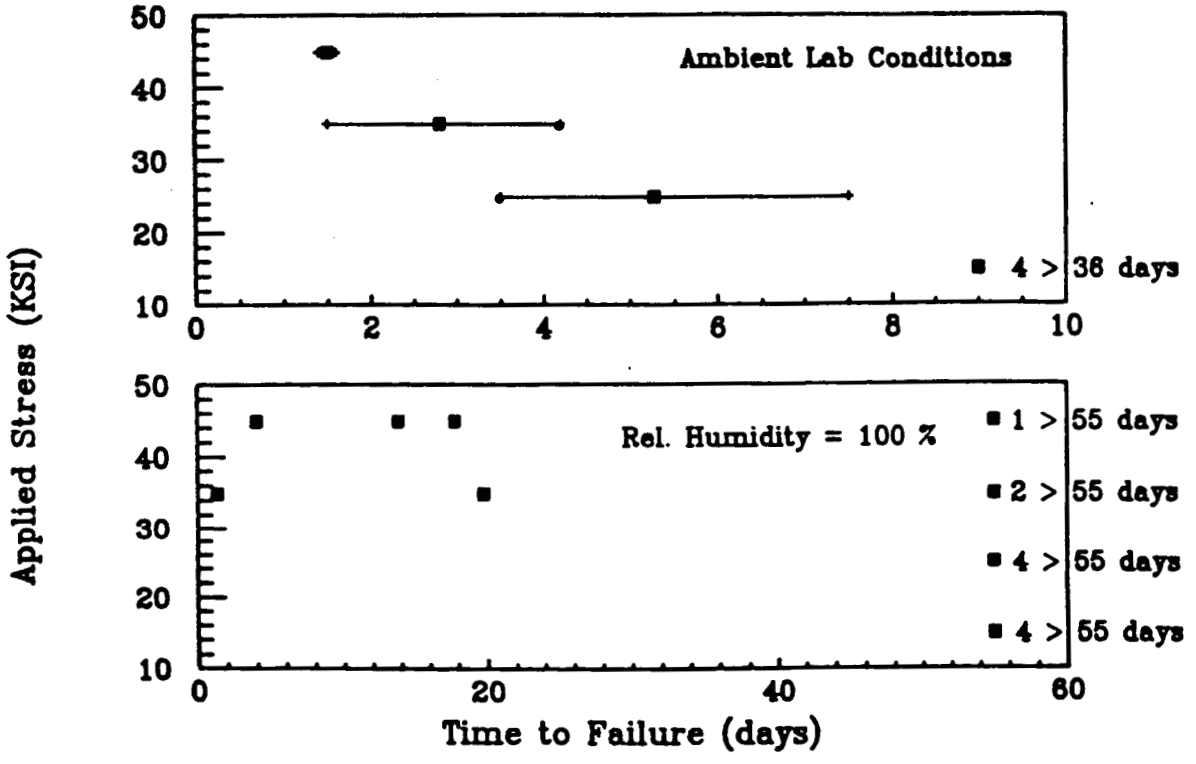

Figure 1 : Alternate Immersion Time to Failure Data for Alloy 2090B.

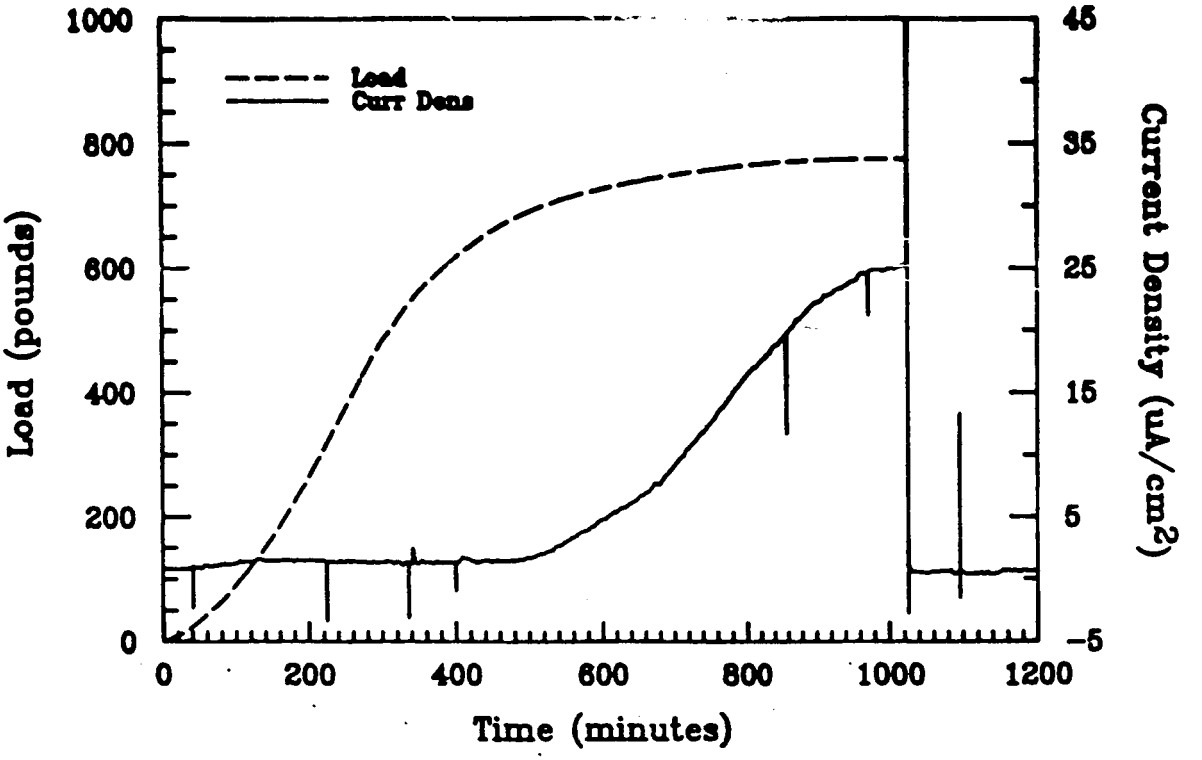

Figure 2 : SSRT Data Plot Illustrating Load and Current as as Function of Time.

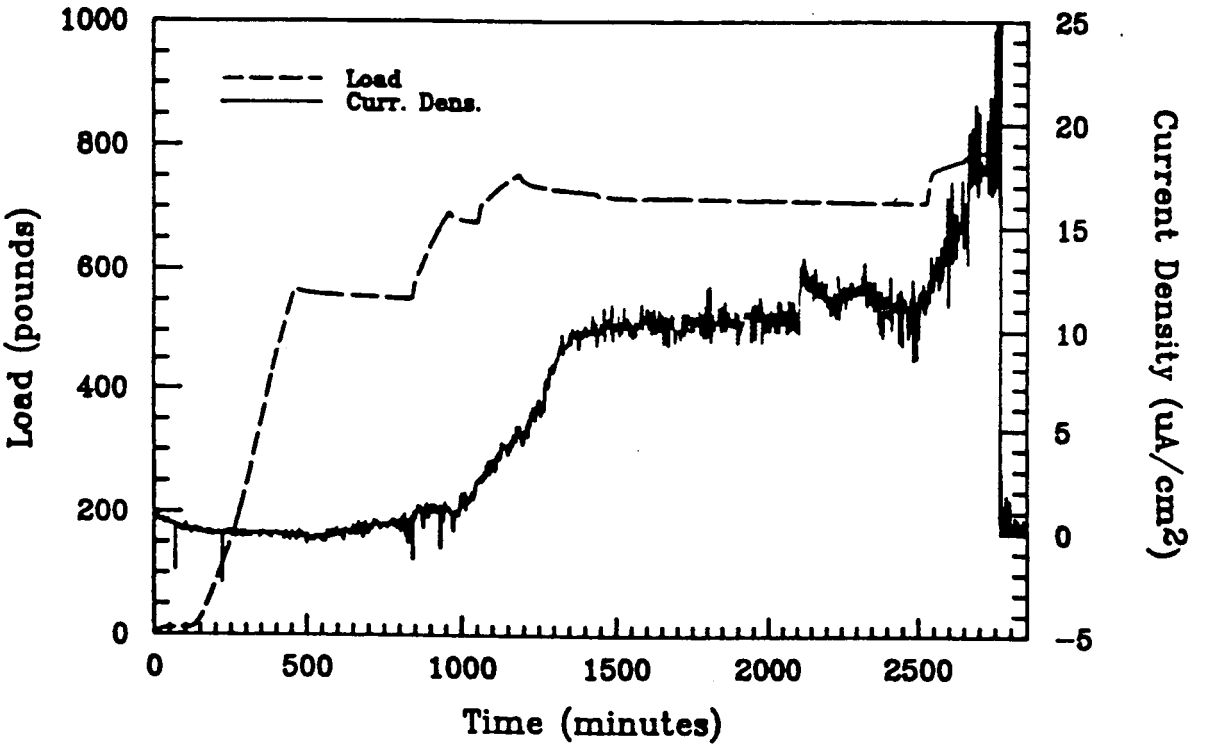

Figure 3 : SSRT Data Plot Illustrating the Effects of Constant Load and Constant Strain on the Corrosion Current.

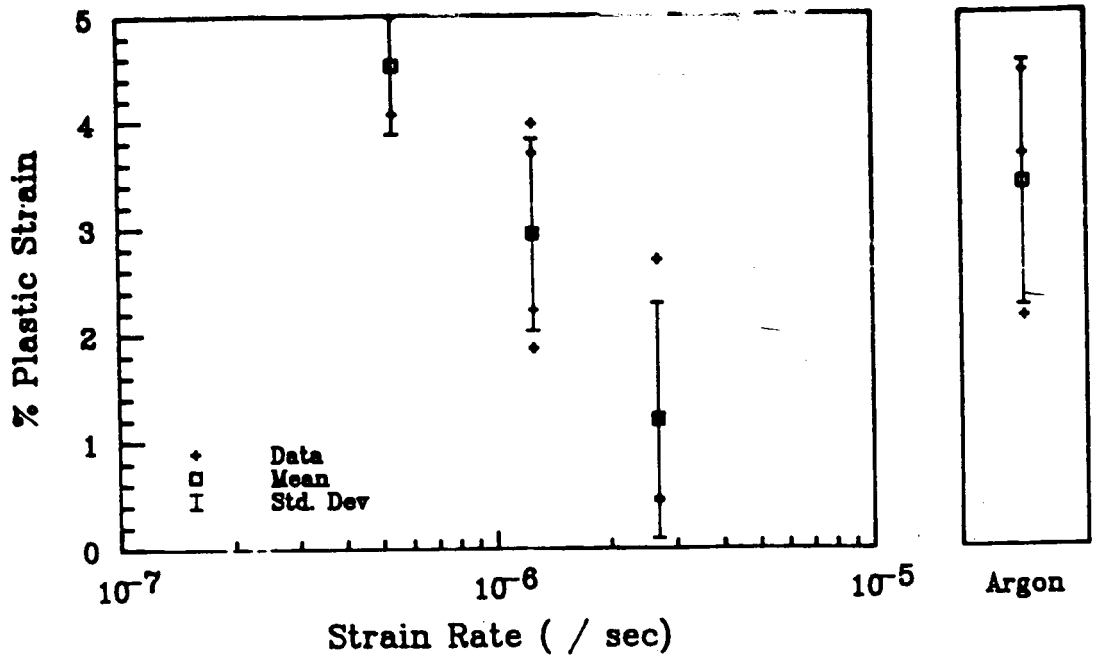

Figure 4 : SSRT Data; Ductility as a Function of Nominal Strain Rate. Alloy 2090C-UA. Applied Potential= -715mV vs SCE.

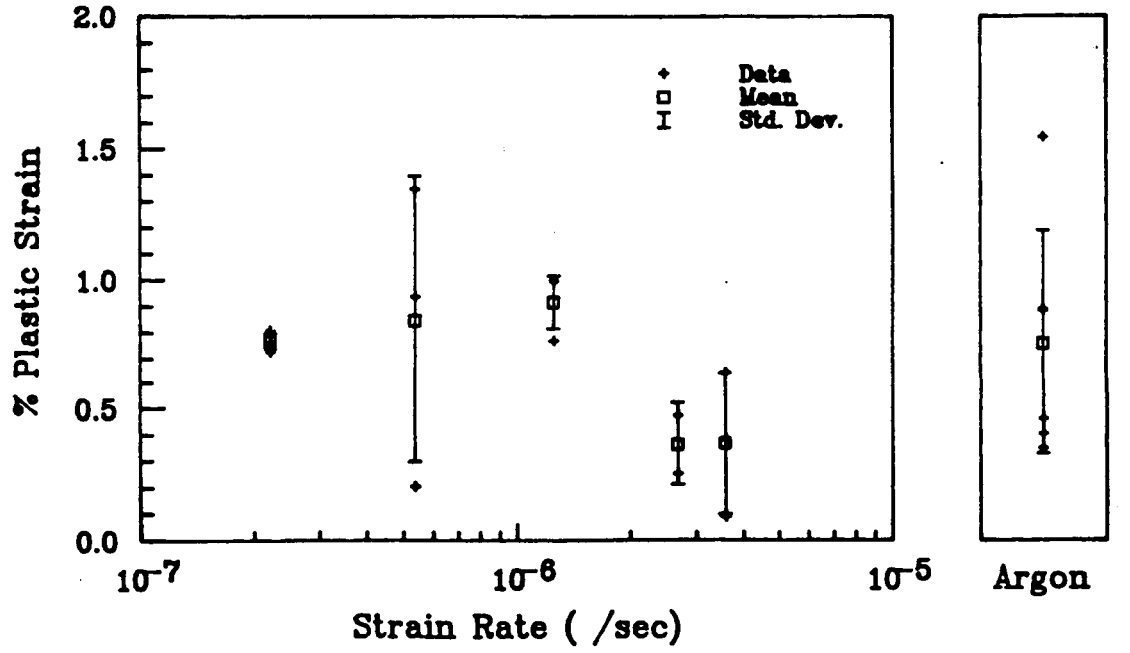

Figure 5 : SSRT Data; Ductility as a Function of Nominal Strain Rate. Alloy 2090C-PA. Applied Potential= -730mV vs SCE.

Environment	ALLOY 2024	2090B
Lab Air	4@ > 60	4@ 0.6±.1
CO_2 - Free (dry NaOH)		4@ > 60
CO_2 - Free (wet NaOh)	4@ >60	3@ >60 1@ 50-52

TABLE 2 : Times to Failure (days) in various environments after constant immersion in NaCl for 7 days.

ADDED SPECIES*	pH	ALLOY 2024	2090C UA	2090C PA
none	7	4@ >75	2@ >30	2@ >30
none	10	4@ >75	2@ >30	2@ >30
LiCl	10	4@ >75	4@ 15±3	6@ 10.7±2.7
Li_2CO_3	10	4@ 5.7±1.5	4@ 1±.3	3@ .7±.1 1@ 9.0
Na_2CO_3	10	4@ >75	2@ 16±2 2@ >60	2@ 8±0 2@ >60
Na_2CO_3	7-9		2@ 6	2@ 2±.5

* All environments have aerated 3.5 w/o NaCl as their base, with 0.1 M of the listed species added. The exception is LiCl, where 0.2M LiCl was added to 2.6 w/o NaCl, in an effort to keep Cl^- and Li^+ concentrations consistent with Li_2CO_3.

TABLE 3 : A summary of Times To Failure (days) under constant immersion conditions.

Data Legend For Tables 2 and 3.

1. X@ >Y : X samples did not break after Y days.
2. X@ M±SD : X samples with mean TTF, M and standard deviation, SD.
3. Occasionally two sets of data are presented. This is done when very different TTF's are measured.

ADDED SPECIES*	INITIAL pH	STEADY STATE CREVICE pH
none	7	4
none	10	4
LiCl	10	4
Li_2CO_3	10	10
Na_2CO_3	10	10

* See footnote to Table 3.

TABLE 4 : A summary of steady-state pH values for simulated crevices in selected environments.

Compound	Solubility	Compound	Solubility
Li_2CO_3	0.21 M	Na_2CO_3	0.67 M
$LiHCO_3$	0.81 M	$NaHCO_3$	0.82 M
LiCl	15.0 M	NaCl	6.10 M

TABLE 5 : Solubilities of Several Compounds of Interest

ADDITIONAL SPECIES*	A/D**	E_{corr}	i_{pass}	E_{br}	E_{rp}	E_{corr}'
None	A	-735±13	---	-720±7	-754±14	-920±16
None	D	-892±35	0.5	-725±10	-739±6	-920±25
LiCl	A	-735±6	---	-735±6	-773±2	-880±6
LiCl	D	-850±12	0.5	-690±56	-742±25	-935±6
Li_2CO_3	A	-737±5	0.75	-600±21	-743±3	-933±10
Li_2CO_3	D	-1016±40	0.50	-603±180	-875±134	-1060±98
Na_2CO_3	A	-1210±0	56	-370±0	-990±11	-1140±42
Na_2CO_3	D	-1243±2	110	-545±21	-903±38	-1230±8

* See footnote to Table 3. All Environments are pH=10.
** A=Aerated ; D=Deaerated.

TABLE 6 : A summary of polarization data for alloy 2090C-UA in in selected environments.
(Units: Potential = mV vs SCE ; Current Dens. = $\mu A/cm^2$)

Program 4

ENVIRONMENTAL DEGRADATION OF Al-Li ALLOYS: THE EFFECT OF HYDROGEN

Semiannual Progress Report

Submitted to the
NASA Langley Research Center

by

Department of Materials Engineering
Virginia Polytechnic Institute
and State University
Blacksburg, VA 24061

Proposal N^{O}. 88-0883-01
VPI Project N^{O}. 230-11-110F-108-402306-1

Principal Investigator:
R. E. Swanson

Report Period: 7/1/88 - 12/31/88

Environmental Degradation of Al-Li Alloys.

Effect of hydrogen

Abstract

The work carried out during the report period has involved a literature review, an assessment of material and tooling requirements for the purposed tests (1), and preparation of metallographic sections in order to determine the most suitable preparation techniques.

Introduction

Strengthening in Al-Li alloys has been mainly attributed to the Al_3Li (δ') phase which nucleates as homogeneous spheres possessing an Li_2 structure (2). However, low ductility and fracture toughness of Al-Li alloys have been associated with strain localization due to both the shearable nature of the Al_3Li precipitates and the formation of precipitate-free zones (PFZ) (2,3). These problems can be overcome by alloy additions that co-precipitate along with the Al_3Li phase and help disperse slip and eliminate PFZ's. In alloy 2090, one of the alloys studied in the present work, these additives are Cu and Mg. Alloys containing more than 1.5 % Li can be expected to form a homogeneous distribution of Al_3Li and various amounts of other phases. These may include the phases occurring in binary aluminum-copper alloys, namely, G.P. zones, θ'', θ', Al_2Cu, and those occurring in the tertiary Al-Li-Cu and Al-Cu-Mg alloys, namely, Al_2CuLi (T_1), Al_6CuLi_3 (T_2), AlCuMg(S') and S. Furthermore, various transition or metastable phases T_1, S' and θ' may be present.

While work on the solution heat treatment of 2090 has shown that yield strength increased with temperature up to 543°C (1010°F), the toughness was found to level out at approximately 516°C (960°F) (4). It was concluded that 543°C was a good solution heat treatment temperature. Other workers have found that with regard to the toughness of alloy 2090, no advantage is offered by using tempers past peak age (5).

Other studies have also revealed that a deformation treatment prior to aging improves the strength and toughness of alloy 2090 (1,6). This effect has been correlated with a number of TEM observations. For alloy 2090 which was undeformed prior to aging for 60 hours at 175°C (347°F), large equilibrium precipitates were observed on high angle grain boundaries (6). The grain boundary precipitate had denude the adjacent regions of Li resulting in very wide PFZ's. When the alloy was subjected to a 7% elongation and then aged for 60 hours at 121°C (250°F), no PFZ's were observed and T_1 and δ' precipitates were much finer.

It is interesting to note that other workers (7), using electron microdiffraction, demonstrated that the major high angle grain boundary phases in Al-Li-Cu alloys are Al6CuLi3 (T2) and another particle of unknown composition which exhibits 5-fold symmetry. Their evidence shows that these phases (and not δ) are responsible for PFZ's in Al-Li-Cu alloys.

Preliminary metallography

Specimens of 2090 alloy, retained from the first year study, have been sectioned and metallographically prepared in the S-T, L-S and L-T orientations. These were polished successively on 1 μm, 0.3 μm and 0.05 μm γ alumina impregated selvyt cloths. The unetched sections are shown in Figure 1. Reasonable results were obtained under these polishing conditions, however samples presently being polished on napless polishing clothes impregnated with diamond paste appear to be producing superior results. Etchants which show promise include Kellers and Graff-Sargent reagents.

Hydrogen charging studies

In this study, test specimens are cathodically charged using the guidelines proposed by Dull and Raymond (8). Several experiments have been conducted to determine the best conditions to create hydrogen embrittlement without causing macroscopic surface damage. At this time, the tests have been carried out for various values of pH, regulated by the addition of HCl in a solution of dionized water containing 3.5 wt % NaCl. Initially, some potentiostatic and potentiodynamic tests have been conducted on 2090 alloys.

The potentiodynamic tests give us the value of Ecorr for the different solutions used. Then, we have been able to find a relation between the pH and the value of E_{corr}, as shown by equation (1) below.

$$E_{corr}(mV/SCE) = -540 - 77.7\ pH \qquad (1)$$

This equation can be compared with the one found by Schnuriger et al (9) to determined the pit generation function (Ep) as a function of chloride ion concentration:

$$Ep(mV/SCE) = -740 - 64\ pH \qquad (2)$$

In test conducted with pH near 7 (the solution contained no HCl), two corrosion potentials were detected. A typical curve is shown in Figure 2. This kind of phenomenon has been previously described by Moran et al (10). We hypothesize that this represents a change in the surface layer. We will further investigate this effect.

Several potentiostatic tests have been performed in order to see if pitting corrosion occurs. Figure 3 shows a typical pitted surface for a 2090 specimen charged at a pH of 1.5. Our results show us that solutions with a pH under 2.5 are too aggressive for this alloy. On the other hand, with the two equations described above, we can calculate a voltage which will provide hydrogen evolution, yet minimize the risk of pitting.

Microhardness test will also be made in order to determine the time needed to charge a sample.

Material/Tooling Requirements

The material requirements for the investigation of the effect of hydrogen on 2090, 2090 + In, and 2219 alloys has been reassessed and the minimum amount required for each alloy is illustrated in Figures 4-6.

With regard to the Charpy impact tests, tooling has been purchased for a machining Charpy specimens with a range of notch root radii. A program is being written specifically for use with a MTS machine and the three point bend fixture to facilitate fatigue precracking of Charpy specimens. The disk rupture test system is ready for biaxial load testing, pending receipt of appropriate sheet material. A power supply and several linear variable displacement transducers have been ordered for the disk rupture system.

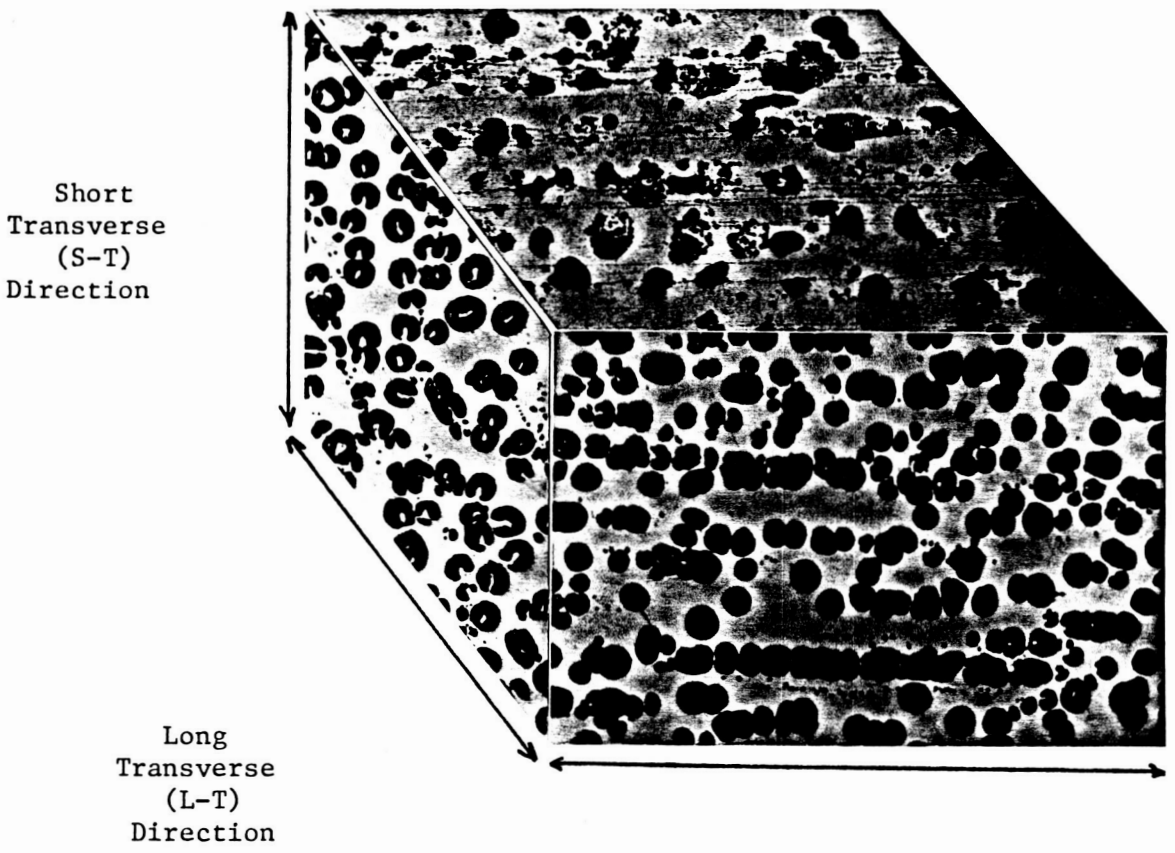

Figure 1. Triplanar optical micrograph of unetched, peak aged 2090.

ORIGINAL PAGE IS
OF POOR QUALITY

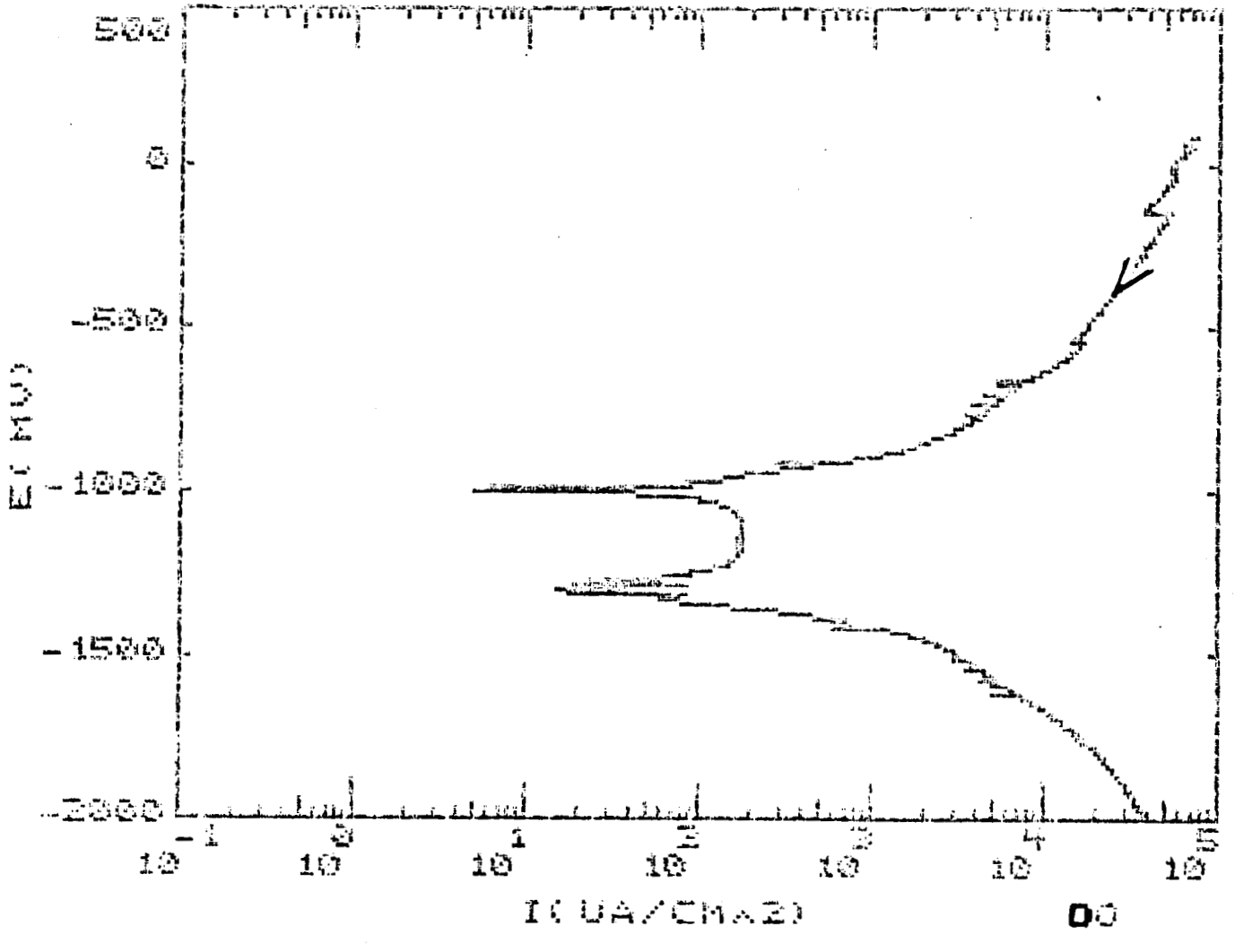

Fig 2:*Potentiodynamic curve for a 2090 alloy in a 3 NaCl - deionized water solution: Double* E_{corr}.

Fig 3: *Example of pitting corrosion of 2090 alloy after potentiostatic test in pH=1.5 at potential of -1.3 V, SCE.*

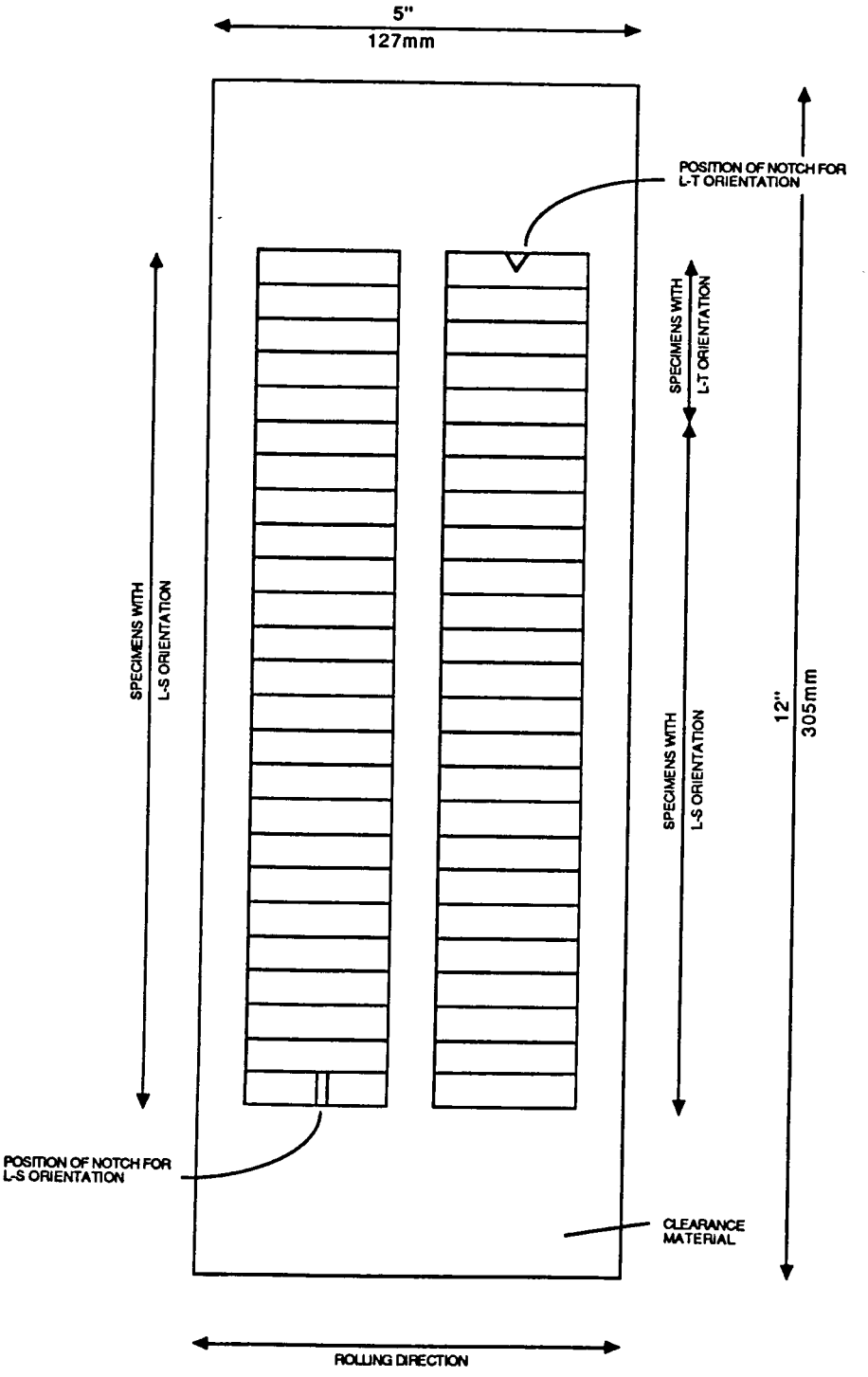

FIGURE 4. Sketch to show material requirements for charpy impact specimens. 0.5" plate * 5" * 12"

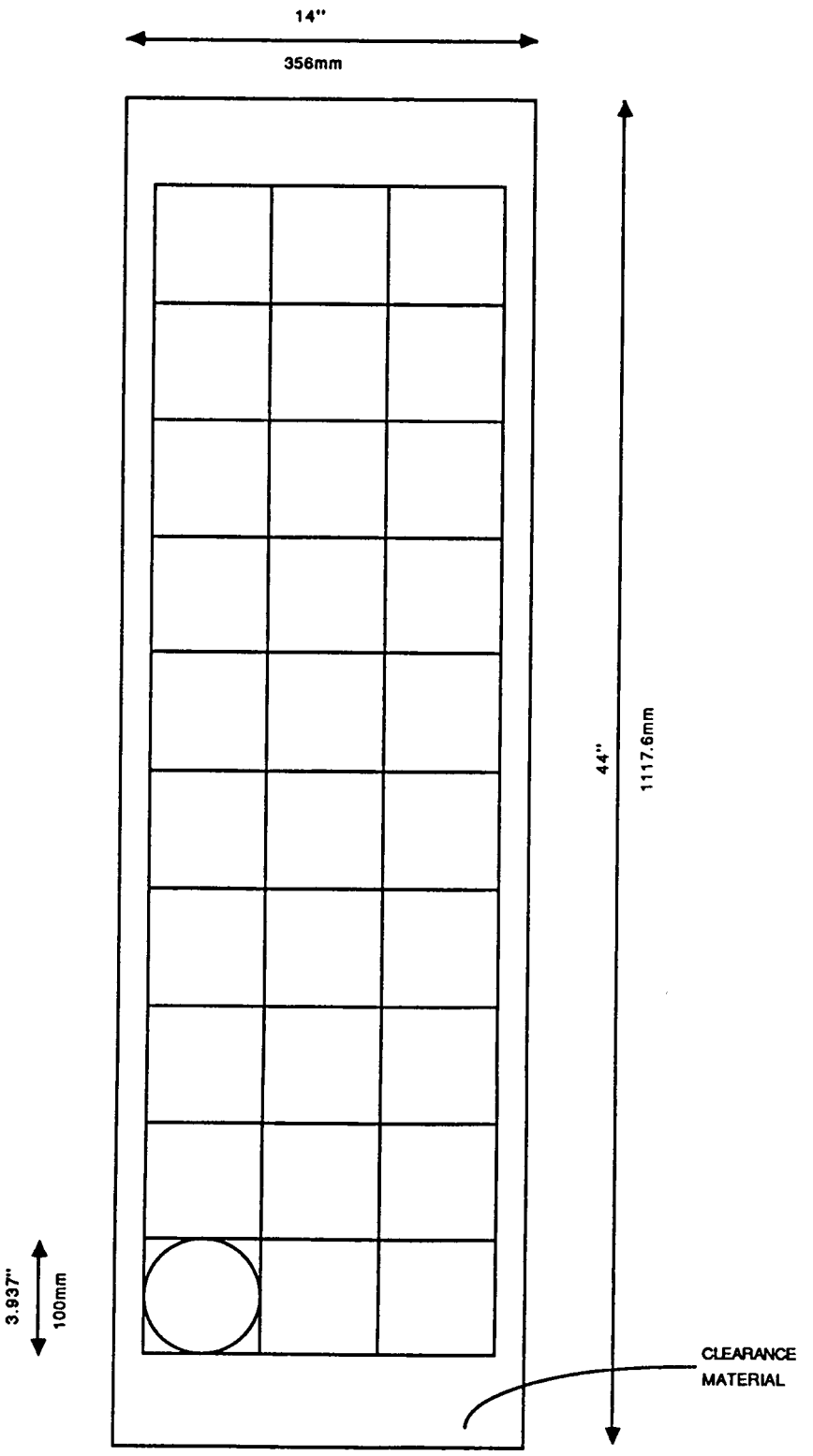

FIGURE 5. Sketch to show material requirements for disk rupture tests. 0.025" sheet * 14" * 44"

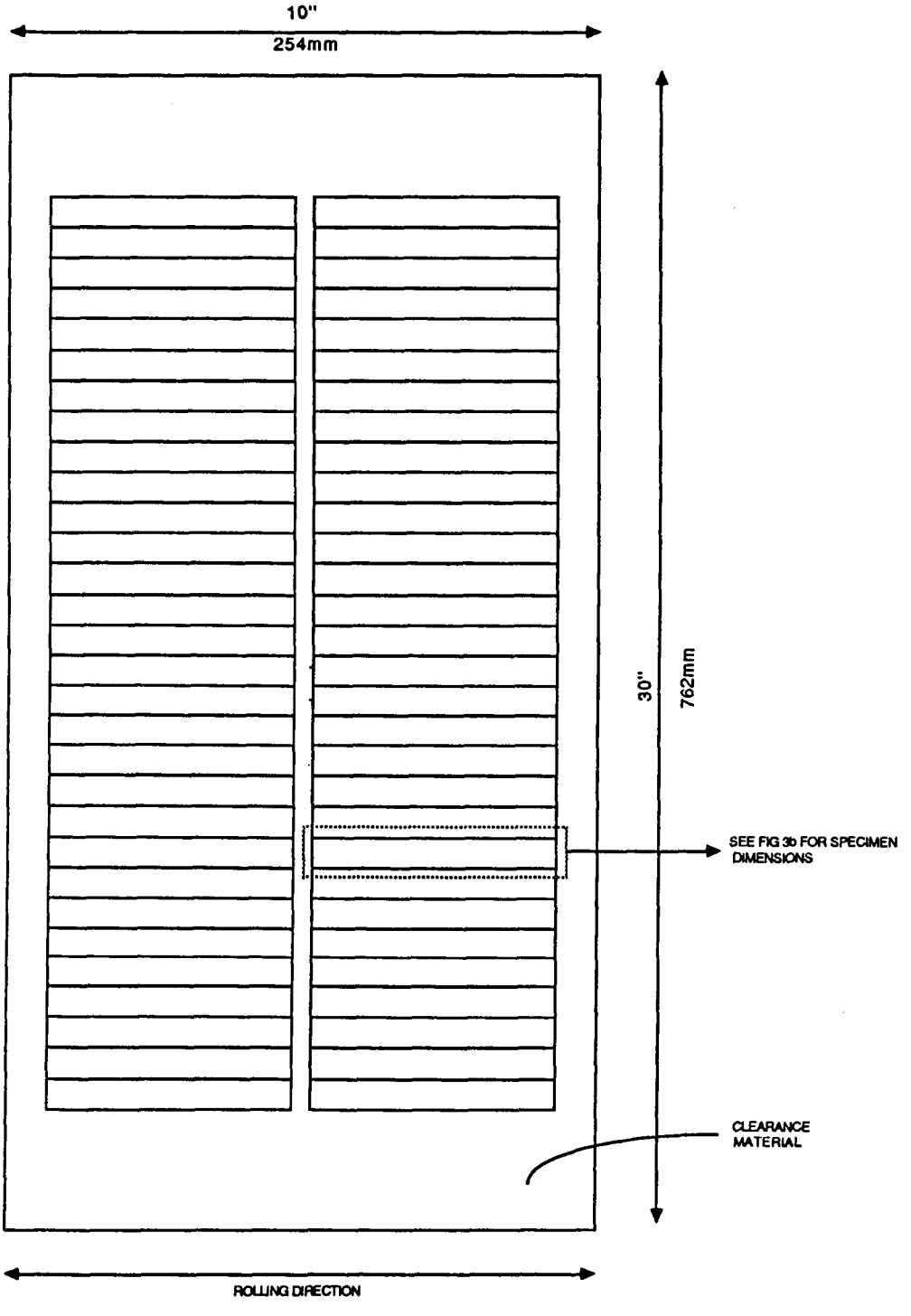

FIGURE 6a Sketch to show material requirements for two-hole flat tensile specimen. 0.25" plate * 10" * 30"

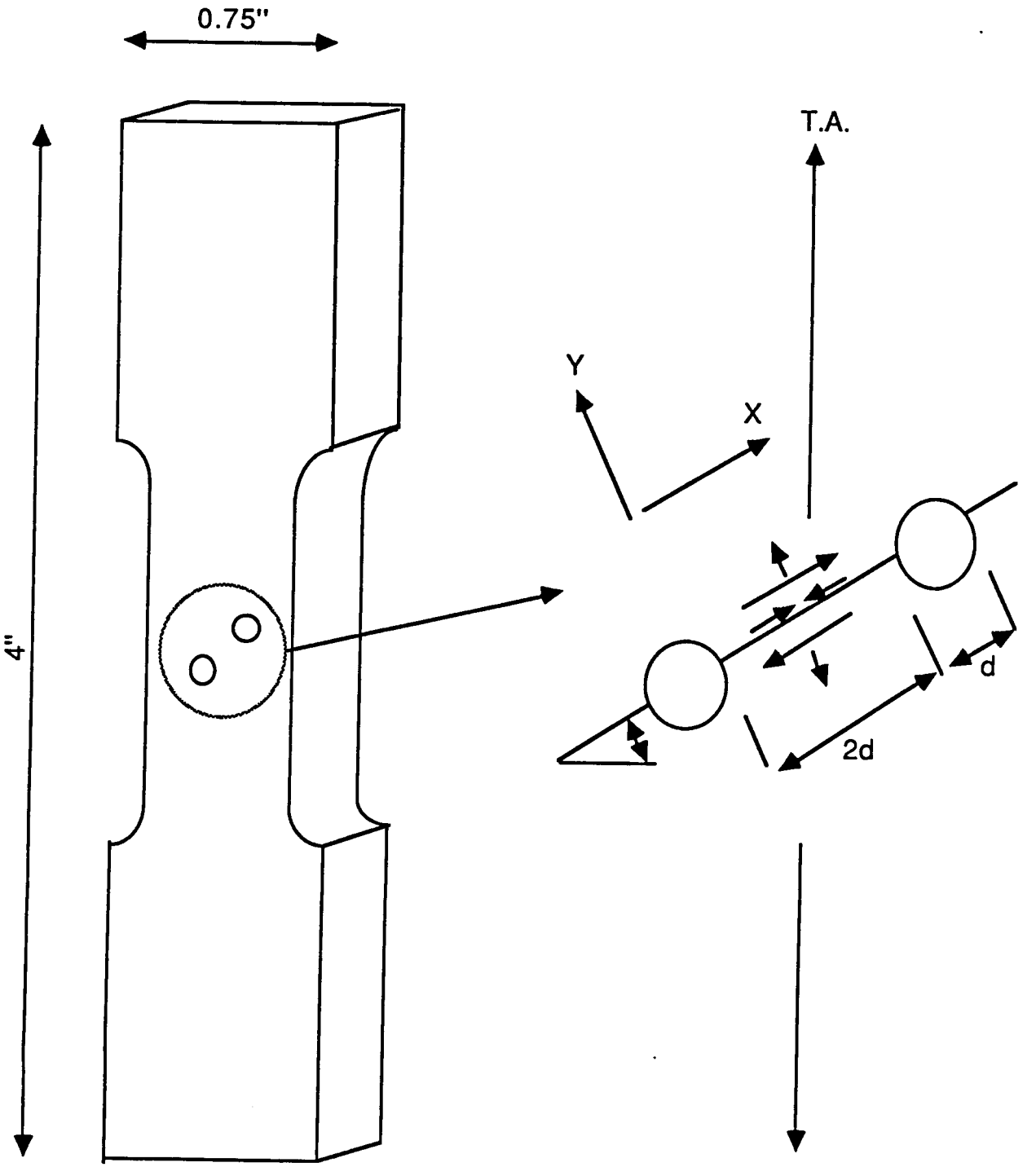

Figure 6b Schematic of two-hole flat tensile specimen

References

1. NASA Progress Report, 'Environment Assisted Degradation Mechanisms in Aluminum-Lithium Alloys', Grant No. NAG-1-745, pp. 64-83

2. P.J.E. Bischler and J.W. Martin, 'The Effect of Prestrain and of Ageing at Room Temperature on the Mechanical Properties of an Al-Li-Cu-Mg Alloy', Aluminum Alloys - Their Physical and Mechanical Properties, Vol.II, 1986, pp. 963.

3. R.F. Ashton, D.S. Thompson, and F.W. Gayle, 'The Effect of Processing on the Properties of Al-Li Alloys', Aluminum Alloys - Their Physical and Mechanical Properties, Vol. I, 1986, pp. 403.

4. F.W. Gayle, J.B. Vandersande and O.R. Singleton, 'Deformation Behaviour in the Aluminum-Lithium-Zirconium System', Aluminum Alloys - Their Physical and Mechanical Properties, Vol. II, 1986, pp. 767.

5. E.L. Calvin, S.J. Murtha, and R.K. Wyss, 'Stress Corrosion Cracking Susceptibility of Alloy 2090', Aluminum Alloys - Their Physical and Mechanical Properties, Vol. III, 1986, pp. 1853.

6. R.J. Rioja, P.E. Bretz, R.R. Sawtell, W.H. Hunt and E.A. Ludwiczak, 'Precipitation Reactions, Strength and Toughness of Al-Li-Cu Alloys', Aluminum Alloys - Their Physical and Mechanical Properties, Vol. III, 1986, pp. 1781.

7. W.A. Cassada, G.J. Shiflet and E.A. Starke, Jr., 'Characterization of Two Grain Boundary Precipitates in Al-Li-Cu Alloys with Electron Micro-Diffraction', Aluminum Alloys - Their Physical and Mechanical Properties, Vol. II, 1986, pp. 695.

8. D.L. Dull, Louis Raymond, 'Electrochemical Techniques', Hydrogen Embrittlement Testing, Louis Raymond, STP 547, ASTM, 1972, pp. 21

9. S. Schnuriger, G. Mankowski, Y. Roque, G. Chatainier and F. Dabosi, 'Statistical Study of the Pitting Corrosion of the 8090 Aluminum-Lithium Alloy', 4th International Aluminum-Lithium Conferences, G. Champier, B. Dubost, D. Miannay, L. Sabetay, Les Editions de Physique, sept 1987, pp. c3-853.

10. J.P. Moran, E.A. Starke, Jr., G.E. Stoner, G.L. Cahen, 'The Influence of the Composition and Microstructure on the Corrosion Behavior of Two AlLiX alloys', J. Corrosion, National Association of Corrosion Engineers, Vol. 43, No. 6, June 1987, pp. 374

Personnel

R.E. Swanson -Assistant Professor and Principal Investigator

M. Lewus - Post-Doctoral Research Associate

F. Rivet - Graduate Research Assistant

Program 5. DEFORMATION AND FRACTURE OF ALUMINUM LITHIUM ALLOYS FOR CRYOGENIC TANK APPLICATIONS

John A. Wagner and Richard P. Gangloff

INTRODUCTION

Cryogenic tanks are responsible for a large portion of the structural weight of current and proposed launch vehicles. As stated in the most recent progress report of this grant [1], it is envisioned that significant weight and cost savings could be realized in future launch vehicles by using advanced processing techniques and novel alloys systems. An ongoing program at NASA-LaRC is evaluating the potential of superplastic forming (SPF) a 2090 based alloy with a minor alloy addition of indium in an effort to reduce the cost of cryogenic tanks. The objective of Program 5 is to understand and optimize the fracture resistance of Al-Cu-Li and Al-Cu-Li-In alloys processed for thin sheet cryogenic tank applications.

RESULTS

Plate, 1/2x47x34", and sheet, 1/8x17x34", have been processed under various schedules at Reynolds Metals and delivered to NASA-LaRC. Compositions of these alloys are:

Al-2.65Cu-2.17Li-0.13Zr-0.05Si-0.05Fe

Al-2.60Cu-2.34Li-0.16Zr-0.04Si-0.05Fe-0.17In

The material was given a thermomechanical treatment (TMT C) or was solution heat treated and stretched approximately 3%. TMT C is a practice used to enhance the SPF behavior of sheet material and leaves the alloy in the overaged, but largely unrecrystallized condition. A representative photomicrograph is shown in Fig. 1a. Large near surface constituent particles were observed in the sheet material, but have not been identified, Fig. 1b.

The isothermal aging responses of these alloys have been defined for solution heat treatment temperatures of 538°C and 555°C at aging temperatures of 160°C and 190°C. Results of this study are summarized in Figs. 2-5. Illustrated in Fig. 2 is the hardening response at 160°C of 2090 sheet and plate from Reynolds which was stretched 3% and compared to conventional 2090 from Alcoa which was studied in the work of Huang and Ardell [2]. At an aging temperature of 160°C, the Alcoa material exhibits a more rapid aging response compared to the Reynolds material. Furthermore, for the Reynolds material, there is a significant increase in the hardenability of plate

compared to sheet material. This behavior is not currently understood.

Fig. 3 shows the effect of the addition of a minor amount of indium to the 2090 composition. Plotted is the aging response of 1/8" baseline material which was aged to the T6 (unstretched) or T8 (stretched) condition along with the aging response of 2090+In in the T6 condition. There is a significant increase in the hardenability of 2090 based material in the T6 condition when alloyed with minor additions of indium. The aging kinetics of the unstretched 2090+In sheet is comparable to the baseline sheet which was stretched 3%; therefore, 2090+In is attractive for SPF application where formed parts can not be stretched. The increase in hardness from the addition of indium is consistent with a separate study [3] at NASA-LaRC in which material was obtained from smaller 30 lb. book mold castings.

The aging response of the same group of alloys at 190°C is shown in Fig. 4 where the beneficial effect of the indium addition is again apparent. A comparison of the aging kinetics of 2090+In sheet material at 160°C and 190°C is made in Fig. 5. As expected, the aging response is more rapid at 190°C. It is interesting to note that the indium bearing alloys, and in fact all of the Reynolds alloys exhibit sluggish aging kinetics; reductions in hardness associated with precipitate coarsening are not generally observed in Figs. 2 to 5.

From this aging study, DSC results and a review of the literature, solution heat treatment at 555°C along with an aging temperature of 160°C was used in screening the mechanical properties of 2090 and 2090+In alloys. It has been demonstrated that aging at a temperature of 190°C can lead to copious grain boundary precipitation and has deleterious effects on the fracture behavior of Al-Li alloys. Strength and toughness were determined for an aging temperature of 160°C at three different aging times: 20 hrs. - underaged, 75 hrs. - peak aged and 120 hrs. - overaged.

Kahn Tear specimens, 1/8" thick, were machined with a notch root diameter of 0.001 inches from sheet material in the LT orientation to obtain a relative ranking of the toughness of these materials and precipitation hardening conditions. Tear strength of the specimens were calculated from the expression:

$$\text{Tear strength, } TS = P/A + MC/I = P/bt + 3P/bt = 4P/bt$$

b = ligament
t = thickness
P = maximum load
A = net section
M = bending moment

C = length for moment action
I = moment of inertia

Tensile specimens, 1/8" square, were machined in the longitudinal direction, and were instrumented with extensometers and strain gages. Current cryogenic tank material, 2219-T87, was also tested for a baseline. All specimens were tested in duplicate at room temperature and -190°C. Both Kahn Tear and tensile tests are currently in progress and partial results are listed in Table 1.

As suggested by the hardness data, there is an increase in the room temperature yield strength and ultimate tensile strength for 2090+In compared to baseline 2090 in the peak aged and overaged conditions, Fig. 6. It is interesting to note that the yield strength differences in Fig. 6 are small and that stretching of 2090 produces yields strengths at least as high as 60.4 ksi. These preliminary data suggest that stretching has a larger effect compared to the In addition; further work is in progress to assess the effects of indium and mechanical deformation on tensile yield and work hardening properties of the 2090 composition.

Considering room temperature ductilities, Table 1, similar tear strengths are observed for T6 2090 and 2090+In. Stretched 2090 appears to exhibit a higher toughness than either undeformed condition.

Examination of Table 1 reveals that there was no significant increase in the tear strength of 2090+In and 2090 based alloys in either the T6 or T8 conditions when testing at cryogenic temperatures. Furthermore, there is a significant reduction of the cryogenic tear strength of the 2090+In alloy for an aging time of 75 hours. These results are in contrast to the results of Glazer et al. [4], who observed a significant increase in toughness of 2909-T8E41 compact tension specimens when tested at cryogenic temperatures. From Table 1, note that 1/8" thick 2219-T87 specimens machined from 1/4" plate exhibit an increase in toughness at cryogenic temperatures and the best overall toughness of the materials screened by Kahn Tear tests.

This lack of toughening at cryogenic temperatures for the sheet material could be related to a change in stress state from primarily plane strain in the compact tension specimens to plane stress in the thin sheet Kahn Tear specimens and the related effect on delamination toughening. While the Kahn tear specimens were notched rather than precracked, the very sharp notch root radius should approximate the later and have only a small effect on increasing fracture toughness. Only tear strength has been computed to date.

It should be emphasized that Kahn Tear testing is only a screening process and has been employed here to develop a relative toughness ranking of these alloys at room and cryogenic temperatures. Before firm conclusions can be established, so-called Kahn initiation and propagation energies must be calculated to, and the effect of temperature considered. This work is in progress. Additionally, refined fracture mechanics methods, with high resolution crack growth monitoring, must be employed to reasonably measure fracture toughness.

CONCLUSIONS

Results for this reporting period can be summarized as follows:

-The 2090 base material produced by Reynolds Metals exhibits a more sluggish aging response compared to Alcoa 2090.

-For the material produced by Reynolds, the 1/2" plate has increased hardenability compared to the 1/8" sheet. The microstructural origin of this effect is not clear.

-Addition of indium to 2090 increases hardness for a range of aging times at two temperatures. Room temperature yield strength and ultimate tensile strength are increased by indium, however, the effect is not substantial.

-The room temperature fracture toughness of stretched alloy 2090 appears to be higher than that of unstretched 2090 or 2090+In.

-There is no significant increase in toughness, as measured by Kahn tear strength, for 2090 based materials at cryogenic temperatures. 2090+In exhibits a decrease in tear strength in the peak aged condition at cryogenic temperatures.

FUTURE PLANS

Future plans will focus on Task II and on Task III as shown in the flow chart in Fig. 7. Specifically, the following areas will be addressed:

-Complete initial alloy strength and Kahn tear fracture toughness characterization.

-Identify most promising techniques for measuring the cryogenic fracture toughness of thin sheet material.

-Conduct microstructural characterizations of 2090 and 2090+In using optical and transmission microscopy.

-Evaluate the combined effects of SPF strain and cryogenic temperatures on the deformation and fracture of 2090 based alloys.

REFERENCES

1. Progress Report, "Environment Assisted Degradation Mechanisms in Advanced Light Metals," Grant No. NAG-1-745-2, Report No. UVA/528266/MS88/102, June, 1988.

2. J.C. Huang and A.J. Ardell: "Microstructural Evolution in Two Al-Li-Cu Alloys," Aluminum-Lithium III, eds., C. Baker et al., p. 455, 1985.

3. L. Blackburn, W. Cassada, G. Colvin and E.A. Starke, Jr., "The Effect of Processing on the Microstructure, Strength and Fracture Behavior of Aluminum-Lithium Alloys," Aluminum-Lithium Symposium, Los Angeles Chapter of ASM, Los Angeles, CA, March, 1987.

4. J. Glazer, S.L. Verzasconi, E.N.C. Dalder, W. Yu, R.A. Emigh, R.O. Ritchie and J.W. Morris, Jr., "Cryogenic Properties of Al-Cu-Li-Zr Alloy 2090," Advances in Cryogenic Engineering Materials, 1986.

Alloy	Condition	Aging Time (hrs.)	Temp. (C)	TS (ksi)	YS (ksi)	UTS (ksi)
2090	T8	20	25	66.2	59.1	67.4
	T8	20	25	68.1	60.4	68.7
	T8	20	-190	63.3		
	T8	20	-190	63.0		
2090	T6	20	25	71.9	48.1	62.6
	T6	20	25	73.0	46.9	61.7
	T6	20	-190	75.9		
	T6	20	-190	74.6		
	T6	75	25	60.4	52.1	65.4
	T6	75	25	55.4	53.7	66.8
	T6	75	-190	56.5		
	T6	75	-190	57.9		
	T6	120	25	55.3	53.8	69.9
	T6	120	25	58.4	53.4	66.7
	T6	120	-190	54.5		
	T6	120	-190	49.8		
2090 + In	T6	20	25	70.6	44.3	59.8
	T6	20	25	69.6	48.6	63.6
	T6	20	-190	67.4		
	T6	20	-190	64.8		
	T6	75	25	57.0	55.0	73.1
	T6	75	25	56.7	52.3	70.8
	T6	75	-190	47.3		
	T6	75	-190	52.5		
	T6	120	25	46.0	55.6	72.3
	T6	120	25	42.6	56.9	74.5
	T6	120	-190	39.3		
	T6	120	-190	48.4		
2219	T87		25	69.5	55.4	69.1
	T87		25	70.0	55.1	68.3
	T87		-190	81.1		
	T87		-190	82.0		

Table 1. Kahn Tear and Tensile Data at Room and Cryogenic Temperatures

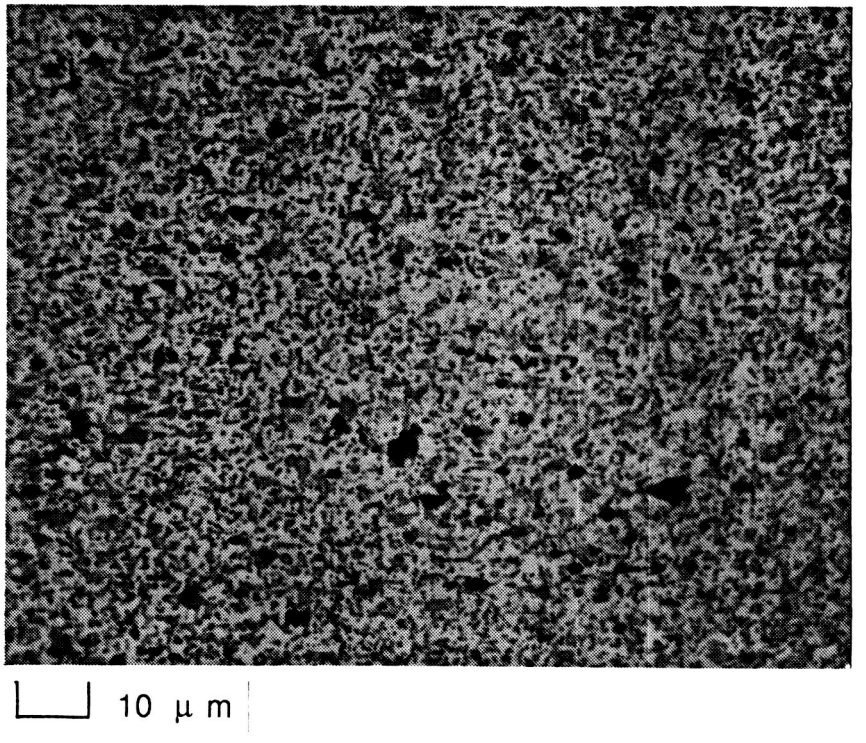

Fig. 1a. Photomicrograph of 2090 + In, TMTC

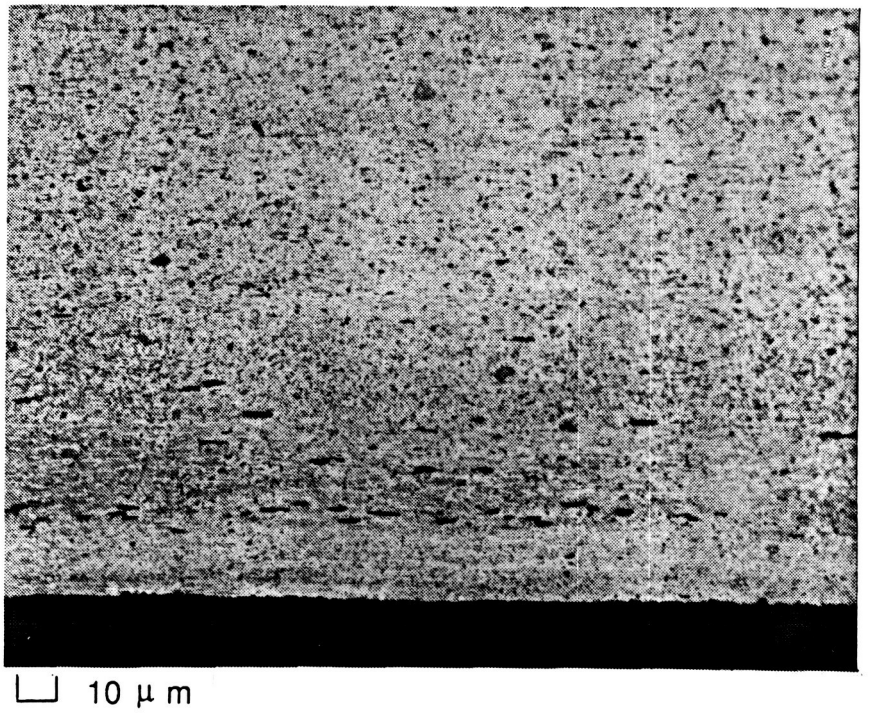

Fig. 1b. Photomicrograph of 2090 + In showing near surface constituent particles

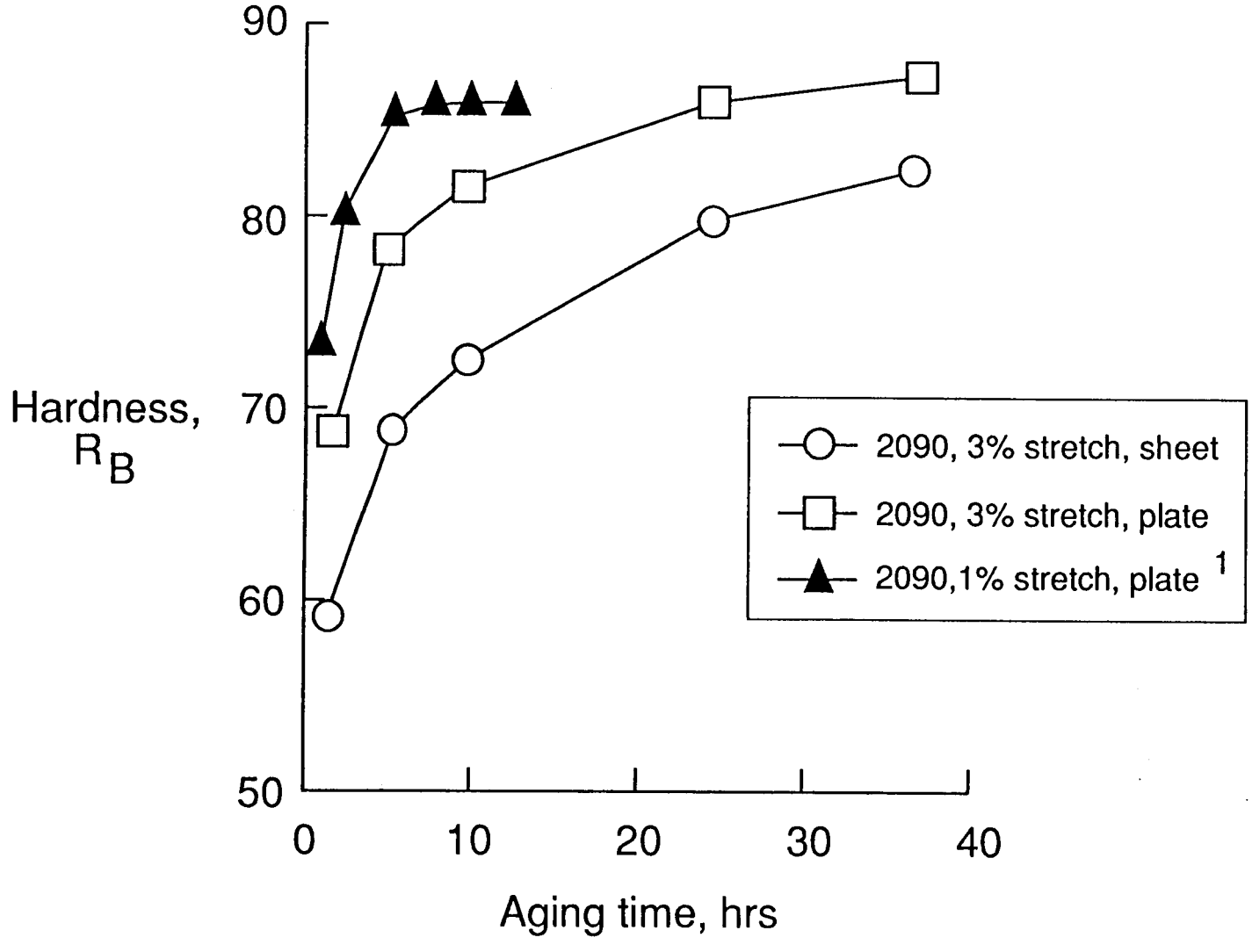

Fig. 2 Hardness, R_B, as a function of aging time for 2090 based alloys aged at 160°C

[1] J.C. Huang and A.J. Ardell: "Microstructural Evolution in Two Al-Li-Cu Alloys", Aluminum-Lithium III, eds. C. Baker et al, pg 455, 1985.

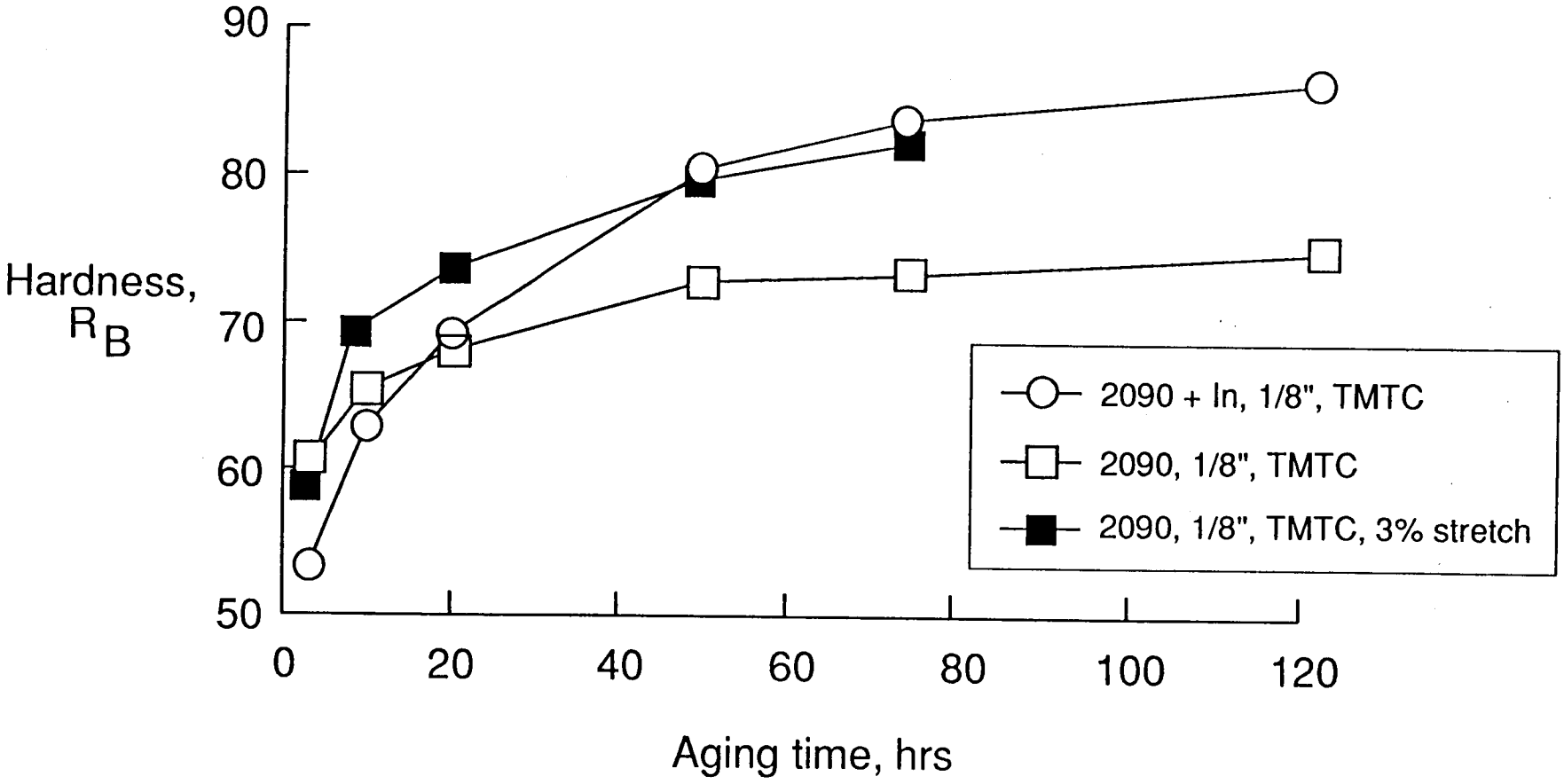

Fig. 3 Hardness, R_B, as a function of aging time for 2090 and 2090 + In solution heat treated at 555°C and aged at 160°C

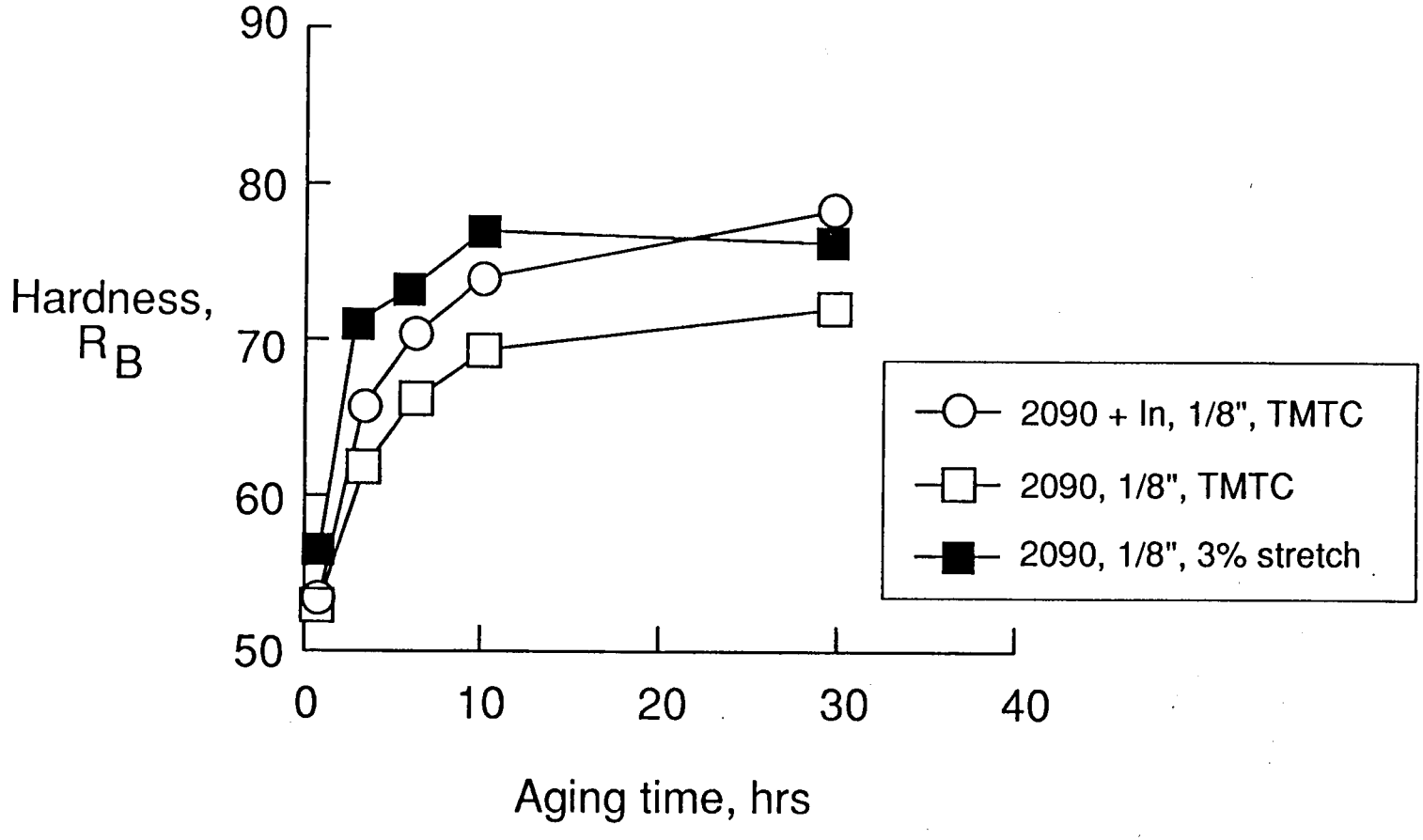

Fig. 4 Hardness, R_B, as a function of aging time for 2090 and 2090 + In solution heat treated at 555°C and aged at 190°C

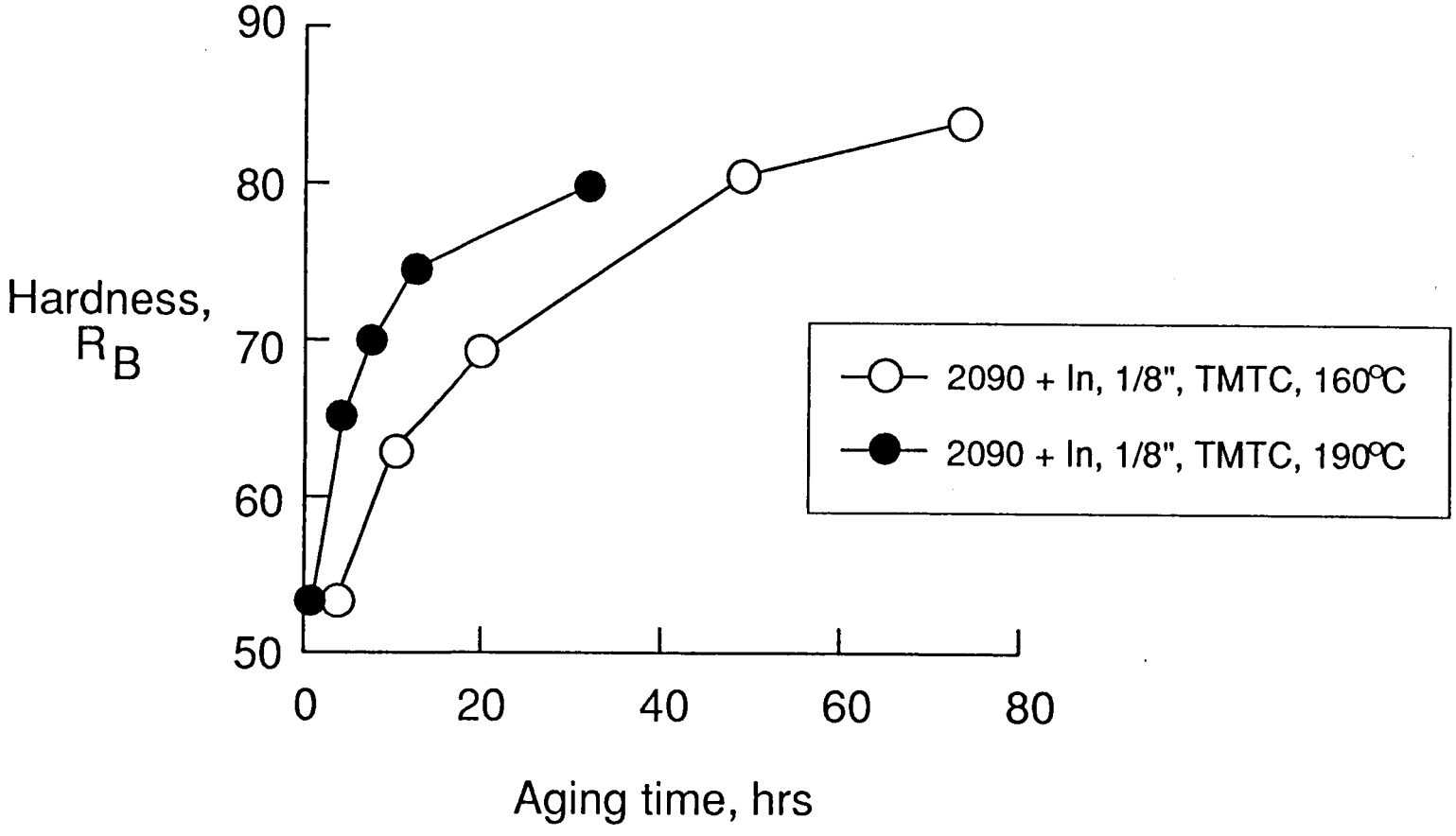

Fig. 5 Hardness, R_B, as a function of aging time for 2090 + In aged at 160°C and 190°C

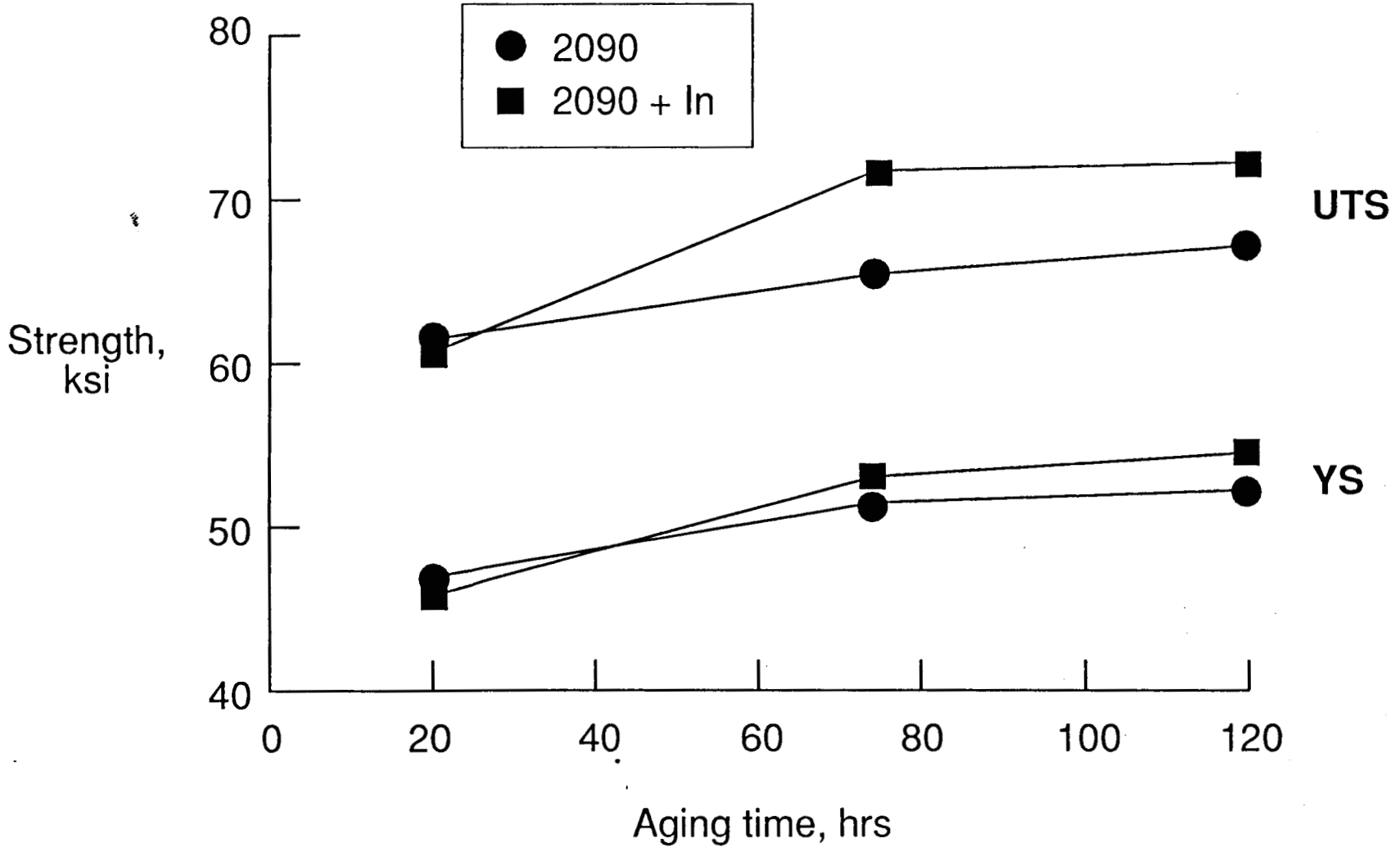

Fig. 6 Variation of room temperature strength with aging time at 160°C for 2090 and 2090 + In, 0% stretch

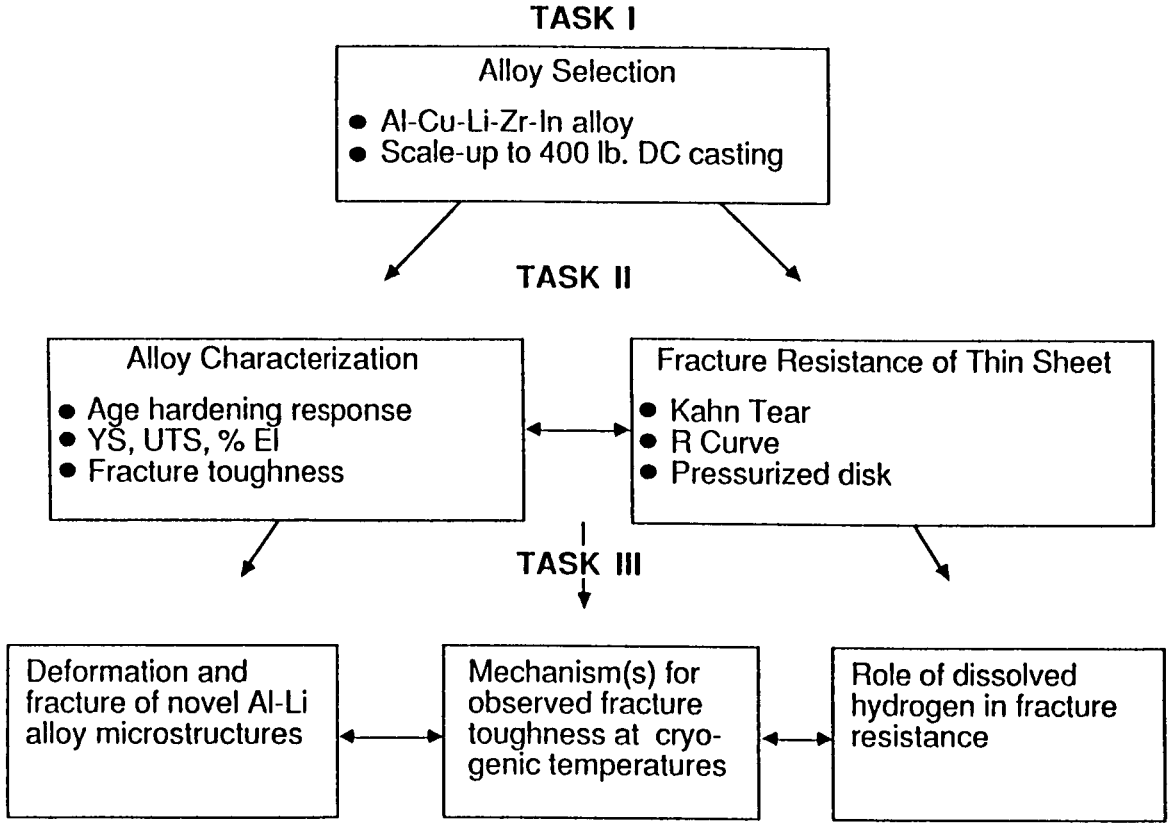

Fig. 7. Task identification for deformation and fracture of advanced aluminum alloys.

Program 6 ELEVATED TEMPERATURE CRACK GROWTH IN ADVANCED POWDER METALLURGY ALUMINUM ALLOYS

William C. Porr, Jr. and Richard P. Gangloff

Background

Aluminum alloys that offer retained strength at elevated temperatures could represent large savings in aerospace applications because of their low density and lower potential cost. Previously, the precipitation strengthened IM alloys 2219 and 2618 were considered the best aluminum alloys for elevated temperature applications. These alloys show significant mechanical property deterioration above 200° C due to large scale precipitate coarsening, time dependent plastic deformation, environmental reaction and cracking.

Newer, rapidly solidified powder metallurgy aluminum alloys show improved mechanical property retention with increasing temperature (Figure 1). Rapid solidification techniques suppress equilibrium cooling reactions and produce powders with ultra fine microstructures. By alloying with elements that have high liquid solubility, low solid solubility, and low diffusion coefficient in aluminum, a high volume fraction of fine intermetallic dispersoids that remain stable at high temperatures can be produced. Allied-Signal Inc. is marketing two RSPM Al-Fe-V-Si alloys that appear especially promising. They report coarsening rates of the $Al_{12}(Fe,V)_3Si$ intermetallic dispersoid in these alloys that are three to four orders of magnitude less at 425° C than the rates for intermetallics in other aluminum PM alloy systems. The Light Metals Center at UVA has reported microstructural stability of one of these alloys annealed at 500° C for times of up to 100 hours [1]. This identifies the Al-Fe-V-Si system as promising for many elevated temperature applications.

Objective

The goal of this research program is to evaluate subcritical crack growth at elevated temperatures in an Al-Fe-V-Si powder metallurgy alloy. As an extension of this goal, the effect of microstructure or environment on crack growth and mechanisms will also be examined.

Proposed Research

Three materials will be used in this study: the Al-Fe-V-Si alloys that are the focus of the program goal, and aluminum alloys 2618 and 2219 which are elevated temperature

precipitation strengthened IM alloys for which a database of elevated temperature crack growth rate information exists. This research will be conducted in five parts, with each stage providing the direction for the next (Figure 3). All materials will be characterized for microstructural homogeneity and room temperature tensile strength and ductility.

Stage 1 of the program will involve R-curve determination as a function of temperature for the three alloy systems to identify fracture behavior and temperature ranges of interest. Loading rate will be varied to determine the extent to which the materials behave in time-independent brittle and in creep brittle manners. Testing will be conducted according to a significant modification to ASTM Standard E 561, and which employs electrical potential monitoring of crack initiation and growth coupled with analytical solutions for K or J. If it is found that Al-Fe-V-Si alloys embrittle substantially at elevated temperatures, crack growth may be characterized by linear elastic fracture mechanics. However, this result is not expected and the J integral approach may be required.

Stage 2 of the program will be tensile and creep-rupture testing at temperatures of interest, identified in Stage 1, to determine material constants necessary for calculation of the C* and transient creep parameters. Tensile testing will be conducted according to ASTM Standards E 8 and E 21, and creep-rupture testing will be conducted according to ASTM Standard E 139. Limited microstructural evaluation may also be conducted at this time to identify any variables that may influence the following program stages.

Stage 3 will be the evaluation of crack growth using the C* and transient creep parameters in the 2618 and 2219 alloys. The goal of this stage of the project will be to refine test techniques for determining the creep parameters by comparing results to those published previously. This testing will be done according to guidelines determined by the ASTM Task Group E-24.04.08 on creep crack growth testing. Compact tension type fracture mechanics specimens will be used in all creep crack growth testing. Tests will be performed at selected temperatures to determine temperature effects on creep crack growth.

Stage 4 will duplicate Stage 3 testing using an Al-Fe-V-Si PM alloy. Crack growth rate will be measured as a function of C* and temperature. Microscopy will be done to correlate microstructural factors with changes in crack growth rate and to explain mechanisms for this crack growth.

Stage 5 will involve creep crack growth testing at one temperature while varying either the volume fraction of intermetallic dispersoids or the gaseous environment.

Experimental results and mechanistic analyses from either of these tests would provide valuable information for materials selection.

Completion of this five stage research program should sufficiently evaluate the elevated temperature crack growth behavior in an Al-Fe-V-Si PM alloy.

Research Progress

Research during this reporting period has focused on a literature review of fracture mechanics analyses of time dependent crack tip deformation and subcritical propagation, on materials acquisition, and on equipment development.

Fracture Mechanics Characterization of Elevated Temperature Cracking: Review of Established Analyses

Characterization of the mechanical properties of the RSPM aluminum alloys has been limited in the most part to tensile testing at various temperatures. In some cases, creep rupture data are available, as is fracture toughness data at room temperature. However, creep-rupture data may not be adequate to evaluate materials performance since it has been shown that "constant-load elevated-temperature creep with strains less than 1% caused considerable reduction in fracture toughness" in aluminum 2618 [2]. For engineering applications, fracture mechanics studies at elevated temperatures would be desired to characterize the effect of defects which are inherent to powder metallurgy products.

Beyond fracture toughness, it is necessary to characterize constant-load subcritical crack growth at elevated temperatures and to make life predictions. Any crack tip field parameter that does this must be a function of time, temperature, and reference stress. Neither the linear elastic fracture parameter, K, nor the elastic-plastic fracture parameter, J, are likely to characterize crack growth rate under steady state creep conditions because neither parameter has a time dependence.

In 1976, Landes and Begley introduced an energy rate line integral, C*, analogous to the path independent energy integral, J, which accounted for deformation and strain rates in characterizing the stress field at the tip of a crack [3]. It has subsequently been shown that C* characterizes crack growth in a metal under steady state creep conditions. Ellison and Musicco have published a compilation of C* testing results for steels and aluminum alloys [4]. Figure 2 shows their compilation for aluminum alloys.

It is important to note that C* is valid only under steady state creep conditions. Saxena and Reidel have each introduced modified C* parameters to characterize crack growth rate under transient conditions from small scale creep to steady state creep. Each has also published in-depth review papers on the theory of C* and these modified parameters (Saxena, [5]; Reidel, [6]). Saxena lists the following equations for calculating creep fracture mechanics parameters:

$$C^* = \frac{P \dot{V}_{ss}}{B W} \eta(a/W,n) \qquad (1)$$

where P is load, $\dot{V}_{ss}$ is the measured steady state load line deflection rate, B is the specimen thickness, W is the specimen width, and $\eta(a/W,n)$ is a geometry factor that depends on crack size and the material creep exponent, n. Saxena also lists an alternative method for calculating C* by making use of the analogy to the fully-plastic J solutions.

$$C^* = a A h_1(a/W,n) (\sigma_e)^{n+1} \qquad (2)$$

where σ_e is the applied remote effective stress, a is the crack length, $h_1(a/w,n)$ is a geometry calibration function found in the EPRI handbook, and A is a material creep constant. Note that with equation 2, it is not necessary to know the steady state load line displacement rate to calculate C*.

The transient creep parameters are not as easily determined, however, useful interpolation functions have been defined for estimation. Reidel proposes a parameter C(t) which characterizes the amplitude of the stress field at a crack tip in a material from small scale creep to steady state creep. The problem with this parameter is that it cannot be measured. Reidel proposes that it can be estimated by:

$$C(t) = (t_T/t + 1)C^* \qquad (3)$$

where t is the time, and t_T is the steady state transition time given by:

$$t_T = \frac{(1-\nu^2)K_I^2}{(n+1)EC^*} \qquad (4)$$

where K_I is the stress intensity factor, ν is Poisson's ratio, and E is the modulus of elasticity.

Saxena proposes the parameter C_t to characterize crack growth driving force. The disadvantage with C_t is that it does not describe the amplitude of the crack tip stress field. It is, however, based on stress-power dissipation rate with a growing crack and has been found to accurately characterize crack growth rate in creeping materials. C_t is given by:

$$C_t = \frac{P \dot{V}_c}{B W} \frac{F'}{F} + C^* \left(\frac{F'/F}{\eta} - 1 \right) \qquad (5)$$

where $\dot{V}_c$ is the load line displacement rate due to the growing creep zone at the tip of a crack, F' and F are geometry terms, and all other terms are as previously defined. A more sophisticated equation by Saxena accounts for primary creep as well.

Based on the above information, any future elevated temperature characterization of mechanical properties of RSPM aluminum alloys should include fracture mechanics studies, preferably a C* analysis.

Materials Acquisition and Properties

Acquisition of 2219 and 2618 alloys for the first three stages of this research program is complete. The 2219 alloy was supplied by NASA LaRC in plate form (1.0" and .25" thicknesses) with a T87 temper. The 2618 alloy is also in plate form (2.25" and .57" thicknesses) with a T651 temper. This alloy was supplied with chemical analysis and mechanical properties documentation by Dr. Daniel Ferton of Cegedur Pechiney. That information is as follows:

.57" plate

Chemical composition (wt%): Al, 2.57 Cu, 1.63 Mg, 1.09 Fe, 0.23 Si, 1.18 Ni

Tensile properties (LT Direction): YS: 62 ksi
UTS: 66 ksi
RA: 7%

2.25" plate

Chemical composition (wt%): Al, 2.66 Cu, 1.62 Mg, 1.13 Fe, 0.22 Si, 1.17 Ni

Tensile properties (LT Direction): YS: 63 ksi
UTS: 69 ksi
%E: 7.3

Acquisition of the desired PM alloys will fulfill the materials requirements for this research program. NASA-LaRC is assisting with this effort.

Plans for the Coming Report Period

The elevated temperature test system being assembled at UVA, described in the previous progress report [7], will become fully operational with the delivery of elevated temperature test fixtures in early 1989. At that time, Stages 1 through 4 of this research program will be possible. Completion of the ultrahigh vacuum chamber for use with the test system in Stage 5 of the program will occur at some time in the future.

Preliminary material characterization will be performed on the program alloys. This will involve optical microscopy and simple tension testing to evaluate the nature and quality of the microstructures of the materials.

Test results of Stage 1 should be available at the end of the next reporting period. After initial refining of test techniques, generation of the crack growth resistance data as a function of loading rate and temperature will begin.

References

1. R.E. Franck and J.A. Hawk, "Effect of Very High Temperatures on the Mechanical Properties of Al-Fe-V-Si Alloy", Light Metals Center, Department of Materials Science, University of Virginia, report to Wright Aeronautical Laboratories, Wright-Patterson Air Force Base, Ohio, July, 1988.

2. D. Bobrow, A. Arbel, and D. Eliezer, "The Effect of Constant-Load Creep on Fracture Toughness and Tensile Behavior of Precipitation-Free Zone Aluminum Alloy Type 2618", Scripta Met., 22, pp. 1503-1508, 1988.

3. J.D. Landes and J.A. Begley, "A Fracture Mechanics Approach to Creep Crack Growth", Mechanics of Crack Growth, ASTM STP 590, American Society for Testing and Materials, Philadelphia, PA, pp. 128-148, 1976.

4. E.G. Ellison and G.G. Musicco, "Notch-Rupture and Crack-Growth Behavior Under Creep Conditions", Subcritical Crack Growth Due to Fatigue, Stress Corrosion and Creep, Elsiver Applied Science Publishers, L.H. Larsen ed., New York, pp. 403-448, 1984.

5. A. Saxena, "Mechanics and Mechanisms of Creep Crack Growth", to be published in proceedings of the 1987 ASM Materials Science Seminar Fracture Mechanics: Microstructure and Micromechanisms, ASM, Metals Park, Ohio, 1987.

6. H. Riedel, Fracture at High Temperatures, Springer-Verlag Berlin, Heidelberg, Germany, 1987.

7. R.P. Gangloff, G.E. Stoner, and R.E. Swanson, "Environment Assisted Degradation Mechanisms in Advanced Light Metals", University of Virginia, Report No. UVA/528266/MS88/102, June, 1988.

8. Metals Handbook Desk Edition, American Society for Metals, Metals Park, Ohio, 1985.

9. T.E. Tietz and I.G. Palmer, "Advanced P/M Aluminum Alloys", Advances in Powder Technology, G.Y. Chin ed., American Society for Metals, Metals Park, Ohio, 1982.

10. Allied-Signal promotional information, author unknown.

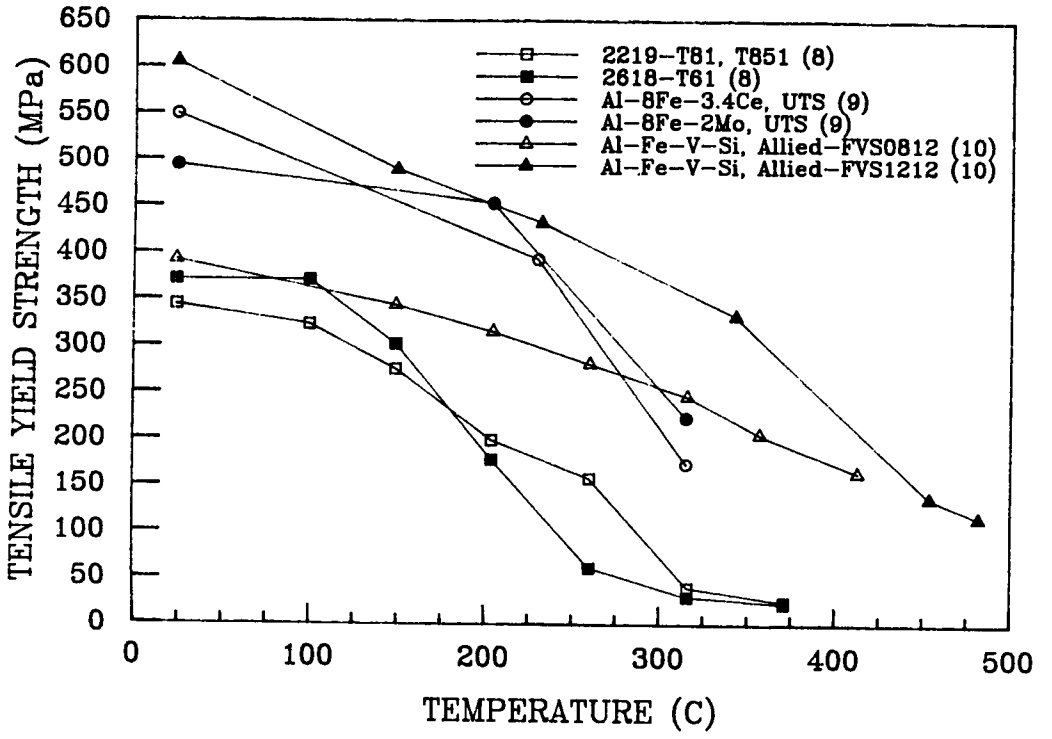

Figure 1. Tensile data of selected IM and PM aluminum alloys.

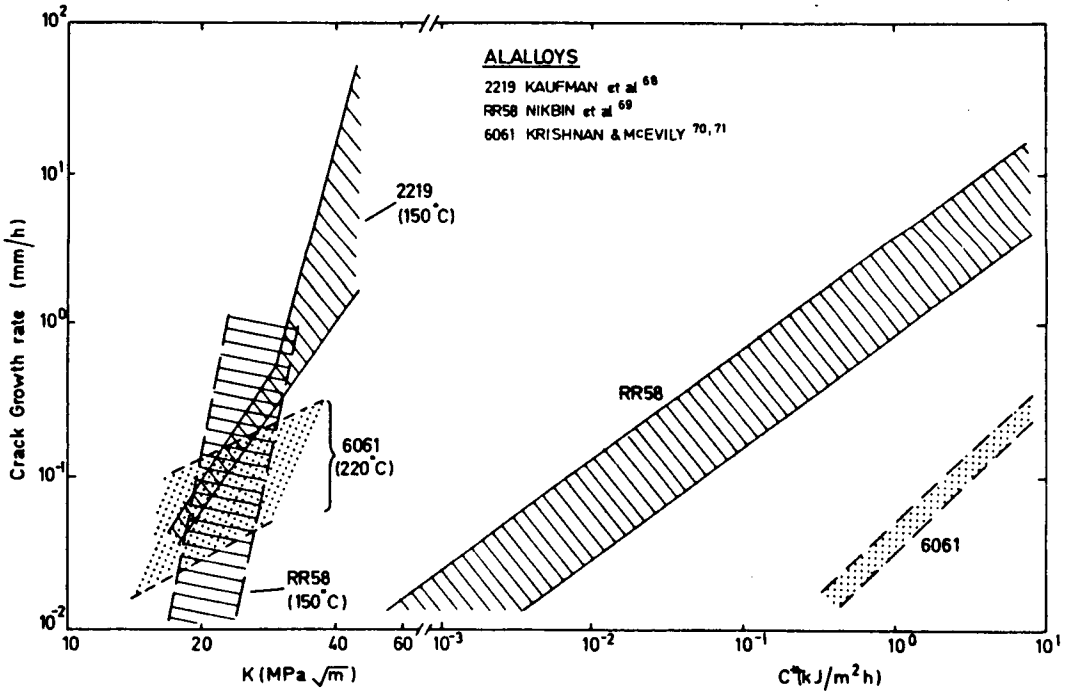

Figure 2. Creep crack growth rates in aluminum alloys in terms of K and C* parameters. Alloy designation RR58 is equivalent to 2618.(4)

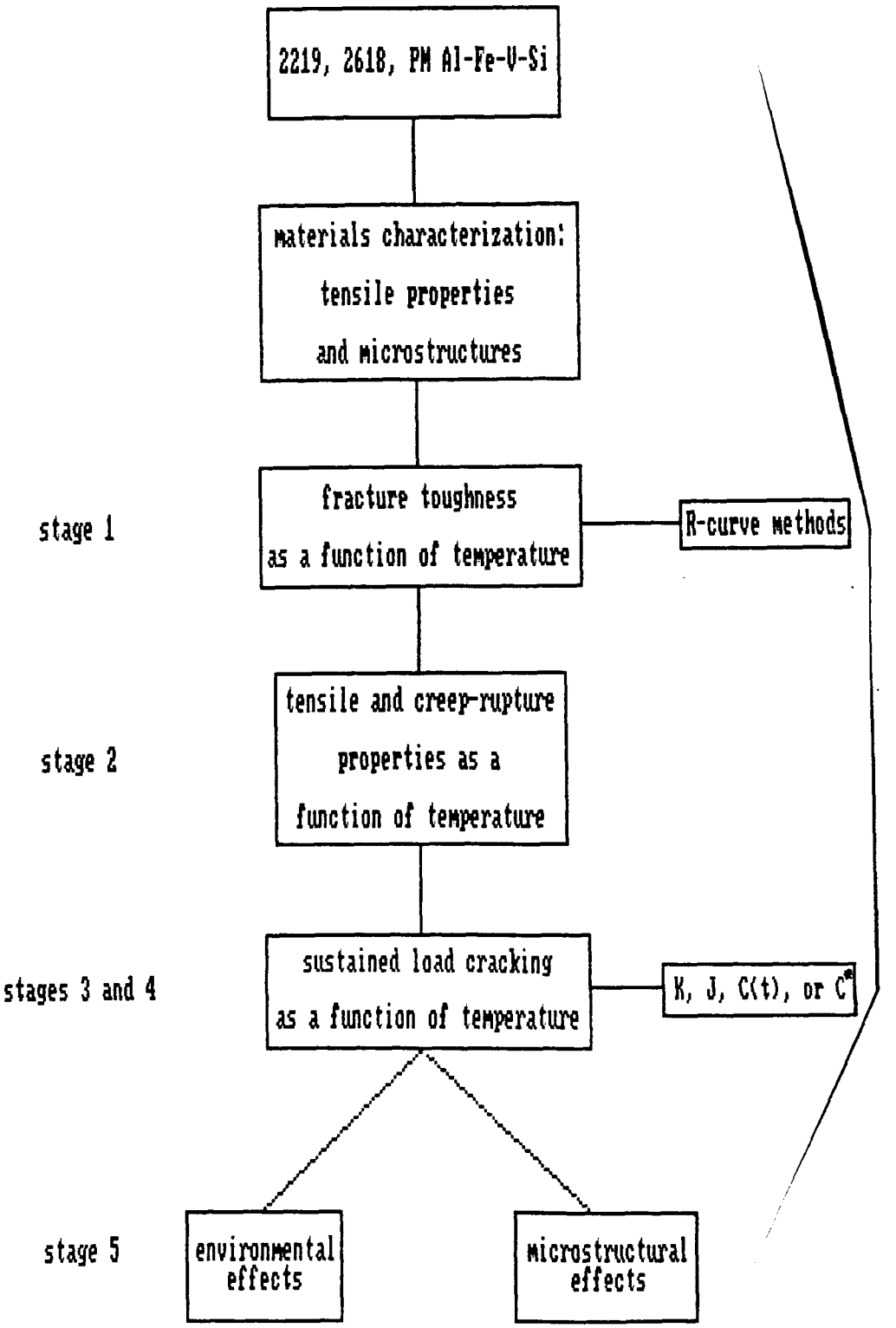

Figure 3. Flow chart of proposed research program.

APPENDIX I: GRANT PUBLICATIONS

R.S. Piascik and R.P. Gangloff, "Aqueous Environment Effects on Intrinsic Corrosion Fatigue Crack Propagation in an Al-Li-Cu Alloy", Environmental Cracking of Metals, R.P. Gangloff and M.B. Ives, eds., NACE, Houston, TX, in press, 1989.

R.S. Piascik and R.P. Gangloff, "Intrinsic Fatigue Crack Propagation in Aluminum-Lithium Alloys: The Effect of Gaseous Environments", in Proc. 7th International Conference on Fracture, K. Salema, ed., Plenum Press, London, in press, 1989.

R.G. Buchheit, Jr. and G.E. Stoner, "The Hydrolytic Effects of Al(III) and Li(I) in Simulated Crevice Experiments Using 2090, 2024 and 1100 Aluminum", to be submitted, Corrosion, 1989.

R.G. Buchheit, Jr., J.P. Moran, G.E. Stoner and K.A. Coyne, "An Investigation of the Localized Corrosion Behavior of Alloy 2090", to be submitted, Corrosion, 1989.

Proceedings ICF-7, K. Salema, ed., Pergammon Press, London, in Press.

INTRINSIC FATIGUE CRACK PROPAGATION IN ALUMINUM-LITHIUM ALLOYS: THE EFFECT OF GASEOUS ENVIRONMENTS

ROBERT S. PIASCIK AND RICHARD P. GANGLOFF

Department of Materials Science
University of Virginia
Charlottesville, VA 22901

ABSTRACT

Gaseous environmental effects on intrinsic fatigue crack growth are significant for the Al-Li-Cu alloy 2090, peak aged. For both moderate ΔK-low R and low ΔK-high R regimes, crack growth rates decrease according to the environment order: purified water vapor, moist air, helium and oxygen. Gaseous environmental effects are pronounced near threshold and are not closure dominated. Here, embrittlement by low levels of H_2O (ppm) supports hydrogen embrittlement and suggests that molecular transport controlled cracking, established for high ΔK-low R, is modified near threshold. Localized crack tip reaction sites or high R crack opening shape may enable the strong environmental effect at low levels of ΔK. Similar crack growth in He and O_2 eliminates the contribution of surface films to fatigue damage in alloy 2090. While 2090 and 7075 exhibit similar environmental trends, the Al-Li-Cu alloy is more resistant to intrinsic corrosion fatigue crack growth.

KEYWORDS

Aluminum alloy; Al-Li; fatigue crack growth; fracture mechanics; corrosion fatigue; gaseous environment; hydrogen embrittlement; surface film; crack closure.

INTRODUCTION

The objective of this research is to characterize and understand intrinsic fatigue crack propagation in advanced aluminum - lithium based alloys, with emphasis on the damage mechanisms for environmentally assisted transgranular cracking.

Al-Li alloys such as 2090 and 8090 exhibit outstanding fatigue crack propagation resistance, but attributable to the extrinsic effects of crack surface closure contact and crack tip deflection (Venkateswara Rao et al., 1988). Extrinsic crack growth resistance is likely to be geometry, orientation and loading history dependent; thus complicating mechanistic understanding and defect tolerant predictions. The intrinsic fatigue crack

growth (FCG) rate is that which is governed by crack tip chemical and mechanical driving forces, independent of external influences of closure, deflection and bulk chemical factors.

Electrical potential monitoring of physically short (0.3 to 5 mm) fatigue cracks, with programmed stress intensity range (ΔK) and stress ratio (R), successfully yielded intrinsic crack growth kinetics for high strength aluminum alloys (Piascik and Gangloff, 1988a). Application of these methods to alloy 2090 in aqueous chloride electrolytes evidenced good corrosion fatigue resistance relative to alloy 7075, a potentially important effect of surface films and a notable lack of classical hydrogen embrittlement (Piascik and Gangloff, 1988b). The current work examines corrosion fatigue in purified gaseous environments to further understand these damage mechanisms.

EXPERIMENTAL PROCEDURE

Two high strength aluminum alloys, Al-Li-Cu-Zr alloy 2090 and Al-Zn-Mg-Cu alloy 7075-T651 rolled to plate, were studied in the unrecrystallized peak aged condition. Compositions, heat treatment, microstructure and mechanical properties are summarized in Table 1. The crystallographic texture of alloy 2090 is similar to that reported by Yoder et al., (1987); precipitate structures are equivalent to those analyzed by Cassada et al., (1987).

Table 1. Material Properties

Chemical Composition (WT %):

ALLOY 2090 (3.8 cm thick plate)

Li	Cu	Zr	Fe	Si	Mn
2.14	2.45	0.09	0.05	0.04	0.00
Mg	**Cr**	**Ni**	**Ti**	**Na**	**Zn**
0.00	0.00	0.00	0.01	0.001	0.01

ALLOY 7075 (6.4 cm thick plate)

Zn	Mg	Cu	Cr	Zr	Fe
5.74	2.31	1.58	0.20	0.01	0.26
Si	**Mn**	**Ni**	**Ti**	**Na**	**Ca**
0.10	0.05	0.01	0.05	0.000	0.0001

Mechanical Properties: (Long-Transverse,Peakaged)

	Yield	Ultimate
ALLOY 2090	496 MPa	517 MPa
ALLOY 7075 (T651)	466 MPa	540 MPa

Alloy 2090 Material Condition:

Solution treated, water quenched and stretched.
Peakaged 190°C - 4 hrs

Alloy 2090 Microstructure:

Grain size - 3.3 mm (trans.); 0.11 mm (short trans.)
Subgrain size - 15 μm (trans.); 5 μm (short trans.)

Fatigue crack propagation experiments were conducted with single edge notched (SEN) specimens (10.16 mm wide, 2.54 mm thick, 0.25 or 0.89 mm notch depth) machined in the L-T orientation at 1/3 plate thickness. The growth of short cracks, sized between 0.3 and 5 mm, was monitored continuously by a

direct current electrical potential method including 8 to 12 amps current, 0.1 μV potential measurement resolution, 3 μm crack length resolution and an analytical calibration relation (Gangloff, 1982). Long crack compact tension (CT) experiments, with compliance monitoring, were conducted in accordance with ASTM E647, (1988).

Specimens were stressed cyclically (sine wave) with a 44.5 kN servohydraulic test frame at a frequency of 5 Hz in load control. By computer measurement and feedback control, ΔK was maintained constant over segments of growing crack length (0.5 to 1 mm), with step reductions in constant ΔK at constant K_{max} producing increasing stress ratio (R) (Piascik and Gangloff, 1988a). A single specimen characterizes intrinsic and transient to steady state corrosion fatigue crack growth rates for the moderate ΔK Paris regime and for near threshold at high R (namely, ripple loading) (Gao et al., 1988, Crooker et al., 1987). For CT specimens, continuously decreasing ΔK for constant R or K_{max} is accomplished by established methods with controlled shedding rate, C (Saxena et al., 1978, Herman et al., 1988). Crack growth rates (da/dN) are calculated by linear regression analysis of crack length (a) versus load cycles (N) data for constant ΔK and by secant methods for continuously decreasing ΔK. Out of plane cracking, common to Al-Li alloys was not produced by the short crack method.

Fatigue experiments in static gaseous environments; including 2 kPa helium, 20 kPa oxygen and 2 kPa water vapor; were performed in a bakable, metal bellows and gasket-sealed, chamber. Prior to testing, the chamber was evacuated to below 3 μPa and backfilled at low flow with high purity gas (99.998% pure helium or oxygen), further purified by passage through a liquid nitrogen cold trap (Method A). An improved procedure (Method B) was employed for selected experiments. Helium was purified by passage through molecular sieve at 23°C to remove H_2O, followed by a reactive, hot titanium alloy chip getter to further reduce H_2O, O_2 and H_2 contaminants. Fatigue loading times were minimized for this second method to limit environment contamination due to outgassing. A quartz vial, attached to the vacuum chamber and containing distilled water, was used for the water vapor experiments. This water was further purified by repeated (3 times) freezing, evacuation, and boiling. Pressures were measured with a capacitance manometer and specimen temperature was monitored by an attached thermocouple.

RESULTS AND DISCUSSION

Intrinsic Fatigue Crack Growth in Moist Air

The intrinsic fatigue crack growth characteristics of alloy 2090 in moist air (>30% R.H.) are accurately characterized by the short crack, ΔK control method, Fig. 1. Data points (Δ) labeled with R, relate to a short edge crack, less than 4 mm in depth. These seven constant ΔK levels of crack growth were obtained by step increases and decreases in R at a constant K_{max} of 17 MPa$\cdot$m$^{1/2}$. Crack growth rates were linear for each ΔK segment, without rate transients. Delay retardation was never observed after a ΔK change, due to constant K_{max} and maximum plastic zone size.

Excellent agreement is observed between short crack, constant ΔK-step increased R and long crack, continuously decreasing ΔK constant K_{max} experimental results. Plotted in Fig. 1 are data for a continuously decreasing ΔK experiment at constant K_{max}, conducted with a CT specimen and two K-gradient parameters; C=-188 m^{-1} for ΔK ranging from 13 MPa$\cdot$m$^{1/2}$ to 8 MPa$\cdot$m$^{1/2}$ and C=-394 m^{-1} for ΔK<8 MPa$\cdot$m$^{1/2}$. Because the experiment was per-

formed at constant K_{max}, the high K-gradient parameter (ASTM E647 recommends $C > -80\ m^{-1}$) does not introduce overload effects causing reduced da/dN. The data in Fig. 1 are in excellent agreement with literature results for alloy 2090 (Piascik and Gangloff, 1988a, Herman et al., 1988).

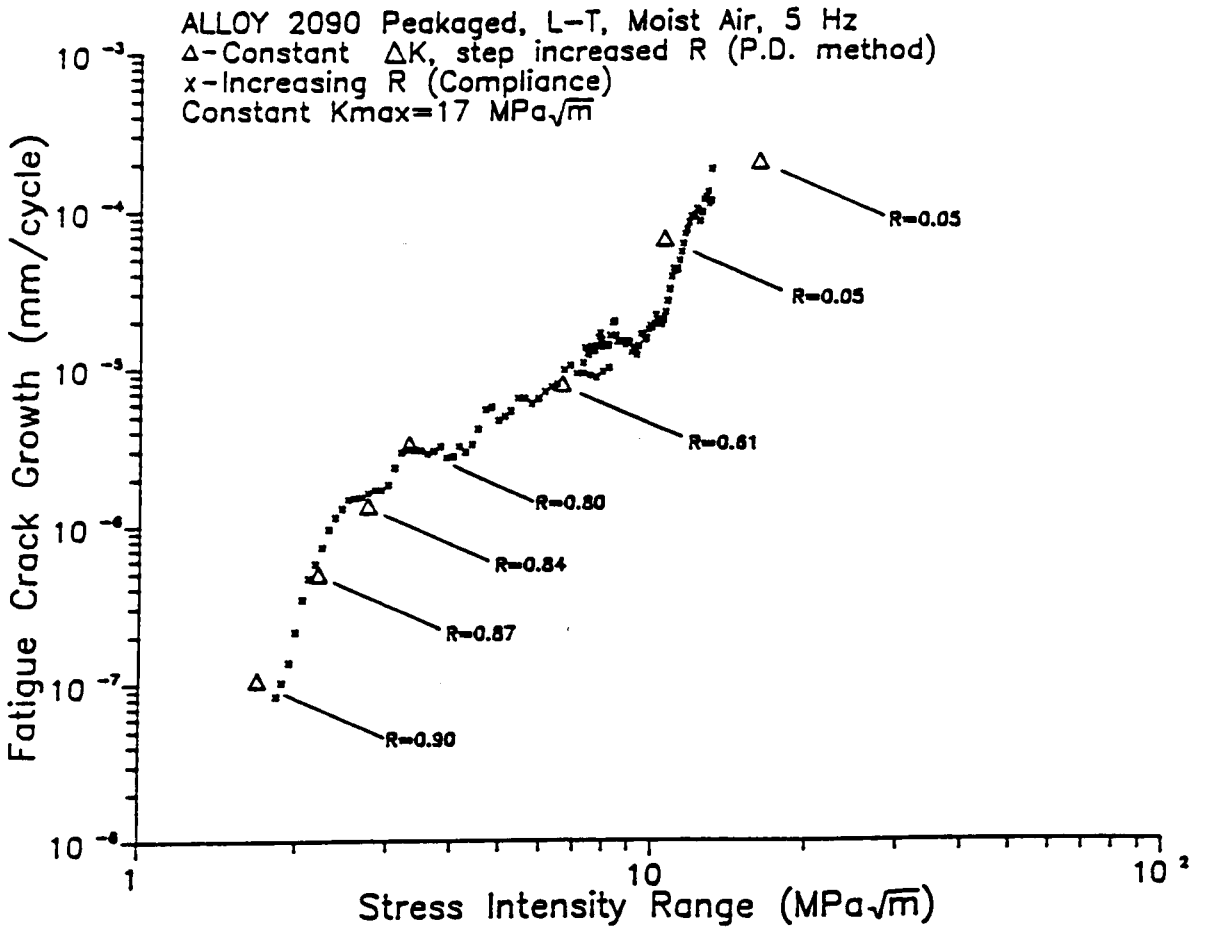

Fig. 1. The intrinsic fatigue crack growth behavior of alloy 2090 in moist air.

Because opening loads were not measured for short crack specimens, compliance based experiments were performed using long crack SEN specimens (38.1 mm wide, 5.0 mm thick, 5.0 mm notch depth) to demonstrate that intrinsic rates of crack growth are measured at low ΔK. For cracks ranging from 5 mm to 13 mm in depth, interfering closure was not observed for R greater than 0.5 and over the ΔK regimes represented in Fig. 1. It is therefore unlikely that closure affects the growth rates of short cracks (< 5 mm) for R greater than 0.6 and ΔK less than 7 $MPa \cdot m^{1/2}$. Roughness induced closure may occur during the moderate ΔK (R=0.05) experiments shown in Fig. 1. Severe deflected crack growth is observed, increasing the likelihood for crack wake closure if Mode II displacements occur. Notably, however, minimal closure was reported for peakaged alloy 2090 at ΔK greater than 9 $MPa \cdot m^{1/2}$ and R=0.1 (Venkateswara Rao et al., 1988).

FCG in Controlled Gaseous Environments

FCG of Alloy 7075 in Gaseous Environments. Fig. 2 contains the results of short crack experiments performed with alloy 7075 in water vapor, helium (purified by Method A), and oxygen. At moderate cyclic stress intensity and low R, a factor of three increase in da/dN is observed in water vapor compared to helium, and oxygen retards fatigue crack growth by a factor of two compared to helium. These results agree with previous findings; dashed lines in Fig. 2 (Gao et al., 1988); where accelerated crack growth was observed for water vapor followed by argon, vacuum, and oxygen. Accelerated growth in water vapor is consistent with hydrogen embrittlement (Gao et al., 1988) and retarded crack growth in oxygen may be caused by oxide induced crack closure, however, surface film effects have not been ruled out. The roles of crack tip rewelding in vacuum and of slip dispersion and irreversibility for oxide covered surfaces remain speculative. Since physically adsorbed He or Ar molecules minimize each process and favor reversible crack tip deformation, such gases provide a reference basis for plastic deformation dominated fatigue damage.

At low ΔK, increased crack growth rate is correlated to the presence of water vapor. The results shown in Fig. 2 reveal accelerated crack growth in 2 kPa water vapor followed by a slight reduction in da/dN for helium and a factor of five reduction in crack growth rate for oxygen compared to water vapor. Notably, the water vapor and helium results exhibit similar crack growth rates compared to moist air, the shaded area in Fig. 2. Here, the upper bound represents intrinsic fatigue crack growth results from microstructural small crack experiments (Lankford and Davidson, 1986) and the lower bound is from high R, long crack experiments (Herman et al., 1988). These rates are significantly faster than crack growth in vacuum.

Petit and coworkers suggest that near-threshold fatigue crack growth in H_2O contaminated nitrogen is rapid relative to dynamic vacuum and similar to moist air due to hydrogen embrittlement (Petit and Zeghloul, 1988). Closure corrected compact tension results in Fig. 2 show accelerated crack growth for nitrogen containing 3 ppm H_2O compared to vacuum. (For vacuum, the upper bound represents results from short crack experiments and the lower bound is the result of closure corrected compact tension measurements.) This acceleration of cracking in N_2/H_2O is consistent with current data for alloy 7075-T651 in Fig. 2. The He environment, purified by Method A, contained between 1 and 5 ppm water due to ineffective cold trap purification and chamber and specimen outgassing. It is not clear why low levels of water vapor are embrittling, because low pressure H_2O molecule transport from the bulk environment to the crack tip may be insufficient to support hydrogen production (Gao et al., 1988). Petit did not consider this kinetic factor when claiming near threshold hydrogen embrittlement in dilute water vapor. We evaluate this consideration for alloy 2090.

Retarded da/dN for oxygen, under closure free high R conditions, suggests that crack tip oxide films mitigate fatigue damage by either precluding contaminant based hydrogen production or by affecting slip processes. The relationship between purely inert gas crack growth rates and values for O_2 must be characterized to resolve the effect of surface films. Such data are obtained for Al-Li alloy 2090, and the competing effects of hydrogen and film formation are examined.

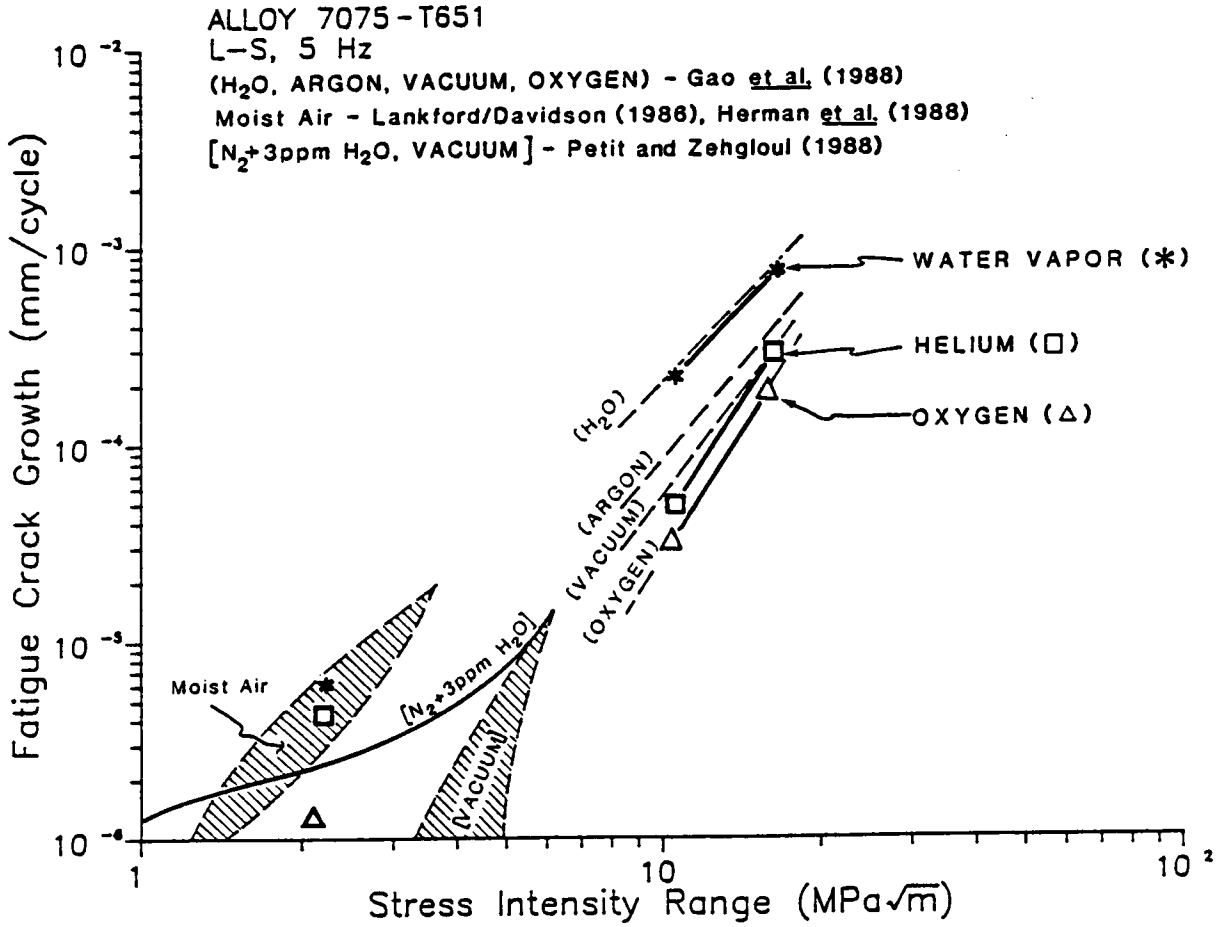

Fig. 2. The fatigue crack growth behavior of alloy 7075-T651 in gaseous environments.

FCG of Alloy 2090 in Gaseous Environments. Shown in Fig. 3 are the results of short crack experiments on alloy 2090 in water vapor, helium (purified by Method B), oxygen, and moist air. At moderate ΔK, da/dN for helium, oxygen and water vapor are equal and only slightly greater than moist air. Retarded fatigue crack growth, a maximum reduction by a factor of five at 11 $MPa \cdot m^{1/2}$, is observed for oxygen. Constant ΔK results plotted in Figs. 2 and 3 represent intrinsic crack growth, not considered in previous studies. At moderate ΔK and low R, extrinsic effects are minimized by short crack lengths and closure free crack growth is ensured by evaluating each constant ΔK experiment for constant da/dN.

Increased crack growth rate in alloy 2090 is correlated to the presence of water vapor for near threshold loading, similar to 7075. At low ΔK and high stress ratio, results in Fig. 3 reveal that 2 kPa H_2O produces the fastest growth followed by moist air. Equal factors of eight reduction in da/dN are observed for helium and oxygen compared to pure water vapor. A comparison of moist air results with the accelerated fatigue crack growth observed for water vapor and the retarded da/dN for oxygen suggests a complex water vapor/oxygen environmental effect for alloy 2090 in moist air.

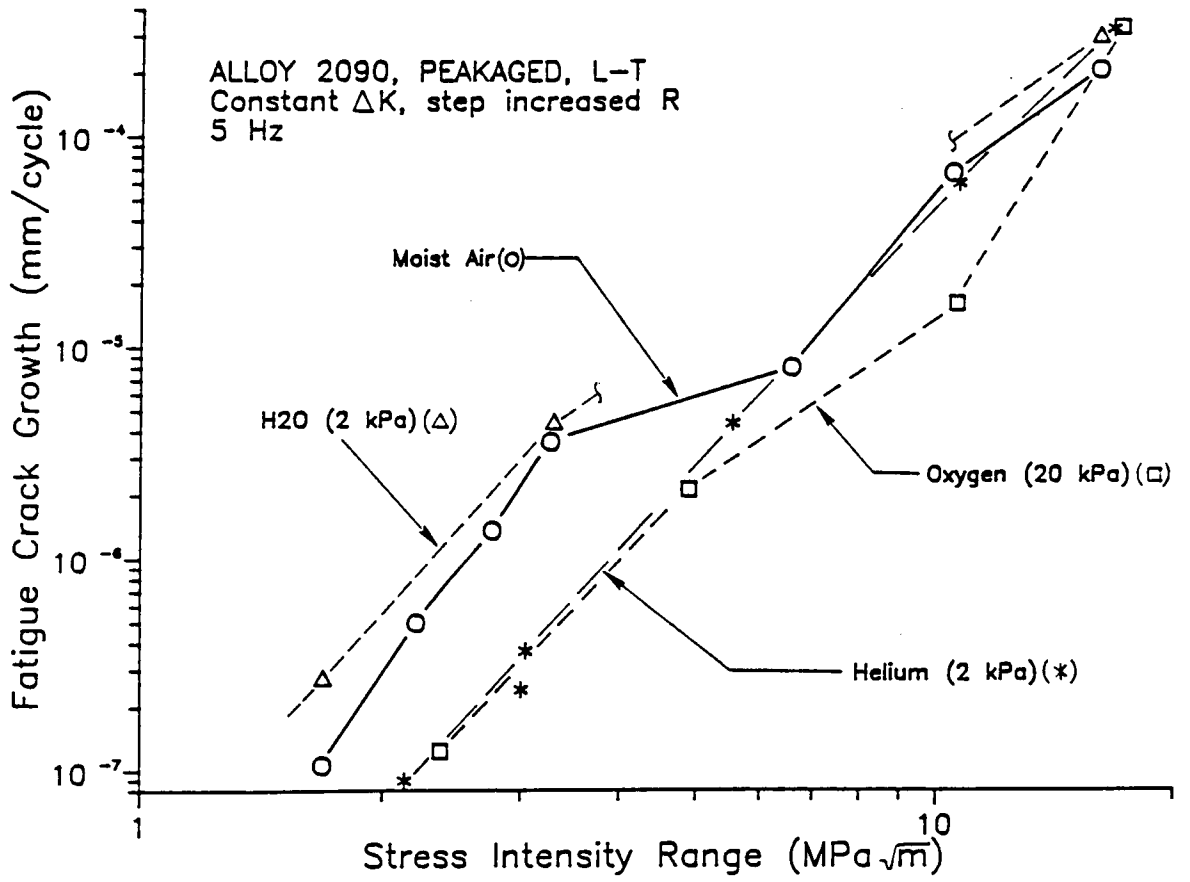

Fig. 3. A comparison of the fatigue crack growth characteristics of alloy 2090 in purified helium, oxygen, water vapor and moist air.

FCG of Alloy 2090 and 7075 in Water Vapor and Helium. Fig. 4 reveals that alloy 2090 generally exhibits a reduced intrinsic fatigue crack growth rate for water vapor compared to 7075. At moderate cyclic stress intensity, crack growth in helium is equivalent for the two alloys. (Note that helium was purified by Method A for alloy 7075 and by Method B for alloy 2090. For moderate ΔK, this difference is not significant based on H_2O pressure-frequency data Gao et al., 1988). Alloy 2090, in 2 kPa water vapor, exhibits similar fatigue crack growth rates compared to helium. A factor of two increase in da/dN is observed for Alloy 7075 in 2 kPa water vapor compared to helium.

For near threshold cracking, fatigue in 7075 for 2 kPa water vapor is significantly faster, a factor of ten, than that observed for 2090. Alloy 2090 exhibits a factor of ten increase in da/dN for 2 kPa water vapor compared to pure helium (Method B), while alloy 7075 exhibits only a slight increase in fatigue crack growth rate for 2 kPa water vapor compared to helium (Method A). Alloy 2090 crack growth rates in the gettered helium environment (Method B) are fifteen times less than those observed for 7075 exposed to cold trap purified helium (Method A). Because of possible helium contamination, the crack growth rate due to mechanical fatigue in 7075 is unknown and the cause for this dramatic effect is unclear.

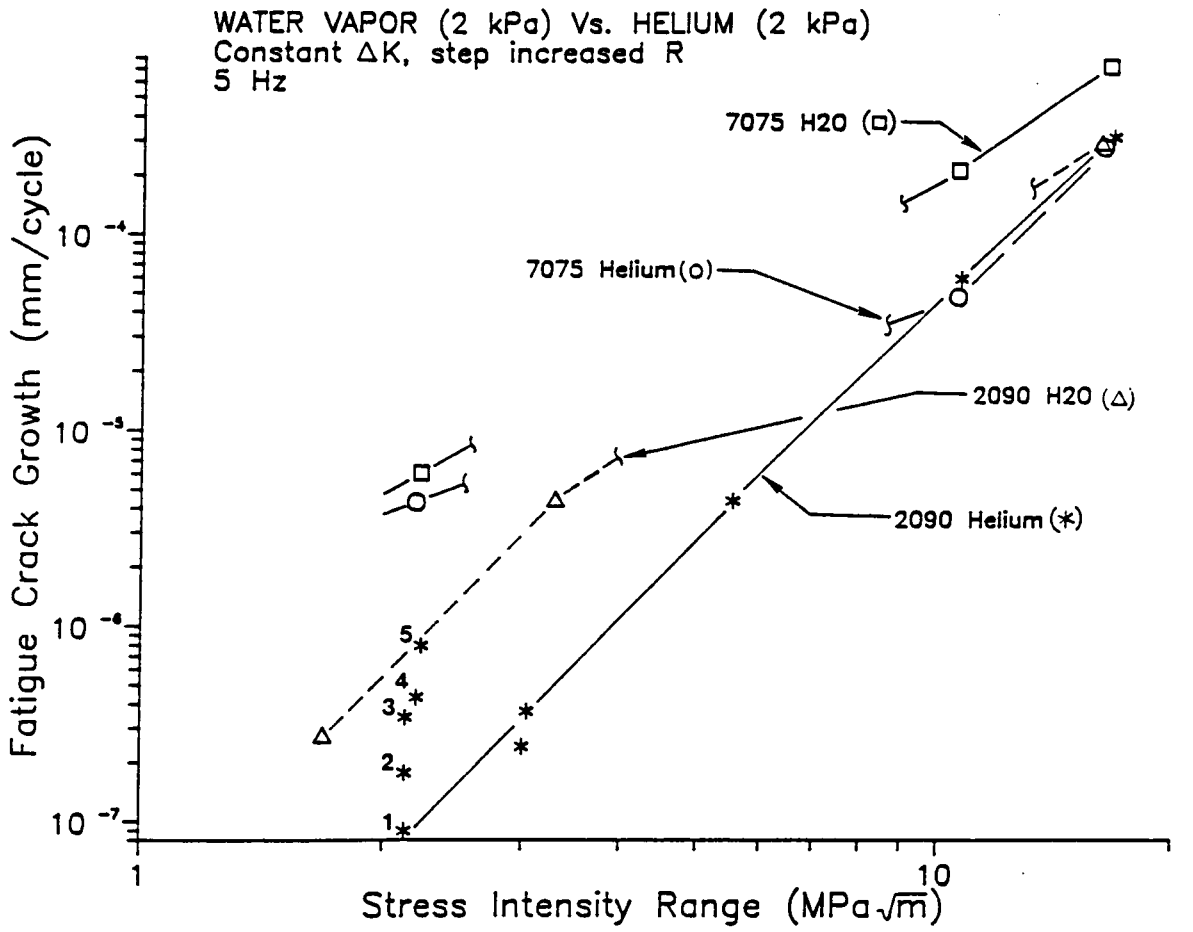

Fig. 4. The fatigue crack growth behavior of alloy 2090 compared to alloy 7075 for water vapor and helium.

A series of near threshold constant ΔK (2.2 MPa·$m^{1/2}$, R=0.88) experiments confirm that small (ppm) levels of H_2O in otherwise pure helium accelerate fatigue crack growth in alloy 2090. Data points 1, 2, and 3 in Fig. 4 represent the sequential measurement of fatigue crack growth rate during a constant ΔK experiment. Point 1 was obtained immediately after helium (Method B) introduction, followed by crack growth rate measurements 2 and 3 as cycling progressed. The fatigue crack growth rate increased by a factor of five, suggesting that environment purity changed during crack growth. After chamber evacuation, the experiment was repeated (data point 4) using cold trap purified helium (Method A), with the wall of the vacuum chamber initially heated for 15 minutes to simulate contaminant outgassing. Data point 4 exhibits an accelerated crack growth rate, similar to point 3 and equivalent to fatigue in moist air. A third experiment, data point 5 in Fig. 4, was performed in pure helium (Method B) containing 3 ppm H_2O. (The chamber was evacuated to 3 μPa, 3 ppm H_2O was added based on capacitance manometer measurement and the chamber backfilled with 2 kPa helium.) The crack growth rate obtained for the 3 ppm (7 mPa) H_2O/helium environment increased 10-fold compared to dry helium, point 1 in Fig. 4, and is similar to the value obtained for the 2 kPa water vapor experiment. The results for alloy 2090 are consistent with results for 7075, Fig. 2 and the findings of Petit and Zeghloul, (1988).

Hydrogen Embrittlement. Water vapor enhanced FCG in aluminum alloys is driven by hydrogen produced through reactions of water vapor with newly created crack tip surfaces (Gao et al., 1988). Because aluminum alloy surfaces react rapidly, the crack growth rate is limited by impeded molecular gas transport to the crack tip. Molecular transport is reduced with decreasing pressure or increasing frequency below a saturation level, resulting in reduced hydrogen production and lower fatigue crack growth rates. Measurements and modeling suggest that the saturation pressure is 5 to 10 Pa for a variety of aluminum alloys loaded at 5 Hz. Environmental embrittlement is eliminated at pressures below about 1 Pa (5 Hz). These trends were established for moderate ΔK, above about 7 $MPa \cdot m^{1/2}$ and low R below about 0.1.

Results of corrosion fatigue experiments at moderate ΔK and saturation frequency-H_2O pressure suggest a reduced hydrogen effect in alloy 2090 compared to 7075. Alloy 7075 results are consistent with modeling (Gao et al. 1988) where da/dN in 2 kPa water vapor (saturation) is greater than rates in helium. For alloy 2090, fatigue crack growth rates are similar for the two environments. The difference in behavior for alloys 2090 and 7075 suggests that:

1. The saturation pressure for alloy 2090 is higher due to a rough fracture surface. (Surface roughness impedes molecular transport to the crack tip (Gao et al., 1988)).
2. The limiting coverage at saturation is low for alloy 2090 compared to 7075 due to different surface reactions.
3. Surface reactions in alloy 2090 are slow and rate limiting. Alternately, equal hydrogen forms but less enters alloy 2090 due to surface impedance, viz the formation of lithium hydride or hydroxide.
4. For equal surface hydrogen production, embrittlement is reduced or bulk hydrogen diffusion in alloy 2090 becomes rate limiting.

The precise mechanism is unclear.

Near threshold, extremely low concentrations of water vapor exacerbate FCG in alloys 2090 and 7075. Specifically, data establish a three order of magnitude reduction in the saturation value of H_2O pressure to load frequency ratio. These results reveal a significant extension of the transport controlled crack growth region for alloy 2090 near threshold compared to high ΔK behavior. Increased molecular transport to the crack tip due to increased mean crack opening at high R explains a portion of the reduced H_2O saturation level (Gao et al., 1988). Reduced, but highly localized, crack tip reaction area could also explain the reduction in saturation value at low ΔK. For the moderate ΔK regime, the crack tip contains newly created surfaces, possibly along distributed slip steps, that act collectively as active sites for hydrogen production and subsequent embrittlement. As the cyclic stress intensity is lowered, crack tip damage is localized, possibly along single slip or cleavage planes, reducing the area of active sites. Because of the reduced area, fewer molecules of water vapor are required for coverage and saturation is obtained at a greatly reduced pressure. Even though fewer hydrogen atoms may be produced at the crack tip, the effective hydrogen concentration may not be altered if embrittlement is localized. These speculations are being examined.

Film Effects. Equal fatigue crack growth rates for oxygen and helium at low ΔK in alloy 2090 demonstrate that surface films do not alter crack tip damage by affecting either slip irreversibility or homogenized crack tip

deformation. Surface films are thought to increase fatigue crack growth rates for planar slip materials, particularly age hardened Al alloys, preventing reversible slip (Jata and Starke, 1986). Conversely, surface films could decrease da/dN by homogenizing localized deformation. The lack of an environmental effect of oxygen compared to helium suggests that surface films do not change the mechanical crack tip damage mechanism. Fatigue studies in purified oxygen provide an excellent means of isolating film effects; a tool here-to-fore not exploited.

Alloy 2090 exhibits a slower fatigue crack growth rate in moist air compared to pure water vapor and accelerated da/dN relative to oxygen. Oxygen molecules in moist air competitively adsorb with water vapor, inhibiting the formation of free hydrogen or forming a crack tip surface film that blocks hydrogen entry ahead of the crack tip.

CONCLUSIONS

1. Gaseous environmental effects on FCG in Al-Li-Cu alloy 2090 are significant, particularly near threshold, and are not closure dominated. Growth rates decrease according to the order: water vapor, moist air, helium and oxygen; the latter two cause equivalent da/dN.
2. A hydrogen embrittlement effect is supported by accelerated fatigue crack growth for water vapor. The unexpectedly strong H_2O effect near threshold is attributed to localized crack surface reaction and opening shape.
3. No difference in the intrinsic fatigue crack growth rates for oxygen compared to inert helium indicates that surface films do not influence mechanical crack tip damage mechanisms.
4. Fatigue crack growth rates in moist air are governed by a complex oxygen/hydrogen embrittlement damage mechanism.
5. Alloy 2090 exhibits better intrinsic transgranular environmental fatigue crack growth, and by inference hydrogen resistance, compared to alloy 7075.

ACKNOWLEDGEMENTS

Financial support provided by the NASA-Langley Research Center, grant NAG-1-745 with D.L. Dicus as monitor, is gratefully acknowledged. Alloy 2090 was provided by E.L. Colvin (Alcoa Technical Center), transmission microscopy by W.A. Cassada and experimental assistance by W.C. Porr.

REFERENCES

ASTM E647-88 (1988). "Standard Test Method for Measurement of Fatigue Crack Growth Rates", Annual Book of ASTM Standards, ASTM, Philadelphia, PA, Vol. 03.01.

Cassada, W.A., G.J. Shiflet and E.A. Starke, Jr, (1987). Scripta Met., 21, 387-392.

Crooker, W.A., J.A. Hauser and R.A. Bayles (1987). In: Proc. Conf. Environmental Degradation of Engineering Materials III, M.R. Louthan, Jr., R.P. McNitt and R.D. Sisson, Jr., eds., 521-532.

Gangloff, R.P. (1982). In: Advances in Crack Length Measurement, C.J. Beevers, ed., pp. 175-229, EMAS, UK.

Gao, M., P.S. Pao and R.P. Wei (1988). Metall. Trans., 19A, 1739-1750.

Herman, W.A., R.W. Hertzberg, and R. Jaccard (1988). "A Simplified Laboratory Approach for the Prediction of Short Crack Behavior in Engineering Structures", J. Fatigue and Fracture of Engr. Materials and Structures, in press.

Jata, K. and E.A. Starke, Jr. (1986). Metall. Trans., 17A, 1011-1026.

Lankford, J. and D.L. Davidson (1986). In: Small Fatigue Cracks, R.O. Ritchie and J. Lankford eds., pp. 51-71, AIME, Warrendale, PA.

Petit, J. and A. Zeghloul (1988). "Environmental Influence on Threshold and Near Threshold Behavior of Short and Long Fatigue Cracks", Metall. Trans., in press.

Piascik, R.S. and R.P. Gangloff (1988). "Environment Assisted Degradation Mechanisms in Al-Li Alloys", Report No. UVA/528266/MS88/101, University of Virginia.

Piascik, R.S. and R.P. Gangloff (1988). "Aqueous Environment Effects on Intrinsic Corrosion Fatigue in an Al-Li-Cu Alloy", In: Environment-Induced Cracking of Metals, R.P. Gangloff and M.B. Ives, eds., NACE, Houston, in press.

Ricker, R.E. and D.J. Duquette (1988). Metall. Trans., 19A, 1775-1783.

Saxena, A., S.J. Hudak, Jr., J.K. Donald, and D.W. Schmidt (1978). J. Test. Eval., 6, (3), 167-174.

Venkateswara Rao, K.T., W. Yu and R.O. Ritchie (1988). Metall. Trans., 19A, 549-569.

Yoder, G.R., P.S. Pao, M.A. Inman and L.A. Cooley (1987). In: Competitive Advances in Metals and Processes, Vol. 1, pp. 25-37, SAMPE, Covina, CA.

Proceedings, World Congress on Environmental Cracking of Metals, M. B. Ives and R. P. Gangloff, eds., NACE, Houston, TX, In Press.

AQUEOUS ENVIRONMENT EFFECTS ON INTRINSIC CORROSION FATIGUE CRACK PROPAGATION IN AN Al-Li-Cu ALLOY

ROBERT S. PIASCIK AND RICHARD P. GANGLOFF
Department of Materials Science
University of Virginia
Charlottesville, VA 22901 USA

ABSTRACT

Intrinsic corrosion fatigue crack growth in Al-Li-Cu alloy 2090 exposed to aqueous NaCl is examined by new fracture mechanics methods applied to short cracks of depth less than 5 mm. Two regimes of the environmental effect are studied; low mean stress-high cyclic stress intensity range and high stress ratio-near threshold or ripple loading. Within each regime alloy 2090 exhibits accelerated transgranular fatigue crack growth in an aqueous NaCl environment, with anodic polarization, relative to moist air and inert helium. Corrosion fatigue crack growth in the LT orientation exhibits a crystallographic "cleavage" morphology at low ΔK and highly deflected slip band cracking at high ΔK. Aqueous NaCl experiments reveal mildly increased fatigue crack growth rates with increased cyclic frequency, strongly reduced da/dN with cathodic polarization and a decreased environmental effect due to Li_2CO_3 addition. Hydrogen embrittlement is suspected, with surface films retarding crack tip environmental reactions for hydrogen production and dissolution. Alloy 2090 is more resistant to aqueous corrosion fatigue crack growth compared to Al-Zn-Mg-Cu alloy 7075, and behaves similar to conventional 2000 series alloys such as 2219.

INTRODUCTION

The objective of this research is to characterize and understand intrinsic fatigue crack propagation in advanced aluminum-lithium based alloys, with emphasis on the damage mechanisms for environmentally assisted transgranular cracking. While the importance of complex extrinsic contributions (namely crack closure, delamination and crack deflection) to the fatigue crack propagation (FCP) resistance of Al-Li alloys is established (1), gaseous and aqueous environmental effects have not been examined.

Intrinsic corrosion fatigue crack growth is that which is governed by crack tip microstructure and mechanical and chemical driving forces; independent of the external influences of closure contact, crack deflection and transient chemical factors that alter steady state crack growth. We believe that it is fundamentally important for mechanistic interpretation to define intrinsic fatigue crack growth rates which are: 1) constant with constant applied ΔK for any crack size or specimen geometry and 2) constant with constant applied bulk environment conditions for any number of load cycles, crack size or specimen geometry.

In this study fracture mechanics experiments; developed to characterize intrinsic FCP for benign environment exposure and based on short crack, programmed stress intensity methods (2); are extended to investigate the effect of aqueous sodium chloride. Emphasis is placed on electrochemical control of the environment and on high resolution measurements of fatigue crack length changes in response to chemical variations.

EXPERIMENTAL PROCEDURE

A 3.8 cm thick plate of an advanced Al-Li-Cu-Zr alloy (AA 2090) was studied in the rolled, unrecrystallized, peak aged condition. Alloy composition, heat treatment, mechanical properties and microstructure, defined by optical and transmission electron metallography, are summarized in Table 1. Results are compared to Al-Zn-Mg-Cu alloy 7075-T651 (6.4 cm rolled plate); chemical composition and mechanical properties are shown in Table 2.

Corrosion behavior was characterized by standardized potentiodynamic polarization experiments at a standard scan rate of 0.16 mV/sec in helium deaerated, 1% aqueous NaCl at pH 8 and 297° K (3). All scans were performed from the most cathodic to the most anodic potentials. Corrosion fatigue experiments were conducted with specimens fully immersed in flowing (30 ml/min), helium deaerated, 1% NaCl (pH 8) in a 1.5 l sealed plexiglass

chamber. Electrode potential was maintained constant by a Wenking potentiostat and platinum counter electrodes isolated from the solution through asbestos frits. Results are compared to fatigue crack growth in moist air (30 to 60% RH) and in purified helium contained in a bakable, metal bellows and gasket-sealed chamber capable of a dynamic vacuum of 1 μPa, as detailed elsewhere (4).

Short crack, fatigue propagation experiments were conducted with single edge notched specimens (10.16 mm wide, 2.54 mm thick, 0.25 or 0.89 mm notch depth) machined in the LT orientation at the one-third thickness position in the rolled plate. Pinned, freely rotating grips were employed, consistent with the stress intensity solution (5). The growth of short edge cracks, of total length (a) between 0.35 and 5 mm, was monitored continuously by a direct current electrical potential method including 8 to 12 amps current, 0.1 μV potential measurement resolution and an analytical calibration relation (6). This method was successfully applied to aluminum alloys, with better than 3 μm crack growth resolution and long term (10 day) stability for near threshold growth rate measurements (2). Long crack compact tension (CT) experiments, with compliance monitoring, were conducted in accordance with ASTM E647 (7).

Intrinsic and transient or steady-state corrosion fatigue crack propagation was studied for both the high stress intensity (ΔK) Paris regime and near threshold growth rates. Edge cracked specimens were stressed cyclically (sine waveform; 0.07 Hz < frequency < 20 Hz; 0.05 < stress ratio < 0.95) in a closed loop servohydraulic machine operated in load control. Employing computer measurement and feedback control, ΔK was maintained constant over segments of growing crack length (about 0.25 to 1 mm), with step reductions (or increases) in ΔK at constant K_{max}, producing increasing (or decreasing) stress ratio (R). Crack growth rates (da/dN) were calculated by linear regression analysis of crack length (a) versus load cycles (N) data. For a single specimen, the load sequence initially probes high ΔK, low

R cracking; followed by near threshold ΔK, high R fatigue for deeper crack depths. Short crack length for the former and high stress ratio for the latter conditions minimize complicating extrinsic effects. Crack bifurcation was never observed. Continuous reduction in ΔK at constant K_{max} provides an effective characterization of intrinsic fatigue crack growth (8). Step changes in constant ΔK with increasing or decreasing R more effectively characterizes transient to steady state crack propagation associated with ΔK changes, electrochemical variables and microstructure.

RESULTS AND DISCUSSION

Corrosion Characteristics

Potentiodynamic polarization data are summarized in Fig. 1a for peak aged alloy 2090 exposed to deaerated and oxygen containing 1% NaCl solutions. In oxygen containing aqueous NaCl, the open circuit potential of alloy 2090 is near the breakaway potential, resulting in extensive surface pitting. Deaeration of the solution limits the oxygen reduction reaction and decreases the open circuit potential in the cathodic direction, forming a passive region extending from -1.0 V to -0.7 V (SCE). At passive potentials, general corrosion and pitting are greatly reduced. Long term (8 day) constant potential experiments (-0.760 V SCE, deaerated 1% NaCl) none-the-less reveal that T_1 precipitates at subgrain boundaries and constituent particles (Al_7Cu_2Fe) are sites of localized attack, Fig. 1b (2).

Corrosion fatigue experiments were performed in deaerated 1% NaCl to limit fracture surface corrosion and pitting, to reduce crevice corrosion at the electrical potential probes and to minimize electrolyte IR-type errors in measured potential. Since the open circuit potential of alloy 2090 varies by 100 to 400 mV during long term exposure, fatigue experiments were performed at a constant anodic potential of -0.760 V (SCE) and a cathodic potential of either -1.160 or -1.260 V (SCE), Fig. 1a.

Intrinsic Fatigue Crack Growth in Moist Air and Helium

The intrinsic fatigue crack growth (FCG) characteristics of alloy 2090 in moist air and purified helium are shown in Fig. 2. The data points (Δ) for moist air were calculated from the linear a versus N responses shown in Fig. 3, for seven constant ΔK levels obtained by step increases or decreases in R at a constant K_{max} of 17 MPa·$m^{1/2}$. Note that linear crack growth for the low ΔK region (ΔK=1.7/R=0.90) reveals no evidence of delay retardation, demonstrating that ΔK reductions at constant K_{max} do not induce overload effects presumably because the maximum or forward loading plastic zone size is constant.

Results for short crack, constant ΔK-step changed R and long crack, continuously decreasing ΔK constant K_{max} experiments are in excellent agreement. Shown in Fig. 2 are the results of a continuously decreasing ΔK experiment conducted with a large crack compact tension specimen (LT) and using two K-gradient parameters; C=-188 m^{-1} for ΔK ranging from 13 MPa·$m^{1/2}$ to 8 MPa·$m^{1/2}$ and C=-394 m^{-1} for ΔK from 8 MPa·$m^{1/2}$ to threshold. Because the experiment was performed at constant K_{max}, the low K-gradient parameter (ASTM E647 recommends C>-80 m^{-1}) does not introduce overload effects causing reduced da/dN. The data contained in Fig 2 are in excellent agreement with literature results for alloy 2090 (1,2,8) and represent the intrinsic FCG behavior of this alloy for moist air.

Accelerated transgranular fatigue crack growth in moist air compared to helium reveals the damaging effect of water vapor, and suggests a hydrogen embrittlement mechanism for alloy 2090 (4). Shown in Fig. 2 are the results of fatigue crack growth experiments performed in purified helium. At high ΔK, da/dN for helium and moist air are equivalent, revealing little environmental effect. At low ΔK and high R, moist air causes a factor of five increase in intrinsic fatigue crack growth compared to that for helium. Crack growth rate data in purified

He provide a mechanical basis for analysis of aqueous environmental effects. Moist air data in Fig. 2 provide the customary base line.

Aqueous Corrosion Fatigue

Intrinsic CF Characteristics. Shown in Fig. 4 is a comparison of the intrinsic transgranular corrosion fatigue crack growth kinetics of alloy 2090 in helium, moist air, deaerated 1% NaCl (-0.760 V and -1.160 V SCE) and deaerated 1% NaCl+0.37% Li_2CO_3 (-0.760 V SCE). All experiments were performed at a cyclic frequency of 5 Hz, using the constant ΔK-step changed R/constant K_{max} sequence similar to that shown in Fig. 3. These results show that alloy 2090 exhibits a moderate environmental effect at high levels of ΔK where differences in crack growth rate are less than three-fold. Near threshold, considerable differences in fatigue crack growth are observed, with a factor of fourteen increase in da/dN revealed by comparing 1% NaCl with anodic polarization and helium; the largest corrosion fatigue effect. In contrast cathodic potential (-1.160 V SCE) reduced fatigue crack growth to a level slightly greater than that observed for moist air, and produced crack arrest above the moist air threshold and similar to fatigue in helium. The addition of Li_2CO_3 to 1% NaCl (-0.760 V SCE) retarded crack growth; the reduction is not as dramatic as that produced by mild cathodic polarization.

Corrosion fatigue experiments performed in aqueous 1% NaCl at constant anodic potential (-0.760 V SCE) show that alloy 2090 exhibits better transgranular corrosion fatigue crack growth characteristics compared to alloy 7075-T651. Results for alloy 7075 are shown by the dashed line in Fig. 4 for the high and low ΔK regimes. At high ΔK, alloy 7075 exhibits a factor of 1.5 to 4 increase in da/dN and at low ΔK 10-fold greater FCG rates are revealed compared to alloy 2090. Alloy 7075 growth rates are in agreement with previous findings by Stoltz and Pelloux, where accelerated fatigue crack growth was observed for 3.5% NaCl with

anodic polarization (9).

For all cases in Fig. 4, crack length increased linearly within the range from 0.35 to 3.5 mm and at constant ΔK. No evidence was obtained for crack geometry dependent increases or decreases in da/dN. While comparisons are limited, the corrosion fatigue effect shown in Fig. 4 is similar to the behavior of 20 to 50 mm long cracks in 2090 and 7075 (9,10). Experiments with short (0.1 to 3 mm) and long (20 to 50 mm) cracks for the steel-aqueous chloride system evidenced dramatic increases in corrosion fatigue crack growth kinetics for the former, and attributed to geometry dependent crack electrochemistry (11). Additional work is in progress to examine "chemical crack size" effects on corrosion fatigue in high strength aluminum alloys.

Frequency Effects. The typical frequency effect on corrosion fatigue crack propagation in 2000 and 7000 series alumiunum alloys (viz. increased or constant da/dN with decreasing frequency) was not observed for alloy 2090 in 1% NaCl (10,12-14).

In deaerated 1% NaCl solution (-0.760 V SCE), alloy 2090 exhibits mildly increased corrosion fatigue crack growth rates with increased frequency at high cyclic stress intensity and little frequency effect at low ΔK. Shown in Fig. 5 is the comparison of average crack growth rate versus frequency at two levels of constant ΔK, 9.9 and 2.2 $MPa \cdot m^{1/2}$. For each frequency, the total variation in crack growth rate (calculated with a two point secant method) and the least squares value are plotted. The numbers shown adjacent to each data point result describe the sequence of experiments conducted on two specimens. At high constant ΔK, a factor of two decrease in fatigue crack growth rate is observed when decreasing the cyclic frequency from 5 to 0.1 Hz. Similar results were reported by Yoder and coworkers for alloy 2090 in aerated 3.5% NaCl (10).

At low ΔK, little difference in fatigue crack growth rate is observed for cyclic frequencies between 0.07 and 20 Hz.

Experiment 4, performed at 0.07 Hz, exhibits a slightly higher fatigue crack growth rate compared to the mean da/dN at 2.2 $MPa \cdot m^{1/2}$. The origin of this result is unclear. Fractographic analysis revealed evidence of increased dissolution for this long term experiment (0.25 mm of crack extension in 8 days), possibly suggesting either an increased driving force for fatigue or simple crack wake corrosion. Long term electrical potential system variations may have contributed to the increased growth rate. The slight reduction in da/dN observed during experiment 6 is attributed to a chemical or mechanical history dependence associated with crack length and shape (15). These factors complicate characterizations of moderate frequency effects in corrosion fatigue.

The important point to be made for Fig. 5 is that corrosion fatigue in alloy 2090 is not exacerbated by decreasing frequency; to the contrary, the opposite trend is likely, particularly at higher ΔK. The rate differences shown here are small, but significant, as demonstrated by resolvable changes in a versus N upon a frequency change at constant ΔK for a single specimen (2).

Polarization Effects. The results of constant ΔK experiments show that corrosion fatigue crack growth in 1% NaCl is mitigated by cathodic polarization. Cathodic polarization da/dN data are compared to the anodic case in Fig. 4. Note the two-fold reduction in rate at high ΔK, increasing to a five-fold decrease at low ΔK and an increase in the approximate threshold stress intensity. Cracking under cathodic potential is similar to the behavior recorded for moist air and enhanced relative to inert He for all ΔK except the near threshold regime.

The beneficial effect of cathodic polarization is clearly evidenced by cyclic crack length measurements at constant ΔK. Fig. 6a reveals that, at low ΔK (2.2 $MPa \cdot m^{1/2}$, R=0.8) and anodic polarization (-0.760 V SCE), a constant crack growth rate is maintained to a crack length of 2.1 mm. Here, a cathodic potential of -1.160 V (SCE) was applied, resulting in crack

arrest consistent with the threshold elevation shown in Fig. 4. At one million load cycles, a potential of -0.760 V (SCE) was again applied. Seventy six hours or 2.2 million additional cycles elapsed before crack growth resumed, achieving a steady state rate similar to the initial anodic condition. A second cathodic polarization of -1.160 V (SCE) reproduced crack arrest. Cathodic polarization also reduced rates of corrosion fatigue at high cyclic stress intensity (9.6 $MPa \cdot m^{1/2}$, R=0.1), as shown in Fig. 6b. After initial cracking at -0.760 V (SCE), a small reduction in da/dN was produced by polarization to -1.160 V (SCE), and a significant, time dependent retardation in crack growth was observed at a cathodic potential of -1.260 V (SCE). At a crack length of 3.1 mm, the applied stress intensity range was decreased to 2.1 $MPa \cdot m^{1/2}$ at R=0.9 with K_{max} maintained constant and the electrode potential was made anodic (-0.760 V (SCE)). A slow recovery to a constant growth rate was observed. Crack growth arrest occurred due to cathodic polarization at -1.160 V (SCE), reproducing the results shown in Fig. 6a. The results of constant ΔK and R experimentation, Fig. 6, are consistent with the single specimen constant ΔK-step changed R results presented in Fig. 4.

The reduction in corrosion fatigue crack growth by cathodic polarization for alloy 2090 is consistent with the findings of other researchers. Cathodic polarization of alloy 7075 in aqueous 3.5% NaCl reduced corrosion fatigue crack propagation at ΔK=11 $MPa \cdot m^{1/2}$ (9). The enhanced stress corrosion cracking resistance of conventional 2000 and 7000 series alloys due to cathodic polarization is documented (16). Consistent with data in Figs. 4 and 6, although not conclusive, the smooth specimen fatigue life of an Al-4.2Mg-2.1Li alloy was increased by mildly cathodic potentials (17).

Ion Addition Effects. The experimental results shown in Fig. 7 demonstrate that a lithium carbonate (Li_2CO_3) addition to 1% NaCl reduces the rate of transgranular corrosion fatigue crack growth at constant ΔK, pH and electrode potential. At a cyclic stress

C-2

intensity of 2.3 MPa·$m^{1/2}$ (R=0.87) and an anodic potential of -0.760 V (SCE), a constant crack growth rate was initially established in deaerated 1% NaCl (pH=8.1). No change in crack growth is observed as the solution pH is increased from 8.1 to 10.4 by addition of NaOH. At a crack length of 1.9 mm, the cell environment was changed by continuously pumping deaerated 1% NaCl+0.37% Li_2CO_3 (pH=10.4) solution from a separate reservoir. After purging the cell with flowing 1% NaCl+0.37% Li_2CO_3, the experiment was resumed, resulting in a thirty percent reduction fatigue crack growth rate. This beneficial effect was reproduced at two higher ΔK levels, Fig. 4.

Fractographic Analysis

The fatigue crack surface morphologies for moist air and deaerated 1% NaCl (-0.760 V SCE) environments exhibit similar components of microscopic fracture, but in different proportions. At high ΔK (15 MPa·$m^{1/2}$), severe planar crack surface deflections due to decohesion or shear separation along intense slip bands and regions of intersubgrain boundary fracture are observed for each environment. Results suggest that NaCl promotes increased sub-grain boundary fracture and reduced crack deflections due to reduced slip band cracking. The latter crack path is dominant for fatigue in moist air (10).

As stress intensity range decreases, the amount of crack tip deflection is reduced and the fracture surface is characterized by increased areas exhibiting a flat crystallographic "cleavage type" appearance. A comparison of the fracture surfaces for moist air and deaerated 1% NaCl (-0.760 V SCE) environments at low ΔK is shown in Fig. 8. In moist air, Fig. 8a, the transgranular fracture surface is crystallographic cleavage with intervening regions of deflected crack growth exhibiting a ductile appearance. The transgranular fracture morphology for 1% NaCl, Fig. 8b, exhibits broad regions of cleavage fracture with little evidence of ductile tearing. Results suggest a greater proportion of crystallographic fracture for aqueous NaCl compared

to moist air.

High angle and sub-grain boundary precipitates, T_2 and T_1, respectively, do not appear to be sites for crack tip dissolution. Detailed examination of the corrosion fatigue crack-final overload fracture interface region reveals no evidence of corrosion. Behind this region, where crack surfaces are exposed to the crevice environment for longer times, small and widely dispersed regions of sub-grain boundary T_1 precipitate corrosion, similar to that shown in Fig. 1b, were observed. No evidence was obtained for T_2 precipitate corrosion along high angle grain boundaries. Secondary cracking along these generally low strength high angle boundaries was not observed for the L-T orientation. Corrosion fatigue was purely transgranular.

MECHANISTIC IMPLICATIONS

Many mechanisms have been proposed to explain rates of environmental cracking in aluminum alloys, including: hydrogen embrittlement, adsorbate decohesion, film rupture/dissolution/repassivation, film induced slip irreversibility, enhanced localized plasticity, and crack tip blunting by corrosion (9,12,13,15-18). In these studies Paris regime corrosion fatigue has been emphasized, crack closure has not been accounted for, and aqueous environments effects on near threshold cracking have not been considered. For fatigue crack growth at moderate ΔK, the cleavage fracture morphology was linked to both hydrogen embrittlement and surface film effects without resolution of the cause. Hydrogen from cathodic reduction in electrolytes and chemical reactions in water vapor is held to embrittle aluminum, with possible contributions from dislocation and grain boundary transport processes. Alternately, surface films suppress plastic deformation by blocking the crack tip emission of dislocations; the local normal stress is elevated causing cleavage.

Based on experimental observations of FCG response to ΔK, frequency, cathodic polarization, and Li_2CO_3 addition; and on the

behavior of alloy 2090 in water vapor and oxygen (4); we speculate that hydrogen embrittlement is likely, but that surface films and crack electrochemistry play an important role in crack tip damage during transgranular corrosion fatigue of alloy 2090. Faster crack growth is correlated with those environmental conditions which promote less protective crack tip surface films, and thus enhance hydrogen entry. This complex interplay and the effects of frequency and cathodic polarization are not consistent with surface reaction or transport limited hydrogen embrittlement, as suggested for steels and 7000 series aluminum alloys (12,13,19,20).

Increased crack growth rates with increasing frequency suggests that time dependent chemical reactions and mass transport within the electrolyte or crack tip plastic zone are rapid, and do not limit environmental crack propagation. Considering mechanical effects, crack tip strain rate is, on average, proportional to loading frequency and stress intensity range raised to a power on the order of 5 (21). At high ΔK mechanical film disruption provides a plausible explanation for the small increase in crack growth with increasing frequency, Fig. 5. Here, crack tip strain rate increases with increasing frequency, the film is locally breached more frequently, and transient dissolution and hydrogen production progress to greater degrees. Crack extensions per unit time and cycle increase. The strong environmental effect for low ΔK may be ascribed to localization of crack tip deformation and mechanical disruption of surface films. Since da/dN is independent of frequency, it is necessary to conjecture that film rupture by strain localization near threshold is not sensitive to frequency, due to reduced average strain rate effects.

The frequency result is unique to the Al-Li alloy. Based on modeling and data for 2000 and 7000 series alloys in water vapor, Wei and coworkers argue for fast surface reaction kinetics which leads to da/dN independent of frequency and at a level which is governed by "saturation" surface reaction and hydrogen production

(13,19). (Low frequency crack growth rates in 7000 series alloys may increase with decreasing frequency due to intervention of a slow surface reaction step.) Crack growth rates for aqueous chloride conditions increased with decreasing frequency for 7017, 7075 and 2618 alloys; for example a factor of 250 decrease in frequency resulted in 7-fold, 3-fold and 2-fold increases respectively in da/dN at ΔK=15 MPa$\cdot m^{1/2}$ (12,14).

Increased and decreased crack growth rates with anodic and cathodic polarization, respectively, could correspond to changes in the formation of crack tip surface films. Reduced da/dN and the formation of a black surface film by cathodic polarization is evidence of a protective crack tip surface film, possibly hydroxide based. (Under cathodic conditions, excess hydroxide ions are present within the crack to react with aluminum and lithium to form surface $Al(OH)_3$+LiOH, resulting in a black surface film. A similar black surface film has been observed on the fracture surfaces of alloy 2090 specimens fatigued in pure oxygen, followed by exposure to moist air (4). The reaction for LiOH formation during water vapor exposure is $Li_2O+H_2O=2LiOH$ (22)). The formation of a surface film may limit hydrogen production by inhibiting the metal/water reduction reaction, resulting in reduced hydrogen entry. The reduced cathodic effect on da/dN with increased ΔK is consistant with mechanical film rupture by intensified slip. Hydrogen production and entry are enhanced by increasing the area of reactive surface along slip steps. Increased da/dN is also observed for anodic potential, an environment that favors a less protective crack tip surface film.

Reduced transgranular corrosion fatigue crack growth with the addition of Li_2CO_3 is possibly due to the formation of a passive film; a result consistent with decreased da/dN associated with a cathodically formed surface film. Li_2CO_3 is thought to form a passive film on Al-Li alloys which increases the susceptibility for intergranular stress corrosion cracking in aqueous NaCl (23). The mechanism is unclear; Li^{+1} passivates aluminum (24), and CO_3^{-2} affects surface film stability (23).

The beneficial effect of a surface film is likely to be chemical in origin. Film or corrosion product induced crack closure is not operative because the environmental influences are observed at stress ratios above 0.85 and for short crack wakes. Secondly, there is no evidence that surface films promote irreversible dislocation damage (4). Rather, we speculate that films interfere with crack tip environmental reactions (hydrogen production or dissolution), resulting in a reduction in fatigue crack growth rate. Once damaged by chemical or mechanical means, such as localized anodic pitting dissolution or slip step formation, the film no longer acts as a barrier; the alloy is rendered susceptible to brittle crack growth.

Although experimental evidence strongly suggests that surface films play a primary role in retarding crack tip damage during transgranular fatigue of alloy 2090 in aqueous environments, further work must be performed to understand the roles of hydrogen and transient localized anodic dissolution. Gaseous environment corrosion fatigue experiments and high resolution fractographic analyses are being conducted in this regard (4).

CONCLUSIONS

The high resolution electrical potential difference technique, short crack specimen geometry and constant ΔK-step changed R/constant K_{max} approach successfully characterizes intrinsic fatigue crack growth in complex aluminum-lithium based alloys exposed to aggressive aqueous environments.

Al-Li-Cu alloy 2090, peak aged, is susceptible to corrosion fatigue crack propagation in aqueous 1% NaCl under anodic polarization. At low ΔK/high R, near threshold crack growth rates are significantly increased, with growth occurring by a crystallographic cleavage process. High ΔK/low R growth rates are increased by the aqueous NaCl environment, with highly deflected slip band cracking and sub-grain boundary fracture the

dominant microscopic modes. Environmental effects on alloy 2090 are less severe than those observed for high strength alloy 7075; the new aluminum lithium alloy behaves similarly to conventional 2000 series alloys.

Crack tip films play an important role in corrosion fatigue damage, as evidenced by: 1) increased da/dN with increased cyclic frequency, particularly at high ΔK, 2) retarded crack growth due to cathodic polarization in NaCl and 3) reduced da/dN due to Li_2CO_3 additions. Film formation hinders the hydrogen embrittlement process which is presumed to control environmental crack propagation.

ACKNOWLEDGEMENT

The research support provided by the NASA-Langley Research Center, grant NAG-1-745 with D.L. Dicus as monitor, is gratefully acknowledged. Alloy 2090 was provided by the Alcoa Technical Center and E.L. Colvin.

REFERENCES

1. K.T. Venkateswara Rao, W. Yu and R.O. Ritchie, Metall. Trans. A, Vol. 19A, pp. 549-561 and pp. 563-569 (1988).

2. R.S. Piascik and R.P. Gangloff, "Environment Assisted Degradation Mechanisms in Al-Li Alloys", Report No. UVA/528266/MS88/101, University of Virginia, Charlottesville, VA (1988).

3. ASTM G5-82,"Standard Reference Method for Making Potentiostatic and Potentiodynamic Anodic Polarization Measurements", 1985 Annual Book of ASTM Standards-Methods and Analytical Procedure, ASTM, Philadelphia, PA, Vol. 3, pp. 123-133 (1985).

4. R.S. Piascik and R.P. Gangloff, "Intrinsic Fatigue Crack Propagation in Aluminum-Lithium Alloys: The Effect Of Gaseous Environments", Proceedings of ICF-7, K. Salema, ed., Pergammon Press, London, in press (1988).

5. H. Tada, P. Paris and G.I. Irwin, The Stress Analysis of Cracks Handbook, Del Research Corp., St. Louis, MO, pp. 2.10-2.11 (1985).

6. R.P. Gangloff, Advances in Crack Length Measurements, C.J. Beevers, ed., EMAS, UK, pp. 175-229 (1982).

7. ASTM E647-88, "Standard Test Method for Measurement of Fatigue Crack Growth Rates", Annual Book of ASTM Standards, ASTM, Philadelphia, PA, Vol. 03.01, (1988).

8. W.A. Herman, R.W. Hertzberg, and R. Jaccard,"A Simplified Laboratory Approach for the Prediction of Short Crack Behavior in Engineering Structures", J. Fat. Frac. Engr. Matls. and Struc., in press (1988).

9. R.E. Stoltz and R.M. Pelloux, Met. Trans, Vol. 3, pp. 2433-2441 (1972).

10. G. R. Yoder, P.S. Pao, M.A. Imam and L.A. Cooley, Intl. SAMPE Metals Conf. Ser., Vol.1, pp. 25-36 (1987).

11. R.P. Gangloff, Metall. Trans. A, Vol. 16A, pp.953-969 (1985).

12. H.J.H. Holroyd and D. Hardie, Corr. Sci., Vol.23, No.6, pp. 527-546 (1983).

13. M.Gao, P.S. Pao and R.P. Wei, Metall. Trans. A, Vol. 19A, pp. 1739-1750 (1988).

14. D. Aliaga and E. Budillion, "Corrosion Fatigue Behavior of Some Aluminum Alloys", AGARD Report No. AGARD-CP-316 (1981).

15. R.P. Gangloff and D.J Duquette, Chemistry and Physics of Fracture, R.M. Latanision and R.H. Jones, eds., NATO Series E, No.130, pp. 612-645 (1987).

16. N.J.H. Holroyd and G.M. Scamans, Environment-Sensitive Fracture, ASTM 821, S.W. Dean, E.N, Pugh and G.W. Ugiansky, eds., ASTM, Philadelphia, PA, pp. 202-241 (1984).

17. R.E. Ricker and D.J. Duquette, "The Use of Electrochemical Potential to Control and Monitor Fatigue of Aluminum Alloys, Paper # 354, Corrosion 85, NACE, Houston, TX, (1985).

18. D.L. Davidson and J. Lankford, Fat. Engr. Matls. and Struc., Vol. 6, pp. 241-256 (1983).

19. R.P. Wei and R.P. Gangloff, "Environmentally Assisted Crack Growth in Structural Alloys: Perspectives and New Directions", in Fracture Mechanics: Perspectives and Directions, ASTM STP, R.P. Wei and R.P. Gangloff, eds., ASTM, Philadelphia, Pa, in press (1988).

20. R.P. Gangloff, "Corrosion Fatigue Crack Propagation", This volume.

21. S.J. Hudak, Jr., D.L. Davidson and R.A. Page, Embrittlement by the Localized Crack Environment, R.P. Gangloff, ed., TMS-AIME, Warrendale, PA, pp. 173-198 (1984).

22. C.E. Messer, The Alkali Metals, Publication No.22, The Chemical Society, Burlington House, London, pp. 183-198 (1967).

23. J.G. Craig, R.C. Newman, M.R. Jarrett and N.J.H. Holroyd, Environmental Degradation of Engineering Materials III, M.R. Louthan, R.P. McNitt and R.D. Sisson, eds. pp. 313-320 (1987).

24. Jing Gui and T.M. Devine, Scripta Met., Vol. 21, pp. 853-857 (1987).

TABLE 1: Alloy 2090 Material Properties

Chemical Composition

Li	Cu	Zr	Fe	Si	Mn
2.14	2.45	0.09	0.05	0.04	0.00
Mg	**Cr**	**Ni**	**Ti**	**Na**	**Zn**
0.00	0.00	0.00	0.01	0.001	0.01

Material Condition

Solutionized, water quenched and stretched.
Peak aged 190°C - 4hrs

Mechanical Properties (Long-Transverse)

Yield	Ultimate
496 MPa	517 MPa

Microstructure

Grain size - 3.3 mm (transverse)
- 0.11 mm (short transverse)
Subgrain size - 15 μm (transverse)
- 5 μm (short transverse)
Precipitates
δ' - Al_3Li, θ' - Al_2Cu, T_1 - Al_2CuLi, T_2 - Al_6CuLi_3,
Matrix phases - δ', T_1, θ'; Subgrain boundary - T_1
High angle grain boundary - T_2

Table 2: Alloy 7075 Material Properties

Chemical Composition

Zn	Mg	Cu	Cr	Zr	Fe
5.74	2.31	1.58	0.20	0.01	0.26
Si	**Mn**	**Ni**	**Ti**	**Na**	**Ca**
0.10	0.05	0.01	0.05	0.000	0.0001

Mechanical Properties (Long-Transverse)

Yield	Ultimate
466 MPa	540 MPa

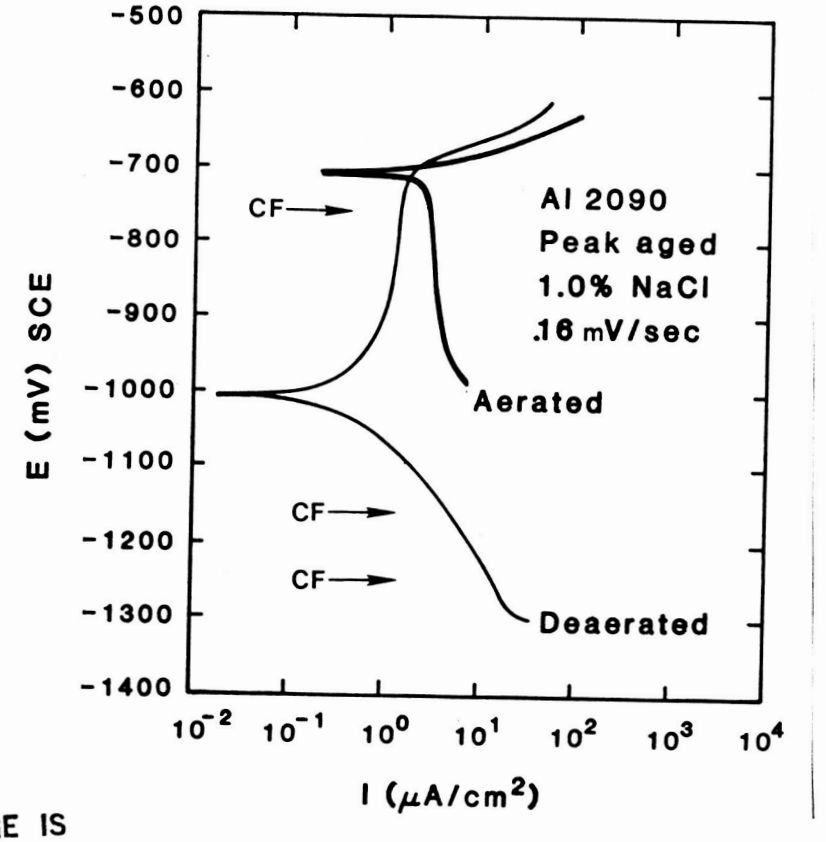

(a)

(b)

Fig.1 (a) Potentiodynamic polarization of alloy 2090 in aerated and deaerated 1% NaCl. (b) Photomicrograph of alloy 2090 exposed to deaerated 1% NaCl for 8 days at -0.760 V (SCE).

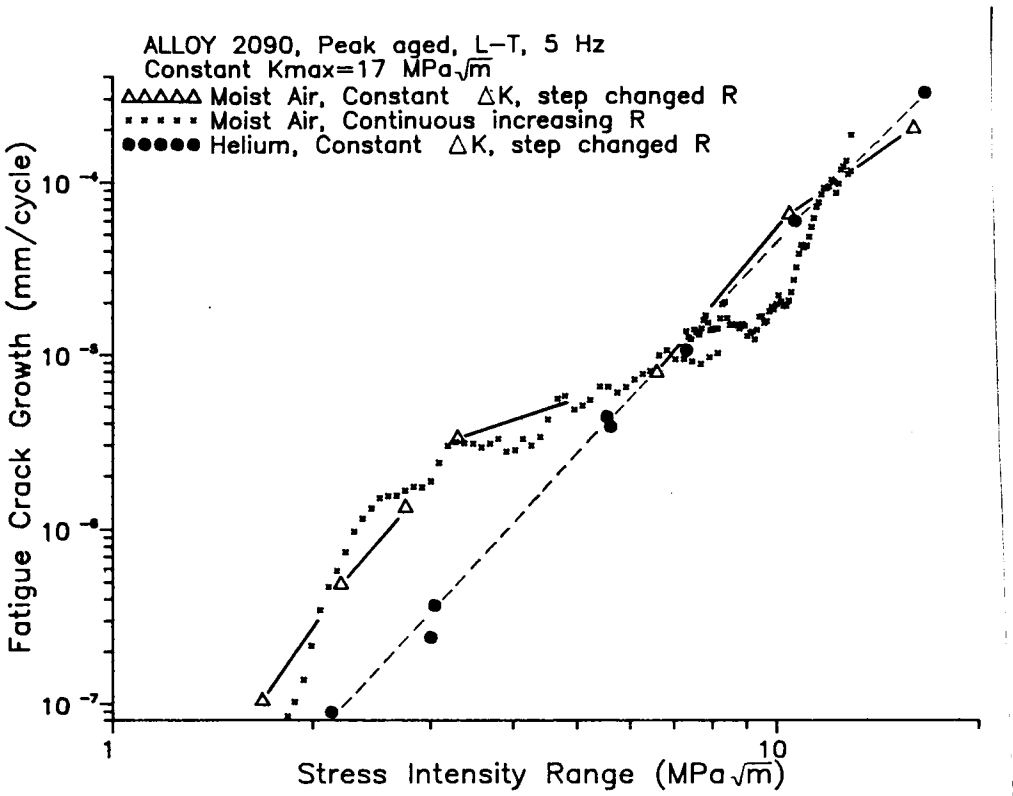

Fig.2 A comparison of constant ΔK-step changed R/constant K_{max} results with decreasing ΔK-constant K_{max} data for moist air and the intrinsic fatigue crack growth behavior of AA 2090 in helium.

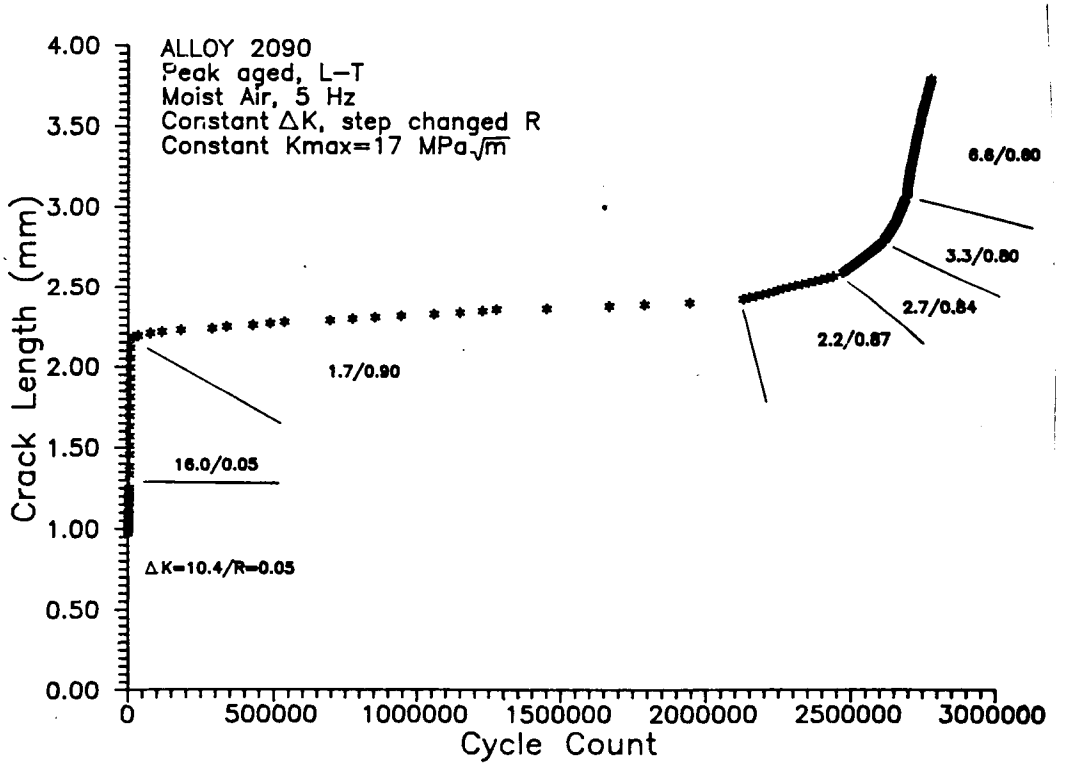

Fig.3 Crack length versus loading cycles data for the constant ΔK-step changed R/constant K_{max} results of Fig. 2, moist air.

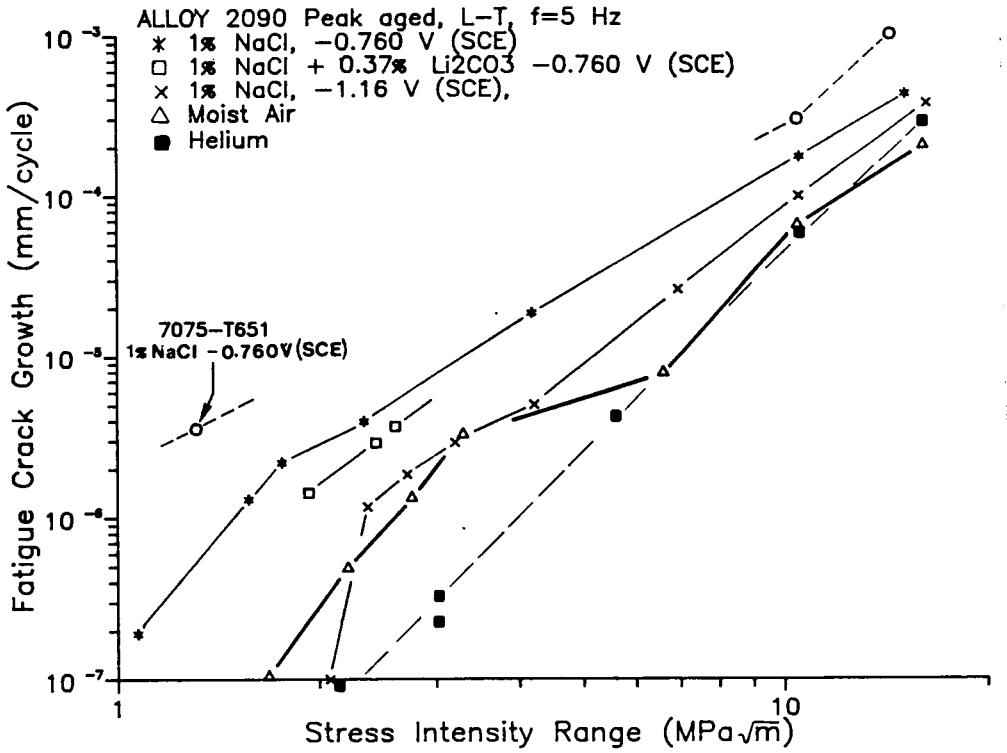

Fig.4 Corrosion fatigue crack growth behavior of alloy 2090 in aqueous 1% NaCl at constant anodic (-0.760 V SCE) and cathodic (-1.160 V SCE) potentials, 1% NaCl+0.37% Li_2CO_3 (-0.760 V SCE), and moist air environments; and of alloy 7075 in aqueous 1% NaCl at constant anodic (-0.760 V SCE) potential.

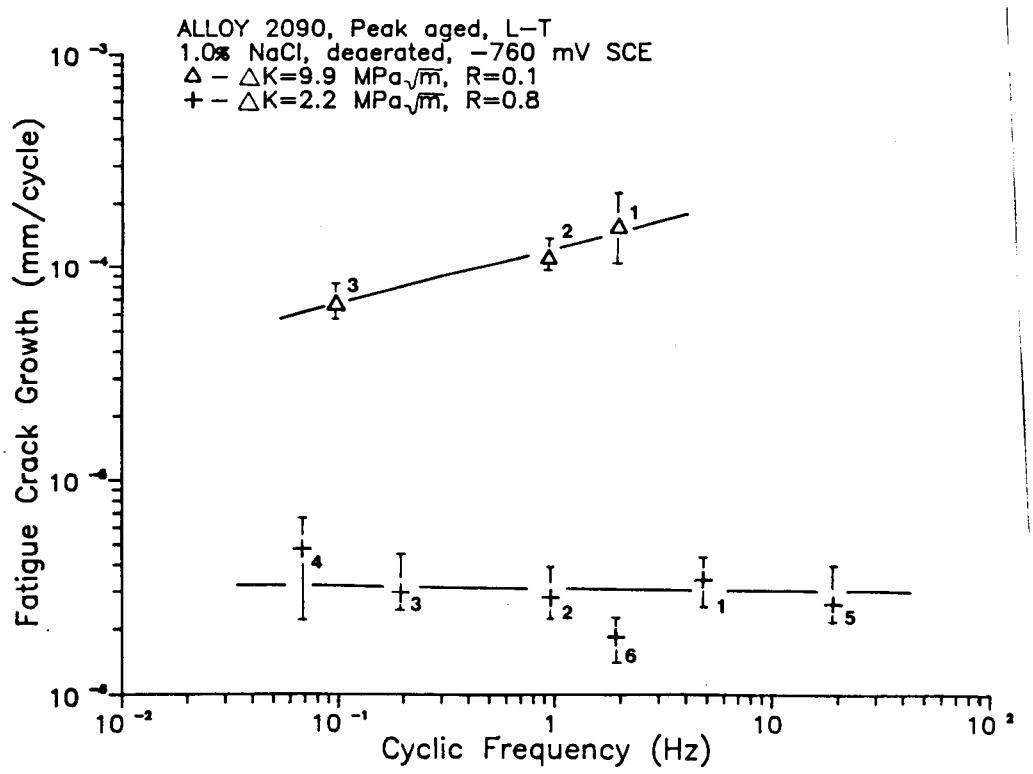

Fig.5 The dependence of corrosion fatigue crack growth rate on cyclic frequency at high and low constant ΔK; alloy 2090 in 1% NaCl with anodic polarization.

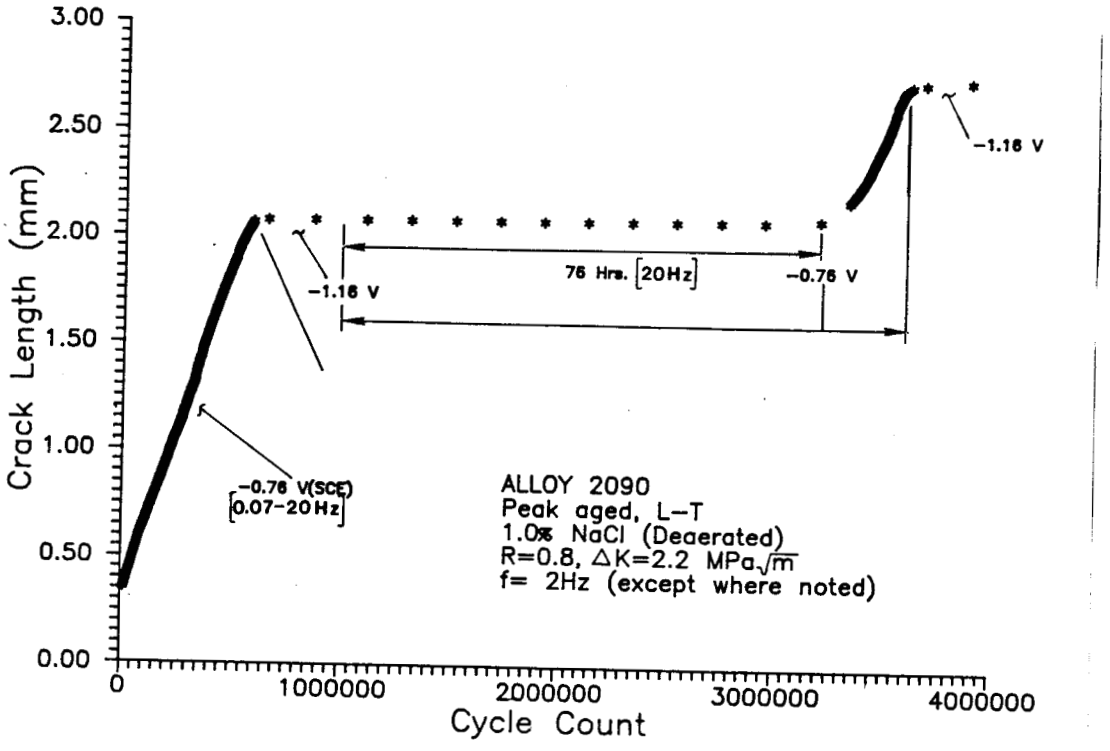

(a)

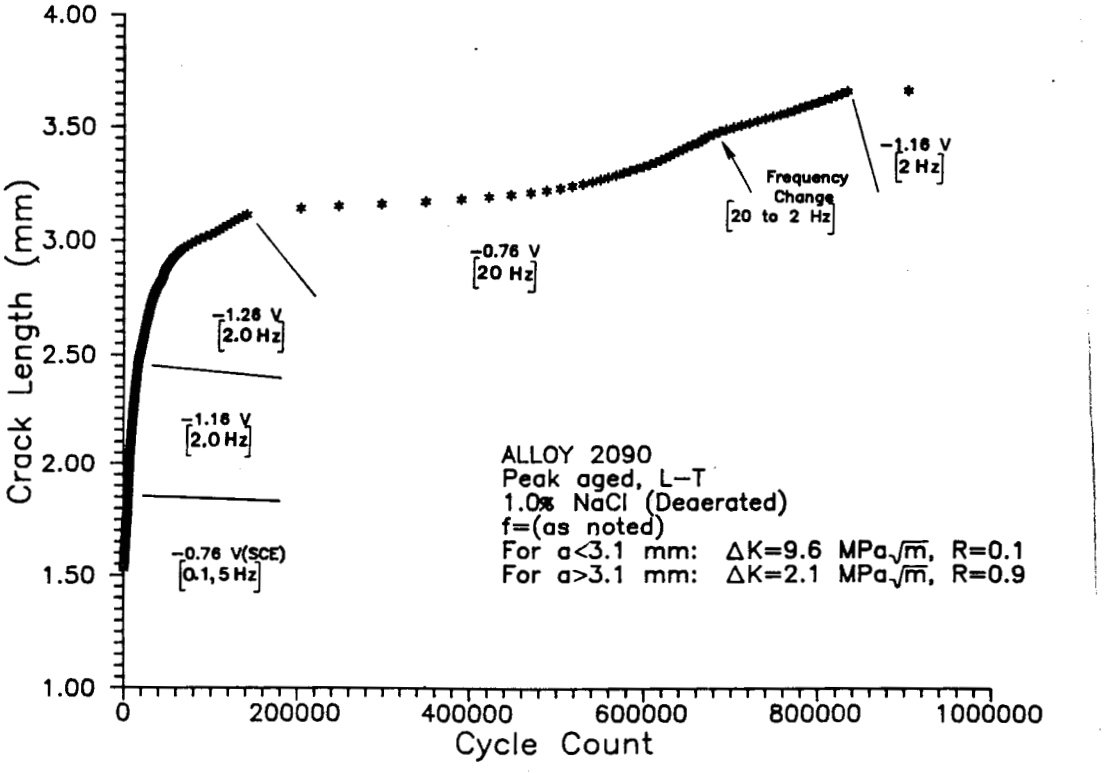

(b)

Fig.6 The effect of cathodic polarization on intrinsic corrosion fatigue crack growth in alloy 2090 1% NaCl at constant ΔK levels of (a) 2.2 MPa·$m^{1/2}$ for high R and (b) 9.6 and 2.1 MPa·$m^{1/2}$ for low and high R conditions, respectively.

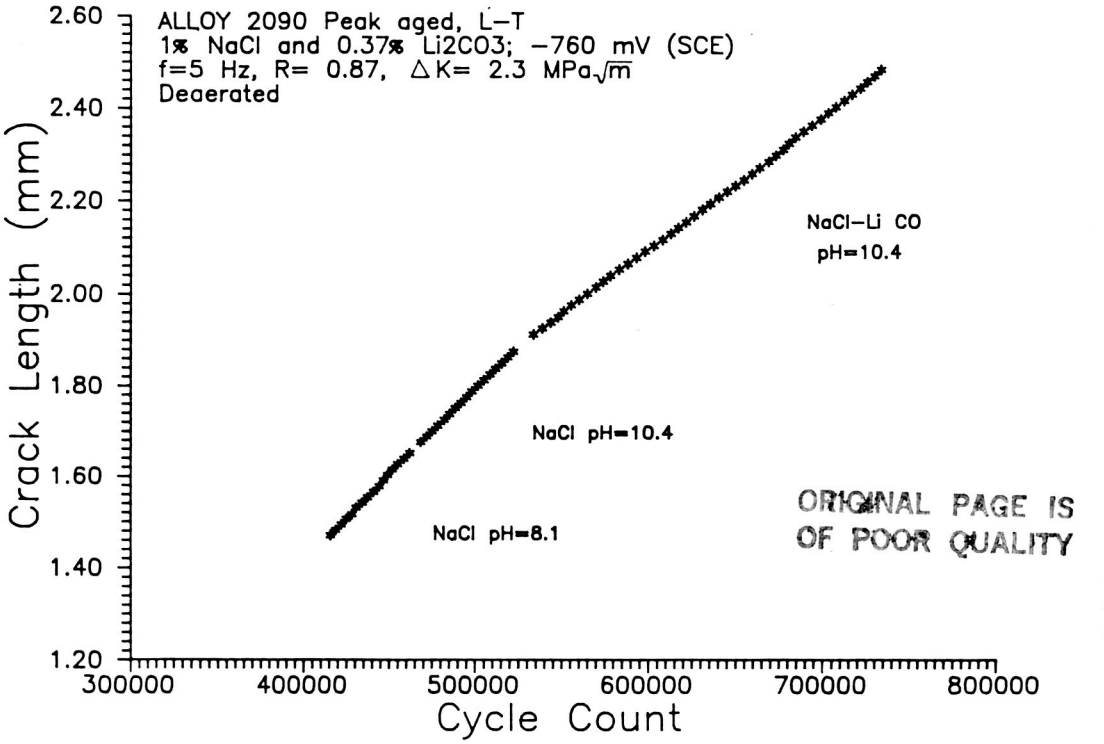

Fig.7 The effect of Li_2CO_3 addition and pH change on intrinsic fatigue crack growth in alloy 2090 exposed to 1% NaCl at constant anodic potential and constant ΔK.

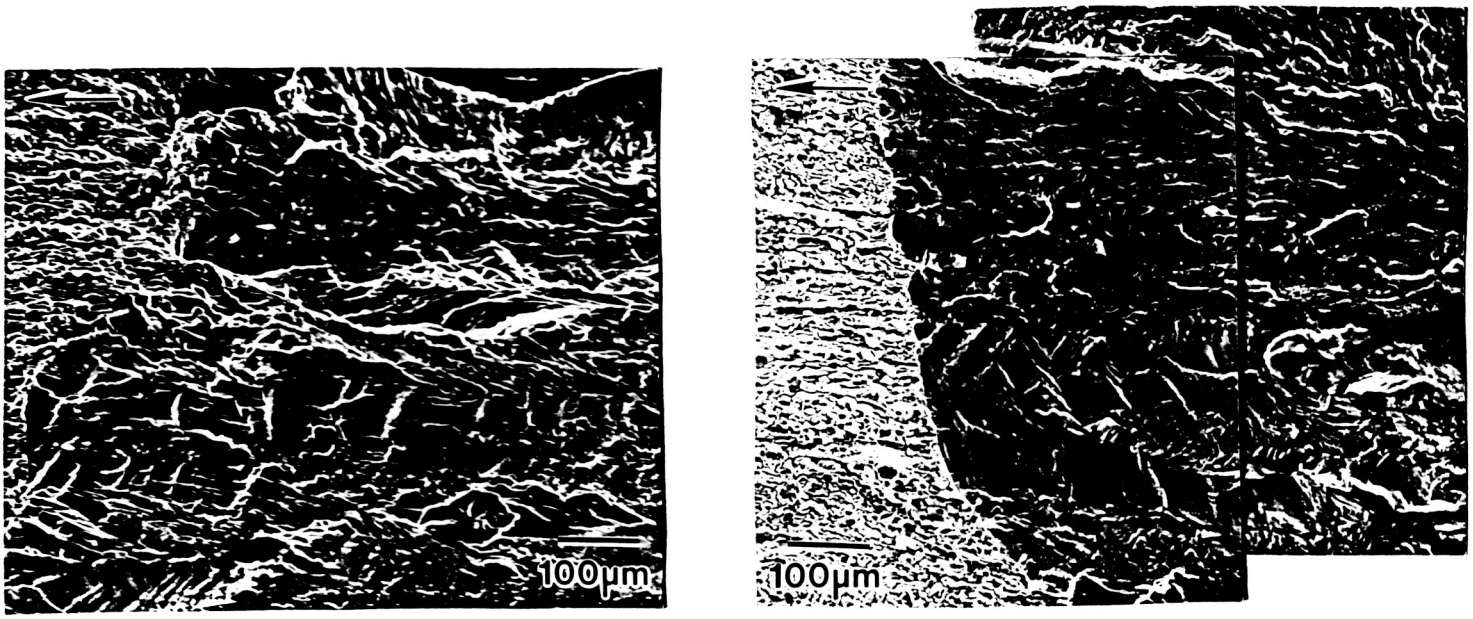

(a) (b)

Fig.8 A comparison of the fracture morphology due to corrosion fatigue at low ΔK in (a) moist air at 2.5 $MPa \cdot m^{1/2}$ and (b) deaerated 1% NaCl (-0.760 V SCE) at 2.2 MPa $m^{1/2}$. Crack growth is from right to left, with the fatigue crack-overload fracture interface shown.

First draft of a paper to be submitted to Corrosion for review; May, 1989

The Hydrolytic Effects of Al(III) and Li(I) in Simulated Crevice Experiments Using 2090, 2024 and 1100 Aluminum

R.G. Buchheit, Jr.
G.E. Stoner

Center for Electrochemical Sciences
and Engineering
Department of Materials Science
University of Virginia
Charlottesville, VA 22901

Introduction: Results from pH versus time measurements made in artificial crevice experiments with 2024-T6 showed that an acidic crevice solution typically developed with time ($3.5 < pH < 4.5$). In similar experiments performed with peak aged 2090, an alkaline crevice solution developed ($8 < pH < 10$).

It is widely believed that crevice solution pH in the range of 3.5 to 4.5 is a result of the hydrolysis of Al^{3+}; although the particular hydrolysis reaction has been debated (1-5). In lithium bearing alloys hydrolysis of Li^{+} is thought to dominate crevice chemistry generating the observed alkaline crevice solution pH (6-8). However, in some cases an acidic crevice solution was observed in experiments using alloy 2090 suggesting that the effects of Li^{+} hydrolysis were mitigated. In 2XXX series alloys where lithium is not present crevice solution pH values as high as 8 have been observed in artificial crevice experiments.

The goal of this study has been to:

1.) establish and isolate the effects of Al^{3+} and Li^{+} hydrolysis in crevice corrosion situations

2.) identify the conditions which favor one or the other of the hydrolytic reactions in question

3.) develop the ability to use hydrolysis equilibria to model the pH versus time response in crevice corrosion situations.

Experimental Approach and Technique: The approach used in this study has been to utilize shavings immersion experiments to monitor the pH versus time response of peak aged 2090, 2024-T6 and 1100 aluminum. A series of experiments have been performed in which 3.5 w/o solution was preadjusted to pH values ranging from 0 to 12 then added to the shavings. Experimental data was then compared to a modeled pH versus time response based on hydrolysis equilibria calculations.

Using this technique, a high surface area to solution volume ratio simulated an important aspect of crevice geometries. Deaeration of the test cell minimized the contribution of O_2 reduction to cathodic activity thereby simulating another aspect of the crevice corrosion process and simplifying the model calculations. Further, the pH response was not affected by chloride ion accumulation since the cell was a closed system. Figure 1 is a schematic illustration showing the cell setup and a listing of the important parameters for these experiments.

Results: Figures 2a and 2b are stability diagrams for the hydrolysis products of Li^+ and Al^{3+} respectively. These diagrams show the relative concentrations of monomeric hydrolysis products as a function of pH. The diagrams were generated by simultaneously solving a system of equations representing the pertinent hydrolysis equilibria. Monomeric species equilibria

were selected because the products of these reactions form quickly and reversibly hence are believed to dominate the hydrolytic activity in short term experiments.

Monovalent lithium is only slightly hydrolyzed and has just one hydrolysis product, namely LiOH, which is in equilibrium with solvated Li^+ at a pH of nearly 14. Aluminum (III) has four monomeric hydrolysis products and multiple equivalence points exist in the range of pH 4 to 8. The hydrolysis equilibrium equations and constants used to generate these diagrams are listed in Table 1.

Figure 3a is a summary of the pH versus time response for peak aged 2090 shavings. The initial solution pH values are indicated on the right hand side of the diagram. These data indicate that there are three characteristic types of response for 2090. The first characteristic response occurs for initial pH values ranging from 0 to 2. At this low pH there is no passive film stability and dissolution of the precipitate phases and matrix phase both occur at appreciable rates. Since there is much more matrix phase that precipitate phase Al^{3+} is likely to be more prevalent in solution than Li^+. Hence Al (III) hydrolysis dominates the solution chemistry. The second characteristic response occurs for initial pH values ranging from 3 to 10. In this regime a passive film exists over the aluminum matrix but does not exist over lithium rich precipitate phases. The precipitate phases dissolve and the lithium ion concentration in solution supersedes that of aluminum ion. As a result Li^+ hydrolysis dominates solution chemistry and an alkaline pH is developed. In experiments where the initial pH was above 11, the

high hydroxyl ion concentration dominated the crevice pH response.

Figure 3b is a summary of the pH versus time response for 2024-T6. Again, three different characteristic types of pH response were observed. The response when initial pH values were in the range of 0 to 2 was similar to that in the case of peak aged 2090; a high aluminum dissolution rate allowed Al(III) hydrolysis to dominate the crevice chemistry. When the initial solution pH was in the range of 3 to 8, the steady state pH was measured to be in the range of 4 to 8 where the Al(III) monomeric hydrolysis product equivalence points exist. When the initial pH was greater than 9, the pH response was dominated by the large hydroxyl ion concentration.

The pH versus time response observed for shavings experiments in 1100 Al was quite similar to that observed for the 2024 shavings. This suggested that the same types of processes were influencing the crevice pH for the same initial solution pH values.

Figure 4 shows an algorithm for calculating the pH versus time response based on hydrolysis equilibria. The inputs for the calculation are the alloy composition, temper, surface area and initial solution pH. The temper input accounts for the relative volume fractions of precipitate and matrix phases. Based on the initial pH, an appropriate corrosion rate (current density) can be chosen. Presently, only two choices are available. The first is a corrosion rate representing corrosion through a passive film (i.e. $4 < pH < 10$) while the second is a corrosion rate

representative of the rapid dissolution in highly acidic or basic solutions. From these inputs a cation production rate for each of the species of interest can be determined. From the cation production rate, the change in metal ion concentration in solution over a small time interval can be calculated. This change in metal ion concentration is treated as a disturbing force on an equilibrium condition. Le Chatelier's Principle is then applied to hydrolysis equilibrium expressions and the resulting pH change for the time interval is determined. In this way, a modeled pH versus time response can be generated.

Figure 5 shows two calculated pH versus time curve, one based on Al(III) hydrolysis and the other on Li(I) hydrolysis. These modeled responses are superimposed on the data summary for peak aged 2090. The solid line in the low pH region is for Al(III) hydrolysis while the line in the high pH region is for Li(I) hydrolysis.

Presently, these calculations can not account for competing hydrolysis equilibria, i.e. Li(I) hydrolysis which forces pH in the alkaline directionand Al(III) hydrolysis which forces pH in the acidic direction. Incorporation of corrosion rate data in the analysis for important precipitate phases like T_1 and the matrix phase in 2090 as a function of pH should facilitate calculation of the modeled response for competitive situations.

Summary:

1.) Acid-base reactions can play an important role in crevice corrosion. The effect of these reactions on solution pH can be treated mathematically for modeling purposes.

2.) The effects of hydrolysis of Li(I) and Al(III) on solution pH can be distinguished from one another both experimentally and theoretically.

3.) Results from shavings experiments indicate that initial solution pH can favor one type of hydrolytic reaction over another resulting in quite different crevice solution pH values. In the case of peak aged 2090, Li(I) hydrolysis dominates crevice pH response when aluminum rich matrix dissolution is suppressed by the presence of a passive film.

REFERENCES

1. K. Sotoudeh, T.H. Nguyen, R.T. Foley, B.F. Brown, Corrosion, 37, 1981, pp. 358-362.

2. L.P. Holmes, D.L. Cole, E.M. Eyring, J. Phys. Chem., 72, 1968, pp. 301-304.

3. C.P. Frink, M. Peach, Inorg. Chem., 2, 1963, pp. 473-478.

4. D.W. Siitari, R.C. Alkire, J. Electrochem. Soc., 129, 1982, pp. 481-487.

5. R.C. Alkire, D.W. Siitari, J. Electrochem.Soc., 129, 1982, pp. 488-496.

6. J.G. Craig, R.C. Newman, M.R. Jarrett, N.J.H. Holroyd, Journal de Physique, 48, Sept., 1987, pp. 825-833.

7. J.G. Craig, R.C. Newman, "Local Chemistry of Stress Corrosion Cracking in Al-Li-Cu-Mg Alloys", Conf. Proc. 4th Int. Aluminum-Lithium Conference, Les Editions de Physique, Paris, 1987, pp. 853-864.

8. N.J.H. Holroyd, A. Gray, G.M. Scamans, R. Hermann, "Environment Sensitive Fracture of Al-Li-Cu-Mg Alloys", Conf. Proc. 3rd Int. Aluminum-Lithium Conference, Institute of Metals, London, 1986. pp. 310-320.

Table 1. Equations and Constants Used to Generate Li(I) and Al(III) Stability Diagrams.

The reactions considered are of the general form:

$$M^{z+} + nH_2O == M(OH)_n^{(z-n)} + nH^+$$

The equilibrium expressions are written in terms of the acid hydrolysis:

$$K_a = \frac{[M(OH)_n^{(z-n)}][H^+]^n}{[M^{z+}]}$$

For Li(I):

$$Li^+ + H_2O == LiOH + H^+ \qquad K_a = 1.513 \times 10^{-14}$$

For Al(III):

$$Al^{3+} + H_2O == AlOH^{2+} + H^+ \qquad K_a = 1.07 \times 10^{-5}$$

$$Al^{3+} + 2H_2O == Al(OH)_2^+ + 2H^+ \qquad K_a = 5.01 \times 10^{-10}$$

$$Al^{3+} + 3H_2O == Al(OH)_3 + 3H^+ \qquad K_a = 1 \times 10^{-15}$$

$$Al^{3+} + 4H_2O == Al(OH)_4^- + 4H^+ \qquad K_a = 1 \times 10^{-23}$$

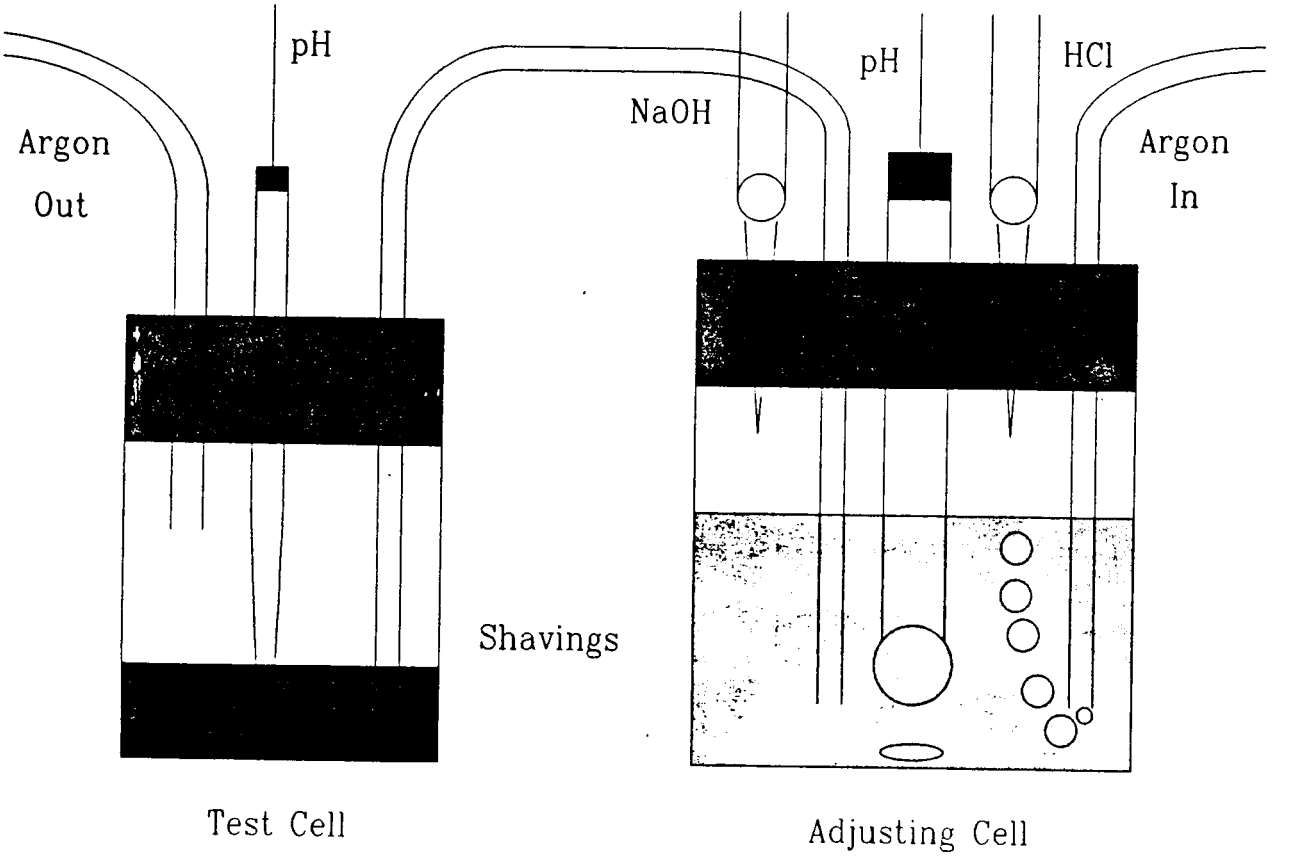

Figure 1. Schematic illustration of the experimental setup used to perform shavings experiments.

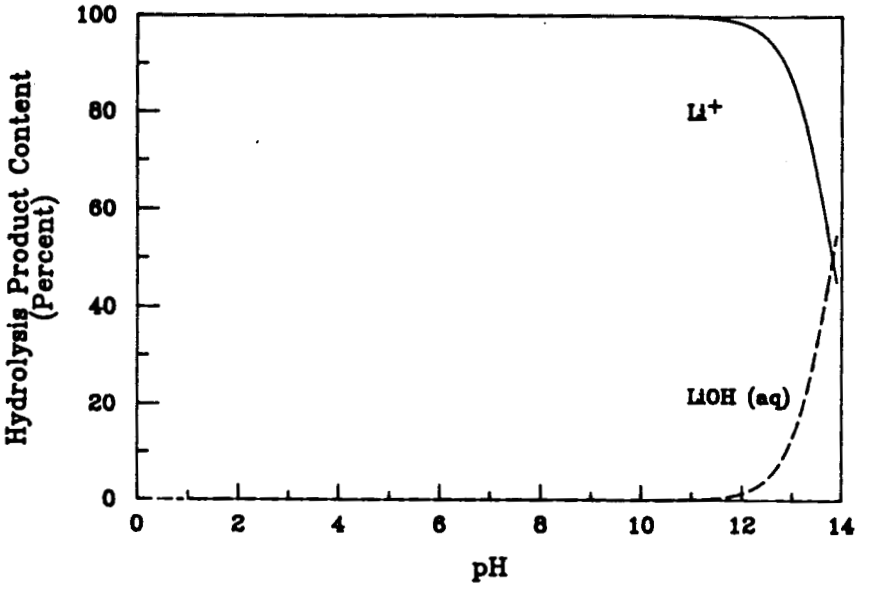

Figure 2a. Stability diagram for Li (I) hydrolysis products.

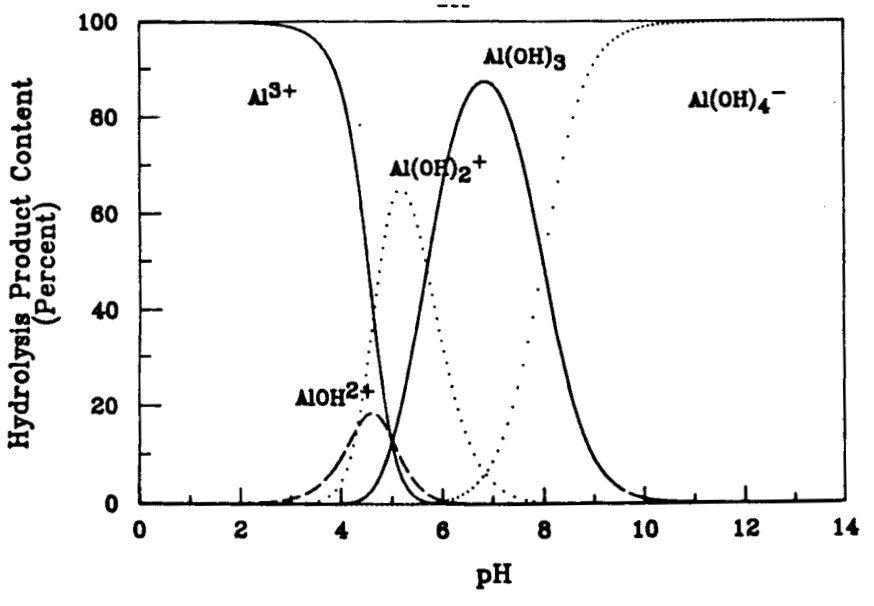

Figure 2b. Stability diagram for the Al(III) monomeric hydrolysis products.

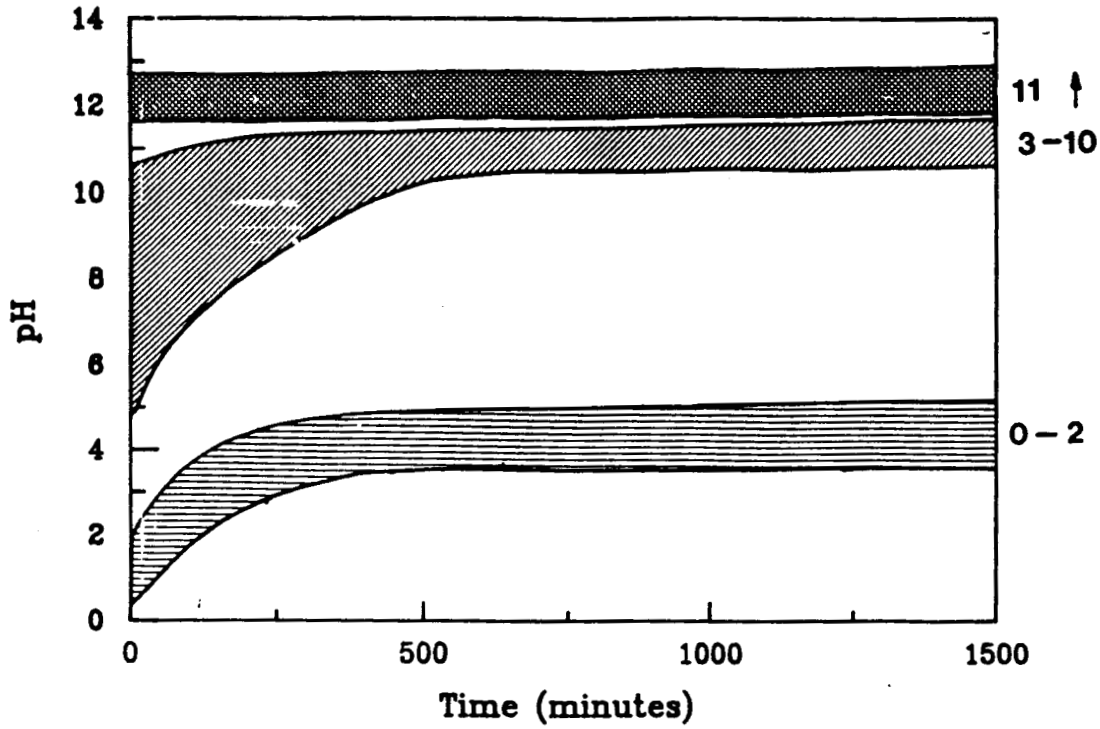

Figure 3a. pH versus time data summary for peak aged 2090 shavings.

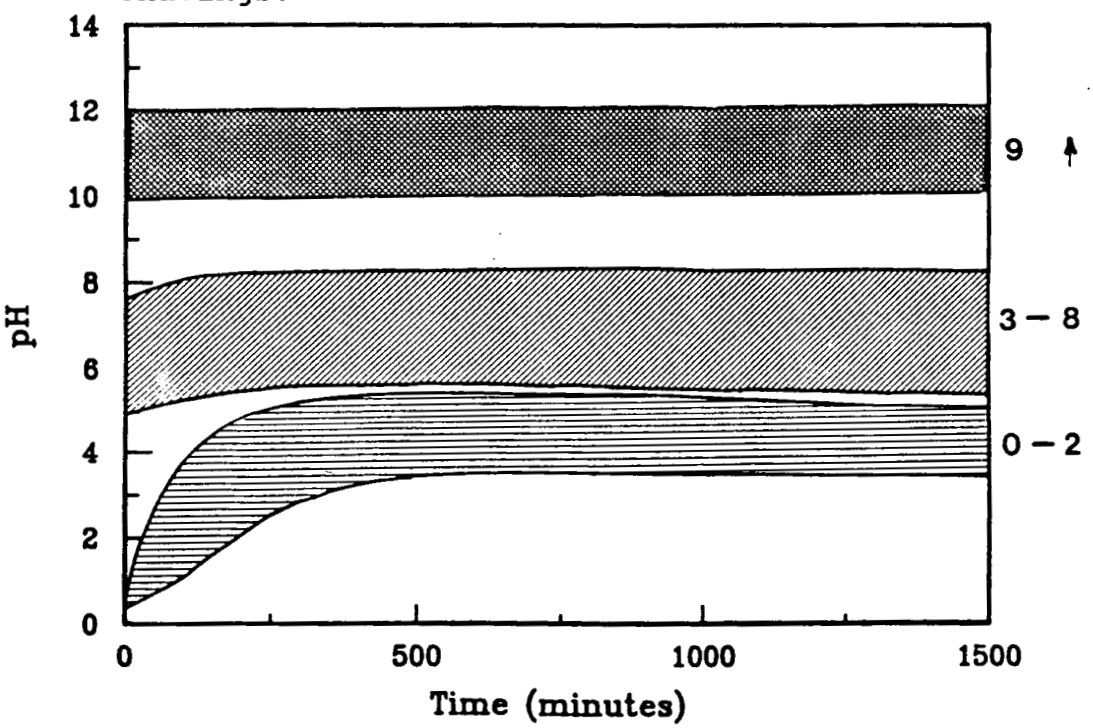

Figure 3b. pH versus time data summary for 2024-T6 shavings.

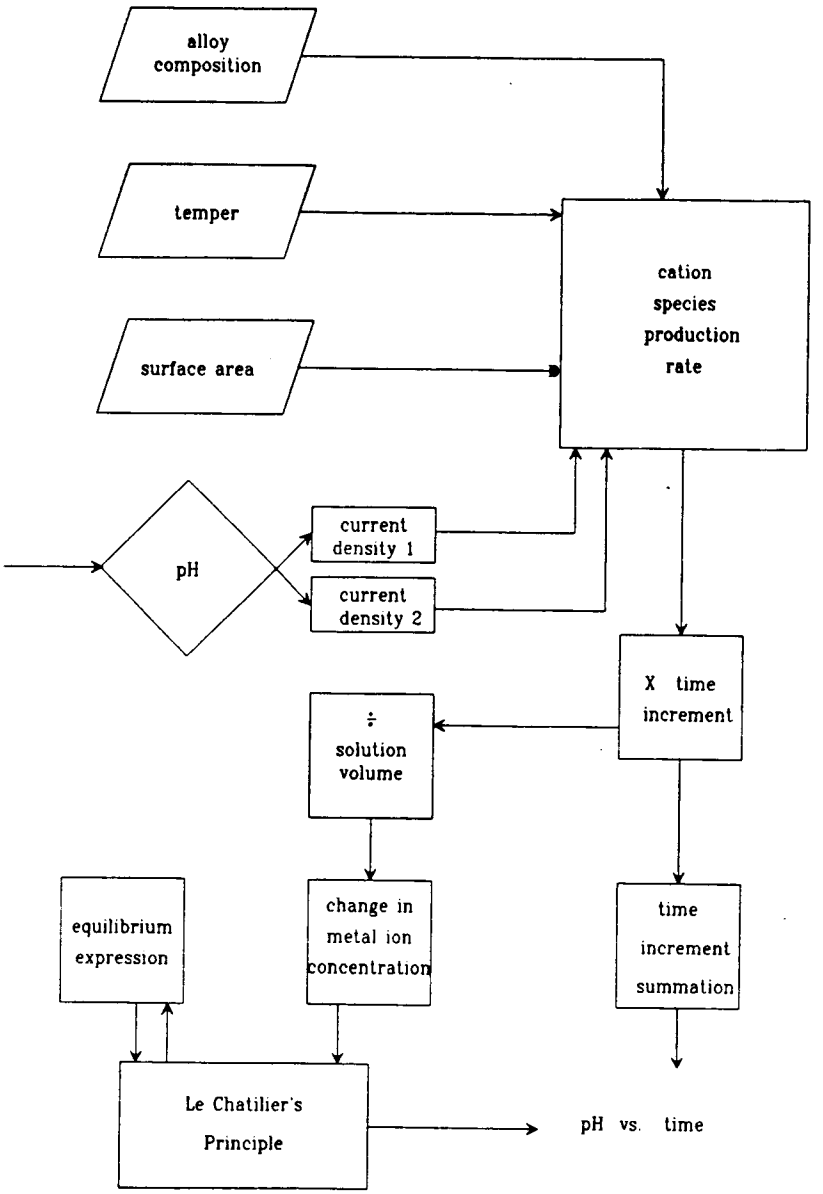

Figure 4. Algorithm for the calculation of the pH versus time response based on hydrolysis.

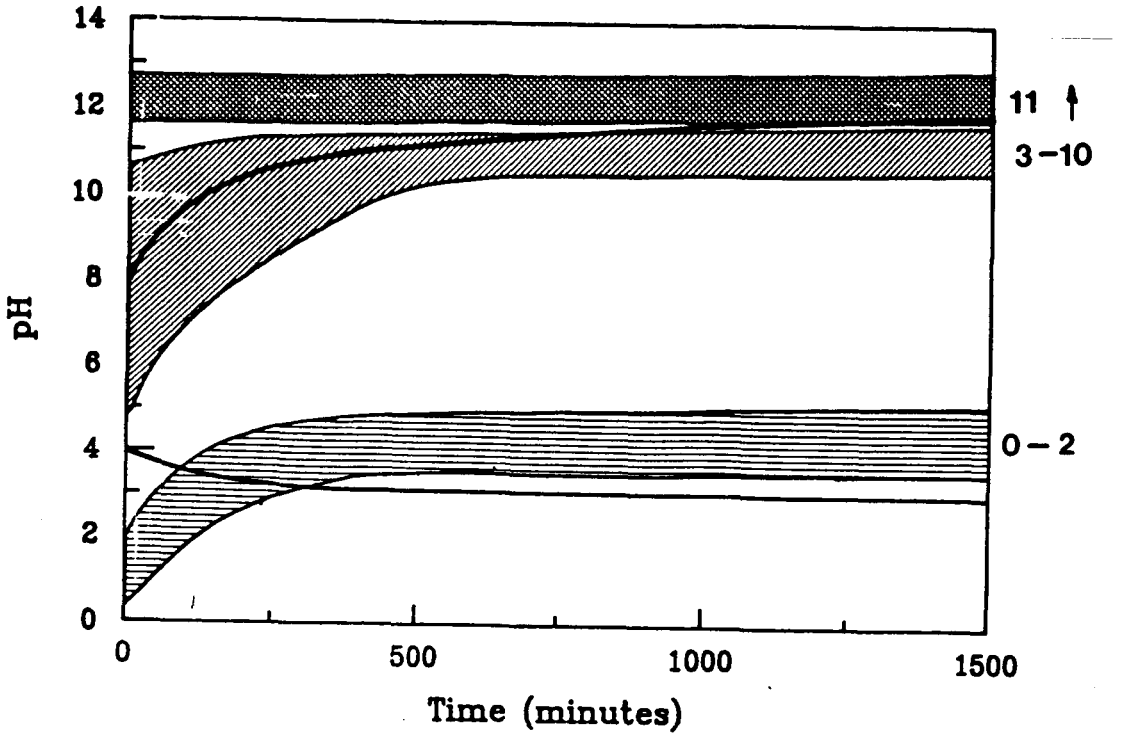

Figure 5. Predicted pH versus time response superimposed on the peak aged 2090 shavings data summary plot.

To be submitted to Corrosion for review; Jan, 1989

AN INVESTIGATION OF THE LOCALIZED CORROSION BEHAVIOR OF ALLOY 2090

R.G. Buchheit, Jr.[1], J.P. Moran[1], G.E. Stoner[1] and K.A. Coyne[2]

[1] Center for Electrochemical Sciences
and Engineering
Department of Materials Science
The University of Virginia
Charlottesville, VA 22901

[2] Newport News Shipbuilding and Dry Dock Company
4101 Washington Avenue
Newport News, VA 23607

ABSTRACT

The pitting and intergranular corrosion behavior of alloy AA2090 (Al-2Li-3Cu) in a 3.5 w/o NaCl solution was investigated. Techniques utilized included potentiodynamic polarization, galvanic couples and pH measurements in simulated crevices. Polarization scans were performed on under aged and peak aged material to obtain the standard polarization parameters. Corroded specimens were examined with optical microscopy, scanning electron microscopy (SEM) and energy dispersive X-ray spectroscopy (EDAX) to distinguish various local corrosion morphologies. Ingots were cast to approximate the subgrain boundary, T_1 (Al_2CuLi) phase, and Al-Cu-Fe constituent phases inherent in the alloy. These were then galvanically coupled to solution heat treated (SHT) 2090 to identify their role in local corrosion processes. Simulated crevices were produced by inserting pH micro-electrodes into crevices machined in 2090 blocks to measure pH versus time response in occluded

environments.

Based on the experiments listed above, two different types of pitting mechanisms were identified. The first type was directly attributed to the dissolution of the subgrain boundary phase T_1. A direct correlation between increased subgrain boundary precipitation and increased subgrain boundary pitting was observed. The second type of pitting involved enhanced local galvanic attack of the matrix material surrounding Al-Cu-Fe constituent particles found in this plate. With this type of attack, large pits formed around constituents which occurred randomly throughout the plate.

Associated with constituent particle pitting was a form of localized attack which was designated as continuous subgrain boundary dissolution. This form of corrosion was observed on all specimens used in corrosion experiments. It was only seen, however, in regions adjacent to the largest pits on the specimen, suggesting the influence of an occluded (crevice) environment. Simulated crevice experiments revealed that an acidic crevice solution developed with time. A mechanism by which continuous subgrain boundary dissolution can occur is proposed.

INTRODUCTION

Aluminum-lithium-X alloys are susceptible to localized corrosion in chloride containing aqueous environments. Localized corrosion manifests itself as stress corrosion cracking, crevice corrosion and pitting. All three forms of

environmental attack have been observed in these alloys and microstructural heterogeneity is often implicated as a contributing factor (1-6).

An emergent class of Al-Li-Cu alloys are being studied as possible substitutes for the more conventional 2XXX and 7XXX series alloys, particularly in applications where weight savings are a premium. It is well known that additions of lithium to aluminum reduce density while increasing modulus (7). Although prototype Al-Li-X alloys suffered from unacceptably low ductility and fracture toughness, the commercially produced 2090 (Al-Li-Cu) can achieve acceptable mechanical properties when correctly processed. The mechanical and physical properties of the Al-Li-X system have been well documented (7-18); however, a brief review of the physical metallurgy of alloy 2090, with emphasis on those features pertinent to the present study, is appropriate here. The following discussion is schematically summarized in Figure 1.

The primary matrix phases are δ' (Al_3Li), θ' (Al_2Cu) and T_1 (Al_2CuLi). Coherent δ' is observed as discrete particles and as a coating on the broad faces of θ' (8,10). The partially coherent T_1 and θ' precipitate heterogeneously along dislocations within the matrix or at G.P. Zones (11-13), and are primarily responsible for improved ductility, relative to the binary alloy. Both phases enhance cross-slip, helping to combat the localized deformation due to shearing of δ' (13-15). T_1 is also the primary phase observed along low angle (or subgrain) boundaries (8,12,13,16). Although the crystallographic nature and exact

composition of the high angle (or grain) boundary phase(s) is somewhat controversial (12,16,18), the issue is sufficiently clear from a corrosion standpoint. The primary grain boundary phase is (or closely resembles) the non-coherent T_2 (Al_6CuLi_3). The binary equilibrium phase, δ (AlLi), is not observed at typical aging temperatures (13,17).

The relative concentrations of these phases is dependent upon aging time. The metastable δ' nucleates immediately upon quenching, and reaches a maximum volume fraction well before the peak aged condition (8). Subgrain boundaries are the initial site for T_1 nucleation. Alloys subjected to deformation prior to aging have a higher percentage of T_1 precipitation occurring within the grains due to an increase in dislocation density there (6,19). Matrix nucleation becomes important at longer aging times. Both T_1 and the grain boundary T_2 are equilibrium phases, and they grow throughout the aging process at the expense of δ' (8,12). This results in δ' precipitate free zone forming along both low and high angle boundaries (9,12,16).

Lithium is known to be an exceptionally reactive substance. Its addition to aluminum as an alloying element has generated a great deal of interest regarding its effect on corrosion behavior. As a result, the Al-Li-X corrosion behavior literature base continues to grow (1-4,6). Niskanen (1) was perhaps the first to conduct a broad study of the corrosion behavior of Al-Li alloys. His results for Al-Li binaries showed an increase in corrosion susceptibility with increasing volume fraction of δ (AlLi). In more complex alloys, δ is either accompanied by other

equilibrium phases or not present at all. Corrosion resistance of these alloys is improved and its dependence upon aging is reduced. Several studies conducted on Al-Li-Cu ternary alloys (1-4,6) have shown that surface damage due to localized corrosion increases as aging time increases. This is reported to be a result of continued precipitation of T_1 and T_2. The type of localized attack (i.e., pitting vs. intergranular corrosion) has been found to be dependent on the precipitation morphology, in particular the presence of lithium and copper poor precipitate free zones (PFZ s) along grain boundaries (4,6).

In the present study, two different types of localized attack are distinguished by microstructural observations of corroded surfaces. Two different mechanisms for localized attack are proposed to account for the differences in attack morphology. The roles of T_1 and constituent phases in the mechanisms of pitting and intergranular attack are also addressed.

EXPERIMENTAL PROCEDURE

MATERIALS PREPARATION

The 2090 alloy used for this study was a commercially prepared 38 mm ingot-cast plate, supplied by the ALCOA Technical Center, Pittsburgh, PA. The plate was solution heat treated and subjected to 6% deformation prior to shipping. Further aging was conducted in an air furnace at 160^{o} C. Tempers utilized in this study included solution heat treated (SHT), under aged (UA) and peak aged (PA) conditions. Alloy composition, grain/subgrain

sizes and aging times are summarized in Table 1. All electrochemical testing was performed on the plane perpendicular to the transverse direction. Surface preparation included grinding with successively finer grades of SiC paper, down to 4000 grit, followed by polishing with a 1 μm alumina/distilled water slurry.

T_1 SYNTHESIS

The T_1 phase (Al_2CuLi) was prepared from 99.99 Al, 99.9 Cu and 99.9 Li stock. Stoichiometric amounts of the components were cast under argon in an induction furnace. The resulting ingot was homogenized in a salt bath at 160^{o} C for 24 hours. The ingot was allowed to air cool after homogenization. X-ray diffraction confirmed that the ingot was primarily T_1 and T_2 (see Table 2 for diffraction data summary).

Large plates 3 to 4 cm in length were revealed upon sectioning the ingot. Large voids were contained between intersecting plates. The ingot fractured along the broad plate faces in compression. These broad faces were mounted in epoxy and polished so that the T_1 plate was fully exposed. Specimens prepared in this fashion were then used in corrosion experiments.

CONSTITUENT PHASE SYNTHESIS

EDAX was used to analyze the composition of 25 constituent particles in a specimen prepared from a 2090 plate. Compositional analysis showed that these constituents were comprised mainly of aluminum, copper and iron. Occasionally

small amounts of vanadium, cobalt or titanium were identified.

Based on these results, three alloy compositions were selected to represent the range of measured constituent compositions. Two ternary alloys, Al-24Cu-5Fe and Al-18Cu-5Fe and one binary Al-14Cu alloy were cast.

Alloys were made from 99.99 Al, 99.9 Cu and 99.9 Fe stock. The alloys were cast then homogenized at 525° C in an air furnace. After homogenization the alloys were cold water quenched. The compositions were verified using EDAX. Figure 2 summarizes the compositional information on both the inherent constituents and the representative castings.

ANODIC POLARIZATION

Potentiodynamic polarization experiments were performed on all tempers (SHT, UA, PA), in 3.5 w/o NaCl solution deaerated with argon. Tests were conducted in a plexiglass cell (300 ml volume), using a Pt counter electrode and a saturated calomel (SCE) reference. The flat, polished specimen (working electrode) was exposed to the solution through a 1 cm^2 round hole machined in the end plate of the cell. A teflon knife-edge washer was used to limit crevice corrosion at the specimen-plate interface. A PAR Model 273/315 potentiostat/automated corrosion measurement system was utilized to perform the scans. Specimens were exposed to the solution and allowed to attain a steady state corrosion potential. This process usually took 3 to 6 hours. When a steady state corrosion potential was attained, an anodic

polarization scan was initiated. The initial applied potential was 40 mV below the measured corrosion potential. The applied potential was scanned at a rate of 0.2 mV/sec. The scan direction was then reversed at an arbitrarily assigned current density of 200 $\mu A/cm^2$. The scan was continued through E_{corr} then terminated.

GALVANIC COUPLING EXPERIMENTS

Current versus time measurements were performed for solution heat treated (SHT) 2090 galvanically coupled to each of the three cast constituent phases and the synthesized T_1. In each of the experiments a PAR 173 Potentiostat/Galvanostat was used in a potentiostatic mode to monitor current.

In each experiment the synthesized phase was connected to the working electrode input of the potentiostat. The SHT 2090 was connected to the counter and reference electrode inputs. The potentiostat was set so that a potential of 0.0 volts was maintained between the reference electrode and working electrode inputs. In this configuration, the potentiostat simulated a zero resistance ammeter and measured the current flow at the couple's free corrosion potential.

The galvanic couple experiments were performed to simulate a constituent or a T_1 particle surrounded by an Al-Li-Cu matrix. To accomplish this, electrodes were constructed so that the constituent or T_1 phase was physically surrounded by 2090 matrix. For the constituents, a cylindrical piece of the cast

constituent alloy was inserted into a hole drilled into a SHT 2090 plate. For the T_1, a small section of a plate from the cast ingot was inserted into a slot machined into the SHT 2090. Teflon separators were used to isolate the embedded phase from the SHT 2090.

The exposed area of the constituent was 0.1 cm while that of the SHT 2090 was 0.9 cm. The T_1 to SHT 2090 exposed area ratio varied from experiment to experiment and is noted on the current versus time plots.

SIMULATED CREVICE EXPERIMENTS

A cylindrical bore 2.5 mm in diameter and 10 mm in depth was machined into a blocks of 2090 measuring 1 x 1 x 1.5 cm. The barrel of a pH micro-electrode (2.35 mm in diameter) was inserted into the bore forming a crevice between the wall of the bore and the barrel of the electrode. The specimen was immersed in aerated 3.5 w/o NaCl. The pH was then monitored for up to 7 days.

EXPERIMENTAL RESULTS

ANODIC POLARIZATION

Table 3 summarizes the polarization data as a function of aging time. Although no measurable trend is observed for the corrosion potential, a slight decreasing trend is observed in both the breakaway and repassivation potentials as aging progresses. These results are consistent with earlier work (2,3,6). Although these electrochemical parameters were only

slightly sensitive to increased aging, a significant increase in subgrain boundary pitting was observed. Figure 3 shows subgrain boundary pitting on peak aged 2090. Subgrain boundary pitting was characterized by small individual pits which were distributed evenly along boundaries exposed at the surface of the specimen. In under aged 2090, the type of boundary attack shown in figure 3 was much less pronounced.

A second type of pitting was also observed. Scanning electron microscopy was used to show that gross pitting was associated with constituent particles. This type of pitting is shown in figures 4a and 4b. Figure 4a is a scanning electron micrograph a pit which was imaged using backscattered electrons. In this imaging mode, regions of high average atomic number appear brighter than regions of low average atomic number. So in this micrograph the high average atomic number Al-Cu-Fe constituents appear as bright spots within the pit. This type of pitting was observed in both the peak aged and under aged tempers.

The pit morphology was more complex in the case of the constituent particle pitting. Aggressive attack occurring near the periphery of the constituent particle resulted in the formation of deep pits and fissures. Surrounding these pits and fissures were regions where the subgrain boundaries had completely dissolved forming a nearly continuous network (fig. 5). Continuous subgrain boundary dissolution of this kind was never observed to occur away from constituent particles.

GALVANIC COUPLING

It is known that the polarity of a galvanic couple can be dependent on factors other than the relative reversible potentials of the respective couple components. This is particularly true of metal alloys exposed to solutions where the concentrations of the metal ions are small and continuously changing (20,21). In these embedded galvanic couple experiments there was the added complication of a high anode to cathode surface area ratio in the case of the constituents and a low area ratio in the case of embedded T_1. Because of these considerations both open circuit potential determinations and current versus time measurements for the couples were performed to assess couple polarity.

Table 4 shows the open circuit potentials for the alloys involved. These measurements were performed in deaerated 3.5 w/o NaCl solution and represent steady state open circuit response.

Table 5 summarizes the current versus time data for galvanic couples of SHT 2090 and the synthesized constituent phases. In each case a net negative current was measured for the couple indicating that the embedded constituent acted as the cathode; in agreement with open circuit measurements.

Figure 6 shows a plot of current versus time for the SHT 2090 / T_1 couple. Consistent with the open circuit measurements, the T_1 is the couple anode. After one hour of immersion, the couple current reaches a maximum of 25μA. The area of T_1 exposed in this particular experiment was 0.05 cm^2. With this area

exposed, the dissolution current density peaked at $5x10^{-4}$ A/cm^2. This value is in good agreement with current densities measured in anodic potentiodynamic polarization of T_1* (22).

---

* During anodic potentiodynamic polarization, T_1 exhibits a potential independent current regime similar to the passive region exhibited by some metals and alloys during such experiments. However, the measured current density in this regime of 5×10^{-4} A/cm^2 is not characteristic of corrosion through a passive film.

Microscopy of Embedded Galvanic Couple Specimens

Figure 7 is an optical micrograph of the Al-18Cu-5Fe embedded constituent specimen which illustrates the features common to all of the galvanic couple experiments. Pitting was observed all across the SHT 2090 surface but was more severe nearer to the constituent. Dissolution in the 2090 was localized near the embedded constituent which formed pits and fissures. The formation of pits and fissures in turn appeared to stimulate continuous subgrain boundary dissolution. The features observed in the embedded galvanic couple experiments were quite similar to those observed near real constituents.

ARTIFICIAL CREVICE EXPERIMENTS

Figure 8 illustrates the pH measured within an artificial crevice of 2090UA as a function of time. Note that the pH quickly attains a steady-state pH value of approximately 4. Similar curves and steady-state pH values were also obtained for SHT and PA tempers.

DISCUSSION

In this study, two different types of pitting were observed. The first type of pitting is termed subgrain boundary pitting (fig. 3). This type of attack was distinguished by discrete pits on high and low angle boundaries and was found to be temper dependent. The degree of pitting was observed to increase for increased aging times up to 14 hours at 162^{o} C.

The second type of attack was always associated with constituent particles in the plate. This type of attack was characterized by large pits surrounded by regions where subgrain boundaries were completely dissolved. The appearance of this type of attack was consistent with the type of attack reported by Kumai et al. (6). This type of pitting and continuous subgrain boundary dissolution will be discussed further in the second section.

Grain Boundary Pitting. Temper dependent, preferential high angle and low angle grain boundary attack has been observed on 2090 alloys (2,6,23). Two mechanisms have been proposed for boundary attack. The first mechanism, proposed by Rinker, Marek and Sanders in a study of 2020, claimed that selective dissolution was responsible for boundary attack (2). The second mechanism proposed that copper depleted T_1 precipitate free zones (PFZ s) had formed and were actively dissolving (6). Presently, there is no consensus as to which mechanism causes grain boundary pitting.

The 2090 alloy used in this study was subjected to a 6% stretch after solution heat treatment and prior to any aging

treatment. A stretch prior to heat treatment introduces dislocations to the subgrain interiors which can serve as nucleation sites for T_1 during aging (4). Stretching prior to aging is reported to minimize the width of the PFZ to some distance less than that of the average T_1 precipitate spacing within the subgrains (19). Kumai et al. also claim that copper depletion along subgrain boundaries is reduced for stretched 2090 (6).

From an electrochemical standpoint, T_1 is a suspect phase. As noted above, the T_1 dissolution rate has been measured to be 5×10^{-4} A/cm^2. If it is assumed that the PFZ along a subgrain boundary is pure aluminum (a worst case scenario considering the ennobling effects of copper additions to aluminum) we can use available corrosion rate data for aluminum to assess the dissolution response of a subgrain boundary region. Table 5 summarizes the pertinent corrosion rate data.

Results from corrosion experiments show that T_1 precipitates are likely to be the most active phase present. Current versus time data show that T_1 dissolves at a rate approximately 100 times greater than the surrounding matrix material. Based on this evidence it is likely that subgrain boundary pitting is a result of selective dissolution of T_1. In the case of unstretched 2090 where a copper depleted zone is reported to exist, the dissolution rate of T_1 is about 10^4 times greater than the PFZ dissolution rate. Hence the dominant contribution to boundary dissolution must again be due to T_1 precipitates.

Kumai et al. argue that selective T_1 dissolution at the boundary should be accompanied by enhanced general corrosion in stretched 2090 where extensive T_1 precipitation has occurred within subgrains. However, it is known that in most instances, for any planar segment of boundary only one T_1 variant is present (16). As a result, precipitate spacing on a subgrain boundary would be expected to be much smaller than that within the subgrain in under to peak aged conditions. This is commonly observed in TEM micrographs imaged using T_1 reflections (16,19,25). In terms of corrosion behavior this means that dissolution of a T_1 precipitate on a boundary would be much more likely to expose another T_1 precipitate. Dissolution of a T_1 precipitate within the subgrain, however, would be likely to expose matrix which would corrode at a slower rate. As a result, boundary pitting can occur without enhanced general corrosion.

Constituent Particle Pitting. As stated earlier, Al-Cu-Fe constituents were found distributed throughout the 2090 plate. Corrosion potential and current data from galvanic couple experiments suggest that these constituents act as small cathodes embedded in a large anode. Normally, a high anode to cathode area ratio results in a slow rate of corrosion (20). However, localized corrosion due to dispersed noble particles in aluminum can result in accelerated corrosion in small regions. Specifically, the presence of iron rich impurity particles in aluminum are known to induce pitting at their periphery (26,27). In a study of the cathodic potentiostatic polarization response of Al-0.5Fe-0.1Si (AA1050A), Nisancioglu et al. showed that pits

grew around Fe-rich particles when the specimen was polarized to -1.2 V_{SCE} for 24 hours (28).

Once a pit has formed around a noble constituent particle, the pit solution can become quite aggressive to the aluminum matrix. Acidic and basic crevice solutions have been reported in experiments simulating local environments using 2090 (29-31). Both alkaline and acidic aqueous solutions are known to reduce passive film stability and increase the corrosion rate of aluminum. Based on the pH versus time experiments performed in artificial crevice experiments with Al-Li-Cu alloys, it is believed that the solution in the crevices formed near constituent particles are acidic (29). Results from pH versus time experiments performed in this study support these findings.

As stated earlier, the appearance of continuous subgrain boundary attack is consistent with the observations of Kumai et al. (6). In this situation, it is the development of an occluded environment which appears to be the factor that distinguishes subgrain boundary pitting from continuous subgrain boundary dissolution. The T_1 precipitates on the subgrain boundaries dissolve as in the case of subgrain boundary pitting, but now subgrain faces exposed by the dissolution of the T_1 are susceptible to accelerated dissolution due to the aggressive pit solution. The result is continuous subgrain boundary attack.

To summarize, the mechanism of continuous subgrain boundary dissolution is proposed to occur in the following way: (1), attack is localized by the galvanic action of embedded

constituents; (2), selective dissolution of T_1 exposes subgrain faces to an acidic crevice solution; (3), the acidic solution increases the corrosion rate of the aluminum subgrain face resulting in continuous attack of the subgrain boundary. The development of continuous subgrain boundary dissolution associated with constituent particle pitting is shown schematically in figure 9.

CONCLUSIONS

1.) Based on open circuit measurements and galvanic couple experiments, a galvanic series can be constructed for the phases in 2090 which appear to govern corrosion behavior. In the order of decreasing nobility they are: constituent phases, 2090 matrix and T_1 (Al_2CuLi).

2.) Two different types of pitting have been distinguished. They are:

a.) subgrain boundary pitting which is attributed to the selective dissolution of T_1 subgrain boundary precipitates.

b.) constituent particle pitting characterized by the formation of large pits surrounded by a continuous network of dissolved subgrain boundaries.

3.) A proposed mechanism for continuous subgrain boundary dissolution is as follows:

a.) localized galvanic corrosion occurs near the constituent periphery
b.) an occluded environment develops with a low pH
c.) selective dissolution of T_1 exposes subgrain faces
d.) low pH solution in the occluded environment stimulates aggressive subgrain wall dissolution leading to continuous boundary attack.

4.) As the aging time is increased (up to peak aged condition), Alloy 2090 exhibits a decreasing breakaway potential and repassivation potential, and an increasing concentration of grain and subgrain boundary pitting.

ACKNOWLEDGMENTS

This research was sponsored by the ALCOA Technical Center, Steve Byrne and Edward L. Colvin Program Directors and by NASA Langley Research Center Grant No. NAG-1-745-2, Dennis L. Dicus, Program Director. The authors would also like to thank ALCOA for supplying the material used in this study.

REFERENCES

1. P. Niskanen, T.H. Sanders, Jr., M. Marek, J.G. Rinker, Aluminum-Lithium Alloys, TMS-AIME, Warrendale, PA, 1981, p. 347.

2. J.G. Rinker, M. Marek, T.H. Sanders, Jr., Mat. Sci. Engr., 64, p. 203, 1984.

3. E.L. Colvin, S.J. Murtha, R.K. Wyss, Conf. Proc.: Aluminum Alloys-Their Physical Metallurgy and Mechanical Properties, University of Virginia, June, 1986, p. 1853.

4. J.P. Moran, E.A. Starke, Jr., G.E. Stoner, G.L. Cahen, Jr., Corrosion, vol. 43, p. 347, 1987.

5. C.T. Tsao, P.P. Pizzo, NACE CORROSION '85, Boston, MA, Paper # 69.

6. C. Kumai, J. Kuzinski, G. Thomas, T.M. Devine, DOE Report, DE-AC03-765 F00098, March, 1987.

7. E.A. Starke, Jr., T.H. Sanders, Jr., Jrnl. of Metals, vol. 33, p. 24, 1984.

8. M.K. Tosten, A.K. Vasudevan, P.R. Howell, Met. Trans., vol. 19A, p. 51, 1988.

9. R.J. Rioja, P.E. Bretz, R.R. Satwell, W.H. Hunt E.A. Ludwiczak, Conf. Proc.:Aluminum Alloys-Thier Physical Metallurgy and Mechanical Properties, University of Virginia, June, 1986, p. 1781.

10. H.K. Hardy, Jrnl. of Metals, vol. 84, p. 429, 1955-56.

11. T.H. Sanders, Jr. E.A. Starke, Jr., Aluminum-Lithium Alloys II, TMS-AIME, Warrendale, PA, 1984, p. 1.

12. J.C. Huang, A.J. Ardell, Aluminum-Lithium Alloys III, Institute of Metals, London, 1986, p. 455.

13. W.S. Miller, J. White, D.J. Lloyd, Conf. Proc.: Aluminum Alloys-Their Physical Metallurgy and Mechanical Properties, University of Virginia, June, 1986, p. 1799.

14. R.B. Nicholson, G. Thomas, J. Nutting, Acta. Met., vol. 8, p. 172, 1960.

15. P.J. Gregson, H.M. Flower, Acta. Met., vol. 33, p. 527, 1985.

16. M.H. Tosten, A.K. Vasudevan, P.R. Howell, Aluminum-Lithium Alloys III, Institute of Metals, London, 1986, p. 490.

17. W.A. Cassada, G.J. Shiflet, E.A. Starke, Jr., Conf. Proc.: Aluminum Alloys-Their Physical Metallurgy and Mechanical Properties, University of Virginia, June, 1986, p. 695.

18. W.A. Cassada, G.J. Shiflet, E.A. Starke, Jr., Scripta Met., vol. 20, p. 751, 1986.

19. F.S. Lin, S.B. Chakrabortty, E.A. Starke, Jr., Met. Trans., vol. 13A, March, 1982, p. 401.

20. J.W. Oldfield, "Electrochemical Theory of Galvanic Corrosion", Galvanic Corrosion, ASTM STP 978, H.P. Hack, Ed., ASTM, Philadelphia, PA, 1988, p. 5-22.

21. D.R. Gabe, M. Shirkanzadeh, Br. Corros. J., 1980, vol. 15, no. 4, p. 216, 1980.

22. R.G. Buchheit, G.E. Stoner, to be published in Aluminum-Lithium Alloys V, 1989.

23. E.I. Meletis, J.M. Sater, T.H. Sanders, Jr., Conf. Proc.: Aluminum Alloys-Their Physical Metallurgy and Mechanical Properites, University of Virginia, June, 1986, p. 1157.

24. M. Pourbaix, Atlas of Electrochemical Equilibria, NACE, Houston, TX, 1966, p. 173.

25. M. Avalos-Borja, P.P. Pizzo, L.A. Larson, "Transmission Electron Microscopy Characterization of Microstructural Features in Al-Li-Cu Alloys", NASA Technical Memorandum 84384, Oct., 1983.

26. L.F. Mondolfo, Aluminum Alloys: Structure and Properties, Butterworths, London, 1976.

27. J.E. Hatch, Properties and Physical Metallurgy of Aluminum Alloys, ASM, Metals Park, OH, 1984, p. 279.

28. K. Nisancioglu, K.Y. Davanger, O. Strandmyr, H. Holtan, J. Electrochem. Soc., vol. 128, no. 7, p. 1523, 1981.

29. J.G. Craig R.C. Newmann, Aluminum-Lithium Alloys IV, Paris, June, 1987.

30. J.G. Craig, R.C. Newmann, M.R. Jarrett, N.J.H. Holroyd, Journal de Physique, vol. 48, no. 9, p. 825, 1987.

31. N.J.H. Holroyd, A. Gray, G.M. Scamans, R. Hermann, Aluminum-Lithium Alloys III, Institute of Metals, London, 1986, p. 310.

TABLE 1 : Materials Properties

Chemical Composition (weight %)

Li	Cu	Zr	Fe	Si	Ti	Mg
2.12	2.60	0.11	0.06	0.05	0.02	0.01

Grain Sizes

	Short Transverse	Transverse	Longitudinal
Grain (mm)	0.15	0.70	12-15
SubGrain (μm)	10	10	15

Heat Treatments

Solution Heat Treated, Quenched and Stretched 6% :

UNDER-Aged : 4 hours at 162°C
PEAK -Aged : 12 hours at 162°C

TABLE 2 : A Summary of X-ray diffraction data for the Al-Li-Cu cast ingot

Measured[1]		T_1 [2]		T_2	
d	I	d	I	d	I
4.682	28	4.69	20		
4.330	26	4.31	30		
3.913	12	3.90	30		
3.369	68			3.37	100
3.158	4	3.15	30		
2.912	4			2.92	8
2.536	5	2.53	20		
2.338	17	2.34	60		
2.181	8	2.19	30		
2.153	20	2.15	100		
2.063	100			2.06	100
2.035	5	2.05	30		
1.955	25	1.95	100		
1.760	18			1.76	40
1.704	5	1.70	10		
1.622	4	1.62	10		
1.583	5	1.58	30		
1.470	10	1.46	20	1.48	16
1.372	4	1.37	30	1.39	18
1.337	8	1.33	30		
1.330	9	1.32	30		
1.260	8	1.24	30		
1.189	6	1.19	30	1.19	40
1.168	5	1.17	20		
1.136	4	1.13	10	1.12	20
0.986	5			0.98	20
0.922	6			0.92	40

[1] d = d-Spacings, in angstroms. I = relative intensity (%).
[2] d-Spacings were obtained from the JCPDS Diffraction Data File.

TABLE 3 : A Summary of Polarization Data

(Potentials : mV vs. SCE Current Density : A/cm^2)

Temper	E_{corr}	i_{pass}	E_{br}	E_{rp}
Solution Heat Treated	-985	$1x10^{-7}$	-650	-850
UNDER-aged	-916	$1x10^{-6}$	-690	-908
PEAK-aged	-892	$6x10^{-7}$	-725	-930

TABLE 4 : Open circuit potential data for 2090 and synthesized phases.

Material	Open Circuit Potential (mV vs. SCE)
2090	- 985
Al-14Cu	- 810
Al-18Cu-5Fe	- 770
Al-24Cu-5Fe	- 780
T_1 (Al_2CuLi)	- 1100

TABLE 5 : Summary of current data for galvanic couple experiments

Constituent	Current (A/cm^2)
Al-14Cu	-5×10^{-7}
Al-18Cu-5Fe	-7×10^{-6}
Al-24Cu-5Fe	-3×10^{-6}

TABLE 6 : A summary of corrosion rates.

Material	Corrosion Rate (A/cm^2)	
T_1	5×10^{-4}	
Al PFZ	3×10^{-8}	(24)
SHT 2090 (matrix)	2×10^{-6}	

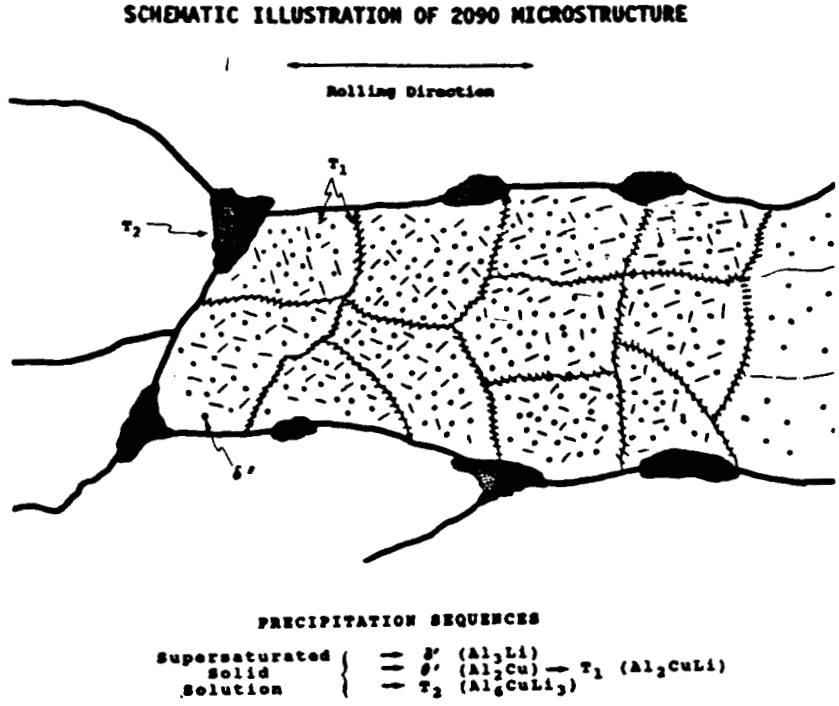

Figure 1. Schematic illustration of typical 2090 microstructural features after peak aging.

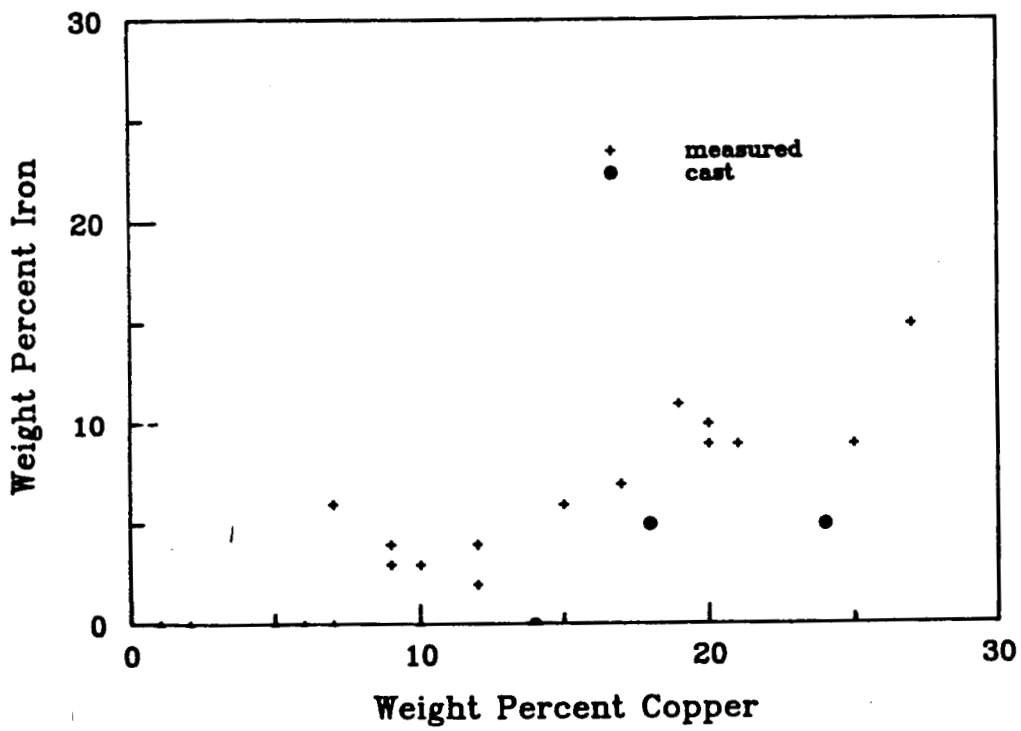

Figure 2. A plot summarizing both the measured and synthesized (cast) constituent particle compositions.

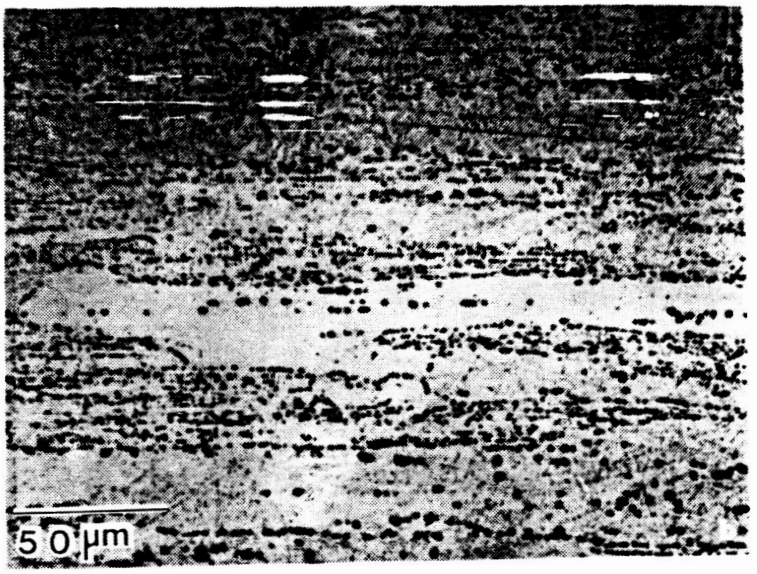

Figure 3. Optical micrograph of subgrain boundary pitting on PA 2090 subjected to anodic polarization in deaerated 3.5 w/o NaCl solution.

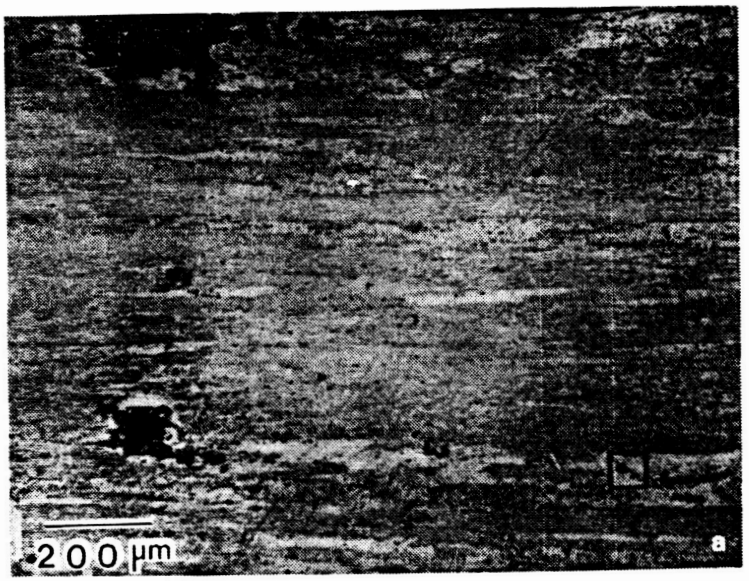

Figure 4a. Optical micrograph of constituent particle pitting on PA 2090 subjected to anodic polarization.

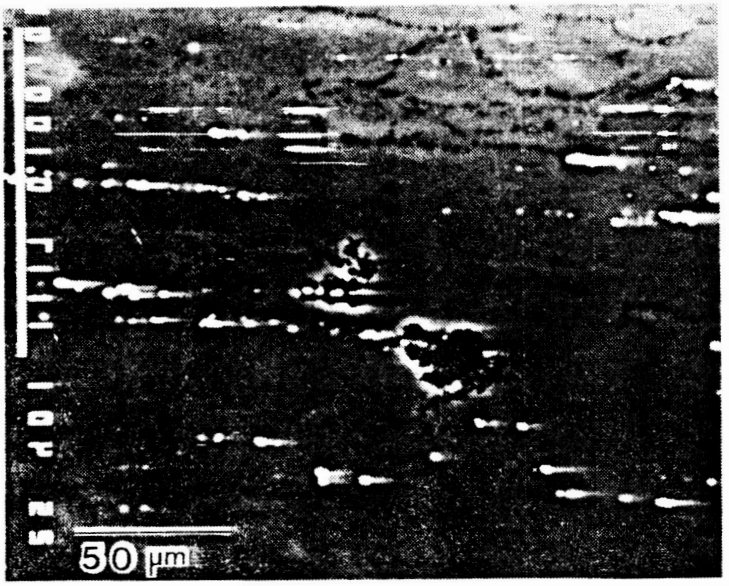

Figure 4b. Backscattered electron image of the region outlined in fig. 4a., brightest spots are constituent particles,

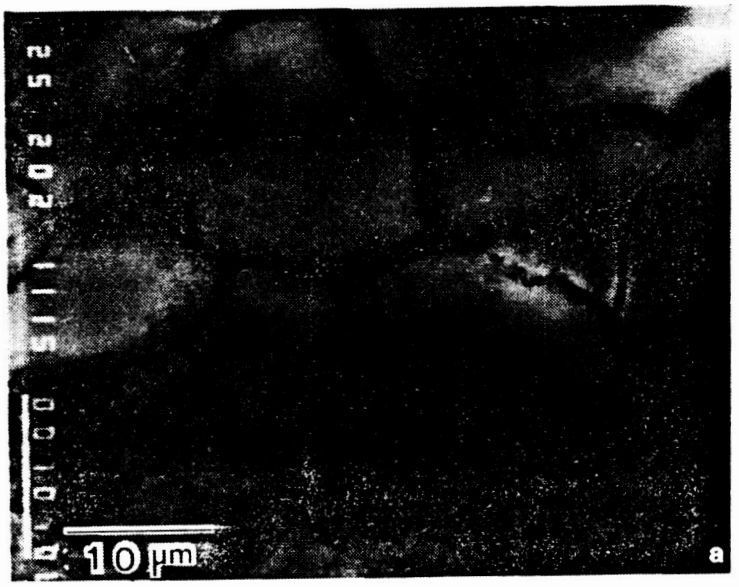

Figure 5. Secondary electron image of continuous subgrain boundary dissolution in the vicinity of a constituent particle subjected to anodic polarization.

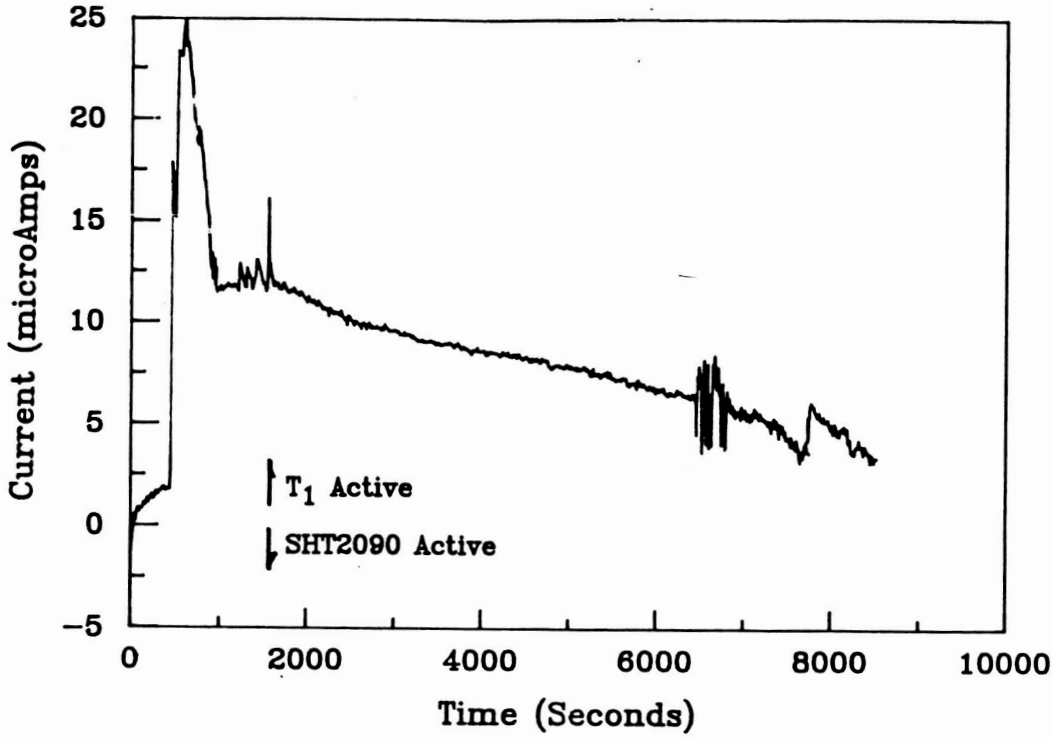

Figure 6. Current versus time data for an SHT 2090 : T_1 galvanic couple experiment performed in deaerated 3.5 w/o NaCl solution.

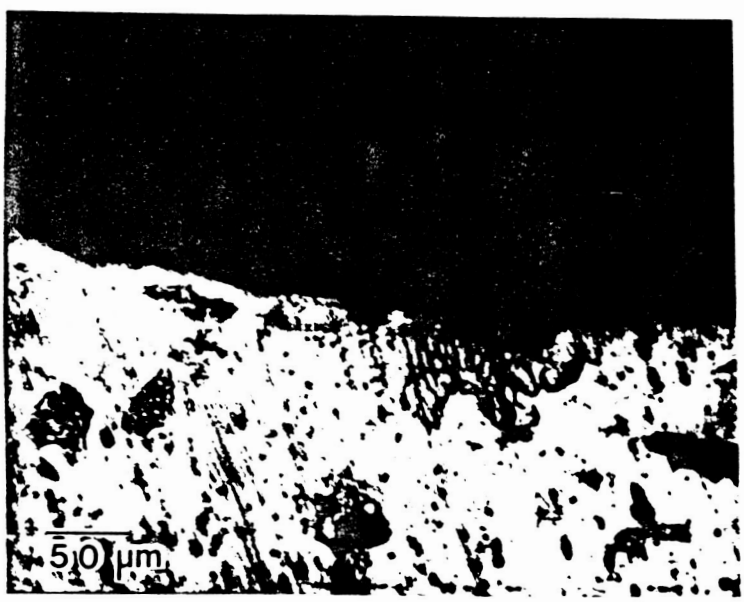

Figure 7. Optical micrograph of continuous subgrain boundary dissolution which occurred during an embedded galvanic couple experiment.

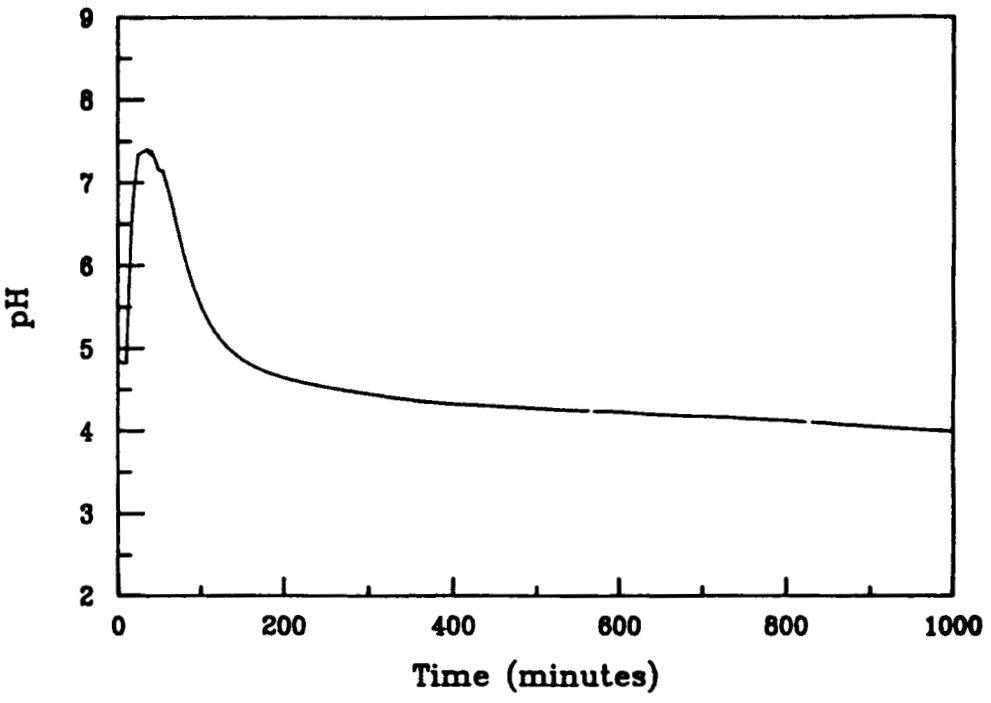

Figure 8. pH versus time response in an artificial crevice in UA 2090.

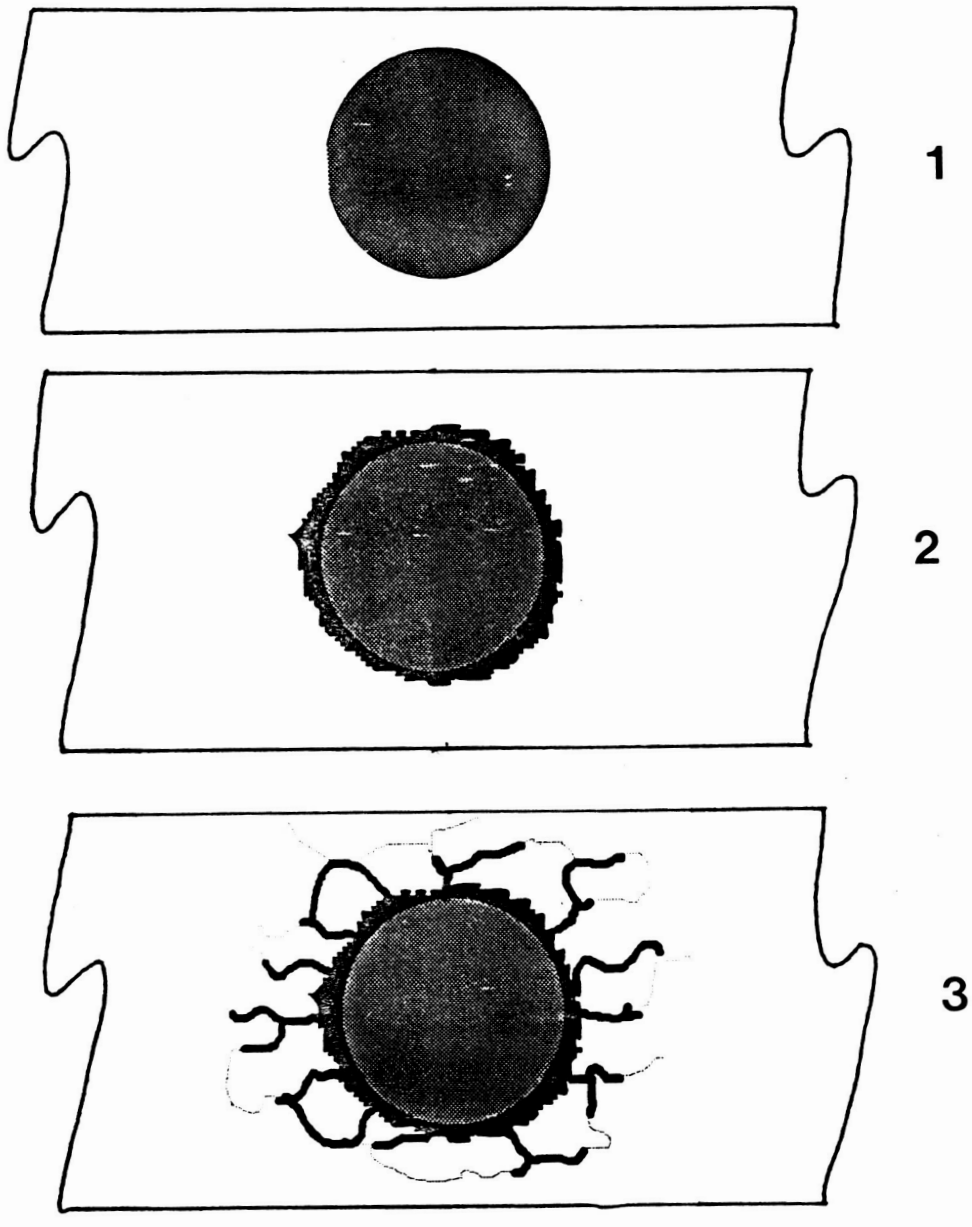

Figure 9. Schematic illustration of the mechanism of constituent particle pitting. Part (1) shows the embedded noble particle, (2) shows the localization of corrosion around the particle periphery, (3) shows the subsequent subgrain boundary attack occurring about the pit.

APPENDIX II: GRANT CONFERENCE PARTICIPATION AND TRAVEL
(June 1, 1988 to December 31, 1988)

Robert S. Piascik and Richard P. Gangloff

1. Grant Review Meeting at Langley Research Center, July, 1988.

2. International Conference on Environment-Induced Cracking of Metals, Kohler, WI., October, 1988. Presented poster entitled: "Aqueous Environment Effects On Intrinsic Corrosion Fatigue Crack Propagation In An Al-Li-Cu Alloy".

3. ASTM technical committee meeting, Atlanta, GA., November, 1988. Presentation to E24.04 Subcommittee on Subcritical Crack Growth entitled: "Intrinsic Corrosion Fatigue Crack Propagation in Al-Li Alloys".

4. ASTM technical committee meeting, Atlanta, GA., November, 1988. Presentation to E24.04 Subcommittee on Subcritical Crack Growth entitled: "Specimen Geometry Effects on Near Threshold Fatigue Crack Growth Measurement".

Richard P. Gangloff

1. International Conference on Environment-Induced Cracking of Metals, Kohler, WI., October, 1988. Presented invited entitled: "Corrosion Fatigue Crack Propagation".

2. World Materials Congress, Chicago, ILL., October, 1988, Presented invited paper with R.O. Ritchie entitled: "Fatigue of Al-Li Alloys".

Glenn E. Stoner, Rudolph G. Buchheit, Jr. and James P. Moran

1. Grant Review Meeting at Langley Research Center, July, 1988.

James P. Moran

1. International Conference on Environment-Induced Cracking of Metals, Kohler, WI, October, 1988.

Robert E. Swanson

1. Grant Review Meeting at Langley Research Center, July, 1988.

APPENDIX III: SCHEDULED PRESENTATIONS-ABSTRACTS

Robert S. Piascik and Richard P. Gangloff

1. "Fatigue Crack Propagation in Aluminum-Lithium Alloys", at 5th International Aluminum-Lithium Conference, Williamsburg, March, 1989.

Richard P. Gangloff

1. "Measurement and Modeling of Environmental Cracking by Hydrogen: The Continuum Perspective", at Corrosion 89: NACE Corrosion Research Symposium, New Orleans, March, 1989.

R.G. Buchheit and G.E. Stoner

1. "The Electrochemical Behavior of the T_1 Intermetallic Compound in Aqueous Chloride Environments", at 5th International Aluminum-Lithium Conference, Williamsburg, March, 1989.

J.P. Moran and G.E. Stoner

1. "The Influence of Bulk and Local Solution Chemistries on the SCC and Localized Corrosion Behavior of Alloy 2090, at 5th International Aluminum-Lithium Conference, Williamsburg, March, 1989.

FATIGUE CRACK PROPAGATION IN ALUMINUM-LITHIUM ALLOYS

R.O. RITCHIE and K.T. VENKATESWARA RAO

Center for Advanced Materials, Lawrence Berkeley Laboratory
and
Department of Materials Science and Mineral Engineering
University of California
Berkeley, CA 94720

and

RICHARD P. GANGLOFF and ROBERT S. PIASCIK

Department of Materials Science
University of Virginia
Charlottesville, VA 22901

ABSTRACT

This review analyzes those factors which control the fatigue crack propagation resistance of advanced aluminum-lithium alloys. Fracture mechanics experimentation and micromechanical modeling establish that fatigue crack propagation in these wrought and precipitation hardened alloys is controlled by mechanical mechanisms for crack tip shielding, and by chemical mechanisms for gaseous and aqueous environments. Microstructural effects, while prominent, are interpreted within these frameworks.

Crack growth kinetics data exist for commercial Al-Li alloys (viz. 2090, 2091, 8090, 8091 and powder metallurgy alloys) as a function of microstructure, crack path orientation, crack size, load ratio, specimen geometry, load sequence, temperature, and environment chemistry for gases and electrolytes. For moist air, long crack and low stress ratio conditions favor growth rates which are up to three orders of magnitude slower than values for commercial 2000 and 7000 series alloys. Tensile overloads and overaging impart added fatigue resistance. Al-Li based alloys exhibit far less outstanding fatigue cracking behavior for high stress ratios, for small crack sizes, after compressive overloads and for specimen geometries which minimize mode II displacements and out-of-plane crack deflections. These observations are explained based on the prominent role of crack tip shielding; local stress intensity and plastic strain amplitude are reduced by premature crack surface contact, that is by asperity induced

closure. These extrinsic mechanisms for fatigue resistance are ascribed to tortuous, locally deflected crack paths in Al-Li alloys and are derived from crystallographic texture, microstructural anisotropy, slip localization and slip plane cracking.

For corrosion fatigue in purified water vapor and aqueous chloride solutions, alloy 2090 exhibits crack growth kinetics which are superior to those of 7000 series alloys and equivalent to other 2000-class materials. For peak aged 2090, crack growth rates increase by up to 50-fold according to the environment order: equal in vacuum, ultra-high purity helium, oxygen; moist air; NaCl with cathodic polarization; water vapor; NaCl with anodic polarization. Cracking in water vapor is enhanced by increasing the ratio of vapor pressure to loading frequency, consistent with fast surface reaction and gas phase transport limited kinetics modeling. Here, however, near threshold cracking is more severe than predicted. For the chloride solution, crack growth rates are exacerbated by anodic polarization and by increased loading frequency. For all cases excepting short-transverse orientations, corrosion fatigue is transgranular (viz. slip band, subboundary and cleavage cracking) without direct influence of high angle grain boundaries. Environment reduces extrinsic effects by reducing crack path roughness due to increased cleavage cracking; and alternately may promote closure by corrosion debris. More fundamentally, intrinsic environmental crack growth kinetics are interpreted based on a dominant role of hydrogen embrittlement, with little influence of crack tip surface films on cyclic plasticity. A lack of measurements and models of crack chemistry precludes determination of the importance of film rupture and repassivation events.

This work was supported by the Director, Office of Energy Research, Office of Basic Energy Sciences, Materials Sciences Division of the U.S. Department of Energy under Contract No. DE-AC03-76SF00098 (ROR and KTVR); and by the National Aeronautics and Space Administration, Langley Research Center under Grant No. NAG-1-745 (RPG and RSP).

For presentation at:

Fifth International Aluminum-Lithium Conference
Williamsburg, Virginia
March, 1989.

Keynote Address: Corrosion 89; NACE Corrosion Research Symposium; New Orleans; March, 1989.

MEASUREMENT AND MODELING OF ENVIRONMENTAL CRACKING BY HYDROGEN: THE CONTINUUM PERSPECTIVE

RICHARD P. GANGLOFF[1]

Department of Materials Science
University of Virginia
Charlottesville, VA 22901
USA

Prevention of hydrogen environment embrittlement (HEE) of structural alloys requires measurement and modeling of crack tip mechanical and chemical damage processes. Continuum mechanics descriptions of environment assisted subcritical crack propagation, largely represented by fracture mechanics experimental and analytical methods, have evolved over the past 30 years. Analyses of mass transport and electrochemical reactions within occluded cracks were considered over a similar period. When integrated, these two approaches provide the basis for damage tolerant life prediction methods, high performance materials, chemically inhibited environments, and sensors. Current understanding and uncertainties are reviewed for monotonic loading (stress corrosion) and corrosion fatigue crack propagation; the main categories of the HEE problem.

Continuum approaches are based on measurable and controllable external variables such as stress intensity factor or applied electrode potential. To be rational, the means must exist to relate the former to crack tip stress, strain, strain rate and microscopic deformation events; and the latter to crack tip pH, potential and the kinetics of clean surface reactions. Such crack tip processes control hydrogen environment cracking. While a formidable challenge, recent successes indicate that the continuum approach is relatable to the physics of cracking, and is thus relevant to mechanistic and engineering studies.

---

[1] This research is supported by the National Aeronautics and Space Administration, Langley Research Center (Grant NAG-1-745), by the Newport News Shipbuilding and Dry Dock Company (Grant POM-7672-R) and by the Virginia Center for Innovative Technology (Grant TDC-88-001).

THRESHOLD STRESS INTENSITY FACTORS, FOR STRESS CORROSION CRACKING (K_{Iscc}) OF STEELS in a variety of electrolytes and gases which produce atomic hydrogen environment embrittlement, are well characterized by fracture mechanics. Extensive data provide a basis for engineering design and indicate the unifying importance of permeation sensor measurements of hydrogen uptake from laboratory and plant equipment environments. Micromechanical modeling relates averaged K_{Iscc} to crack tip normal stresses acting over a microstructural distance, and to hydrogen content. Mass transport and reaction modeling, coupled with confirming measurements of crack tip pH and electrode potential, were merged with the threshold concept to develop a model of the effect of crack geometry and chemical variables on HEE. Predictions of increased hydrolytic acidification and hydrogen atom production within small cracks explain a variety of fracture measurements; this integration demonstrates necessary modifications of the conventional fracture mechanics approach. Uncertainties remain, for example regarding the relationship between the stress intensity factor and the statistical distribution of normal stress and hydrogen segregation on the microscopic scale.

THE FRACTURE MECHANICS APPROACH TO CORROSION FATIGUE CRACK PROPAGATION enables component life prediction which is being transitioned to commercial applications; for example offshore structures. Phenomenological data bases are extrapolated to long time and varying environmental conditions by continuum models of damage mechanisms. Component life is predicted from laboratory data based on the premise of growth rate similitude. Predictions are tested by experiments with instrumented, full-scale components in aggressive environments. Despite important successes, several uncertainties remain.

The following conclusions are supported by experiments and modeling for two cases of cycle-time dependent corrosion fatigue: low strength steels in electrolytes typical of the marine environment, and advanced aluminum-lithium alloys in gases and solutions capable of producing adsorbed hydrogen.

- Fracture mechanics descriptions of corrosion fatigue propagation; viz, crack growth rate as a function of stress intensity factor; are broadly established and quantitative. Experimental methods are well developed and extensive data bases have been produced over the past three decades.

- Future experimental procedures will exploit precision crack length measurement and computer control of stress intensity to determine novel corrosion fatigue crack growth rate data. The basic problem confronting the experimentalist is the lack of direct probes of mechanical and chemical damage processes local to the corrosion fatigue crack tip.

- A plethora of interactive variables influence the corrosion fatigue crack growth rate-stress intensity relationship. Time (loading frequency) dependencies are critical; complicating long-life component performance predictions based on shorter term laboratory data. Additionally, corrosion fatigue crack growth rates are affected by environment chemistry (viz: temperature; gas pressure and impurity content; electrolyte pH, potential, conductivity, and halogen ion content); by mechanical variables such as ΔK, mean stress, and waveform; and by metallurgical variables including microstructure. Data suggest that yield strength is not a critical factor in corrosion fatigue.

- Continuum fracture mechanics descriptions of corrosion fatigue and the similitude concept are hindered by the inability of stress intensity to simply describe local crack tip mechanical and chemical driving forces. Data and analyses demonstrate that the unique relationship between da/dN and ΔK is compromised by: a) premature crack surface closure contact, b) transient crack growth, c) crack size and geometry dependent crack growth rates. Causal mechanisms include crack wake surface contact, deflected and multiple cracking, pronounced crack tip plasticity and crack geometry dependent occluded crack chemistry. Stress intensity adequately describes elastic-plastic stresses, strains and strain rates local to the crack tip plastic zone; but not within 1 to 5 μm of the crack tip, within single grains poorly described by the constitutive behavior of the polycrystal and when deformation response is environment sensitive. These limitations do not preclude the major quantitative approach developed to date to characterize subcritical crack propagation. Rather, they indicate the direction for crack tip modeling.

- Micromechanical and chemical models of crack tip driving forces and fatigue damage provide a means to strengthen the weaknesses of the continuum approach. Models, based on hydrogen embrittlement, have predicted the relative time dependence of corrosion fatigue. Absolute predictions of crack growth rate are, however, hindered by uncertainties in the fundamental mechanisms of hydrogen embrittlement. The reasons for the uniquely damaging effect of cyclic strain and environmental exposure remain speculative.

- Opportunities exist for future research to: (a) develop quantitative microchemical-mechanics models of corrosion fatigue, (b) develop methods to directly probe crack tip damage and to measure near threshold corrosion fatigue, (c) apply continuum approaches to characterize the corrosion fatigue crack propagation behavior of advanced monolithic and composite alloys, and (d) develop damage tolerant life

prediction methods and *in situ* sensors for environment chemistry and corrosion fatigue crack growth.

It is correct to isolate and examine the crack initiation and propagation stages of hydrogen environment embrittlement; that is, SCC and corrosion fatigue. As understanding of the growth of small cracks increases, whole-life models can be developed for those applications where initiation is important.

The Electrochemical Behavior of the T_1 Intermetallic Compound in Aqueous Chloride Environments

R.G. Buchheit
G.E. Stoner
Department of Materials Science
University of Virginia
Charlottesville, Virginia 22901

The intermetallic compound T_1 is suspected to play a major role in the localized corrosion of aluminum-lithium-copper alloys. The intermetallic was synthesized for characterization of its electrochemical behavior. Experiments performed included open circuit potential measurements, potentiodynamic polarization and current versus time measurements for galvanically coupled solution heat treated 2090 and synthesized T_1. In nearly neutral, deaerated 3.5 w/o NaCl solutions the corrosion potential of T_1 was measured to be -1100 mV_{SCE}. In anodic potentiodynamic polarization experiments in pH = 6 solutions, the intermetallic did exhibit a potential independent current region. Though the shape of the polarization curve in this region suggested a passive regime, the measured current density of 5×10^{-4} A/cm^2 was not typical of corrosion through a passive film. The 'breakaway' occurred at -730 mV_{SCE}. The compound dissolved anodically in experiments where it was galvanically coupled to solution heat treated 2090. Measured currents ranged from 5 to 15×10^{-6} A/cm^2.

Evidence suggesting the dealloying of copper from this compound will also be presented.

To be presented at the Fifth International Aluminum-Lithium Conference, March 28-31, 1989, Williamsburg, VA.

THE INFLUENCE OF BULK AND LOCAL SOLUTION CHEMISTRIES ON THE SCC AND LOCALIZED CORROSION BEHAVIOR OF ALLOY 2090

J.P. Moran and G.E. Stoner

Department of Materials Science
The University of Virginia
Charlottesville, VA 22901

An Abstract Submitted to The Fifth International Conference on Aluminum-Lithium Alloys

ABSTRACT

The initiation of stress corrosion cracking and the localized corrosion behavior of alloy 2090 (Al-2Li-3Cu) were investigated in various 3.5w/o NaCl-based environments. Experimental techniques utilized included SCC Time-To-Failure (TTF) measurements on smooth-bar samples in constant strain (per ASTM G-49), potentiodynamic polarization, and pH vs. time experiments in simulated crevices. Additions to the bulk environment included Li_2CO_3, Na_2CO_3 and LiCl. The alloy was investigated in an underaged and a peak-aged temper.

Stress corrosion cracking (SCC) specimens immersed in aerated NaCl did not fail after as much as 21 days; however, removal of SCC specimens from solution after 6 days and subsequent exposure to lab air resulted in fracture, usually in 10 to 20 hours. Removal of specimens from solution after 6 days and exposure in a CO_2-free environment, however, did not promote fracture. Li_2CO_3 additions to NaCl resulted in accelerated failure of SCC specimens (1 to 3 days), and improved passivity. Na_2CO_3, on the other hand, did not promote failure, but resulted in significantly reduced passivity. LiCl additions had little effect on the SCC or polarization behavior.

The proposed role of CO_2 in the lab-air experiments, as well as that of Li_2CO_3 in the constant immersion tests, is to promote the formation of a passive film along occluded cell walls, thereby reducing localized dissolution and blunting, allowing a sharp crack to propagate. This is supported by the SCC and polarization data. Although the formation and compositional characteristics of this passive film are not clear, an argument for the precipitation of Li_2CO_3 within occluded cells will be presented, based on correlations in SCC and simulated crevice data. Changes in SCC and polarization behavior as a function of aging were small, relative to the environmental effects, suggesting that local environments must be a critical aspect of any proposed SCC mechanism for alloy 2090.

DISTRIBUTION LIST

1 - 3	Mr. D. L. Dicus Contract Monitor Metallic Materials Branch, MS 188A NASA Langley Research Center Hampton, VA 23665
4 - 5*	NASA Scientific and Technical Information Facility P.O. Box 8757 Baltimore/Washington International Airport Baltimore, MD 21240
6	Mr. J. F. Royall, Jr. Grants Officer, M/S 126 NASA Langley Research Center Hampton, VA 23665
7	Dr. Charles E. Harris Mechanics of Materials Branch National Aeronautics and Space Administration Langley Research Center Hampton, VA 23665
8	Mr. W. Barry Lisagor Metallic Materials Branch NASA Langley Research Center Hampton, VA 23665
9 - 10	R. P. Gangloff, MS
11	G. E. Stoner, MS
12	T. H. Courtney, MS
13	J. A. Wert, MS
14	F. E. Wawner, MS
15	W. D. Pilkey, MAE
16	E. A. Thornton, MAE
17	J. K. Haviland, MAE
18	C. T. Herakovich, CE
19	M. J. Pindera, CE
20	J. P. Moran

21	W. C. Porr, Jr.
22	J. A. Wagner
23	R. S. Piascik
24	R. G. Buchheit, Jr.
25 - 26	E. H. Pancake, Clark Hall
27	SEAS Publications Files
28 - 29	R. E. Swanson Department of Materials Engineering Virginia Polytechnic Institute and State University Blacksburg, VA 24061

*One reproducible copy

JO#2231:ph